

# Accretion regimes in the X-ray binary systems A 0535+26 and Her X-1/HZ Her

**Dissertation**

der Mathematisch-Naturwissenschaftlichen Fakultät  
der Eberhard Karls Universität Tübingen  
zur Erlangung des Grades eines  
Doktors der Naturwissenschaften  
(Dr. rer. nat.)

vorgelegt von

**Daniela Bohl**

aus Nürtingen

Tübingen  
2014

Tag der mündlichen Qualifikation: 15.12.2014  
Dekan: Prof. Dr. Wolfgang Rosenstiel  
1. Berichterstatter: Prof. Dr. Andrea Santangelo  
2. Berichterstatter: Prof. Dr. Klaus Werner





# Abstract

This thesis discusses the physics of two accreting X-ray pulsars, A 0535+26 and Her X-1. Based on observations from different X-ray satellites, the timing and spectral behavior of the two systems is studied.

A 0535+26 is a Be/X-ray binary system, i.e. it regularly undergoes *normal* and *giant* outbursts, separated by phases of quiescence. In April 2010, *Swift/BAT* detected a brightening of A 0535+26. The maximum and the decay of the outburst were observed by the *RXTE* and *INTEGRAL* observatories. We analyzed the light curves, pulse profiles and the pulsed fraction of the source and performed a spectral analysis using the *RXTE* and *INTEGRAL* data. Our analysis reveals variability of the continuum parameters with source flux, in particular a hardening of the continuum with increasing source flux on short time scales (i.e. for single pulsation cycles) and long time scales (i.e. on time scales of many pulsation cycles). The spectra averaged over many pulsation cycles of A 0535+26 show a variation of the cyclotron line centroid energy but no correlation with the luminosity of the source. However, our short time scale analyses (i.e. based on fragments of the pulsation cycle) indicate a positive correlation of the cyclotron line energy with the source flux. Some accreting X-ray pulsars show spectral changes on long time scales and on the time scale of single pulsation cycles. Depending on the type of spectral variations with flux, the sources seem to form distinct groups. This behavior is probably reflected in the accretion regimes that may result in a particular pulsar depending on its luminosity: the so-called sub- and super-critical accretion regimes. Based on the observed spectral properties, we argue that A0535+26 operates at the sub-critical accretion

regime during the analyzed outburst.

The second part of the thesis describes the analysis of the X-ray binary system Her X-1/HZ Her. The light curve of Her X-1 shows different periodicities including the 35 day super-orbital period with two on-states (high X-ray flux) and two off-states (low X-ray flux). The source's pulse period shows a long-term spin-up, interrupted by short intense spin-down periods. A possible explanation for this behavior can be ejection of matter during the spin-down episodes. In this work, we have analyzed *XMM-Newton* observations taken during main-on states of the source and studied the spectral changes in the *RGS* and *EPIC* data. We compared the derived amount of hot, photoionized material for different spin-up/-down regimes. A change in the amount of matter around the neutron star is expected to be indicated by the width and intensity of the emission lines from the photoionized plasma and of the  $\text{FeK}\alpha$  emission line. We do not see a correlation between the line parameters and the locally measured pulse period change, and thereby cannot supply evidence of increased disk outflows within this analysis.

The analysis of *EPIC-pn* spectra on short time scales (i.e. based on fragments of the pulsation cycle) reveals a unprecedented variability of the spectral parameters. Our results support the model of a freely precessing neutron star with a complex non-dipole magnetic field. The spectral variability is attributed to the emission from several emission components, i.e. several emission regions on the neutron star.

# Zusammenfassung

Diese Arbeit behandelt die Eigenschaften zweier akkretierender Röntgenpulsare, A 0535+26 und Her X-1. Basierend auf den Beobachtungsdaten von Röntgensatelliten wird das spektrale und zeitliche Verhalten untersucht.

Das Be/Röntgendoppelsternsystem A 0535+26 durchläuft regelmäßig „normale“ und „riesige“ Ausbrüche, ebenso wie Ruhephasen. Ein Anstieg der Leuchtkraft der Quelle wurde im April 2010 vom Röntgenobservatorium *Swift/BAT* gemessen. Daraufhin beobachteten die Satelliten *RXTE* und *INTEGRAL* das Maximum und das Abklingen des Ausbruches. Aus diesen Daten wurden Lichtkurven und Pulsprofile extrahiert und eine Untersuchung der spektralen Eigenschaften durchgeführt. Wir stellen eine Veränderung der spektralen Parameter abhängig von der Leuchtkraft fest. Insbesondere wird das Spektrum „härter“ mit zunehmender Leuchtkraft der Quelle, sowohl im Bereich einzelner Pulsationszyklen, als auch über längere Zeitbereiche hinweg (gemittelt über eine große Anzahl von Pulsationszyklen). In den über mehrere Pulsationszyklen gemittelten Spektren beobachten wir eine Variation der Energie der Zyklotronlinie, jedoch keine Korrelation mit der Leuchtkraft. Die Analyse der Spektren von einzelnen Pulsationszyklen deutet allerdings auf das Bestehen einer solchen Korrelation hin.

Die Leuchtkraft und die spektralen Eigenschaften akkretierender Röntgenpulsare sind abhängig von der Art des Akkretionsvorganges. Anhand der Leuchtkraft der jeweiligen Quelle scheinen sich diese in sogenannte „sub-kritische“ und „super-kritische“ Akkretionsregime zuordnen zu lassen. Aufgrund des beobachteten spektralen Verhaltens

argumentieren wir, dass sich A 0535+26 während des hier betrachteten Ausbruches in einem sub-kritischen Akkretionsregime befindet.

Der zweite Teil der Arbeit befasst sich mit der Analyse des Röntgendoppelsternsystems Her X-1/HZ Her. Die Lichtkurve von Her X-1 weist verschiedene Periodizitäten auf, unter anderem eine superiorbitale Periode von 35 Tagen, die sich in zwei „on-states“ (hoher Fluss im Röntgenenergie-Bereich) und zwei „off-states“ (niedriger Fluss) aufteilt. Die Pulsperiode von Her X-1 zeigt eine langfristige Abnahme („spin-up“), die durch kurze starke Pulsperiodenanstiege („spin-down“) unterbrochen wird. Dieses Verhalten kann durch Auswurf von Materie während der kurzen „spin-down“ Phasen erklärt werden. Wir haben Beobachtungen des Röntgenobservatoriums *XMM-Newton* für verschiedene „main-on states“ der Quelle analysiert. Um nach Anzeichen für Materieauswurf zu suchen, wurden die spektralen Veränderungen in den *RGS* und *EPIC* Daten untersucht. Der Anteil an heißer, photoionisierter Materie wurde für verschiedene „spin-up“ und „spin-down“ Abschnitte verglichen. Eine Änderung der Materiemenge um den Neutronenstern sollte sich in der Breite und Stärke der Emissionslinien des photoionisierten Plasmas und der Fe K $\alpha$ -Emissionslinie widerspiegeln. Anhand von diesen Beobachtungen kann kein Zusammenhang zwischen den Parametern der Emissionslinien und der lokal gemessenen Pulsperiodenänderung festgestellt werden, und damit kein Hinweis auf eine erhöhte Materiedichte erbracht werden. Die Analyse von *EPIC-pn* Spektren für Teile einzelner Pulsationszyklen zeigt eine Variation der spektralen Parameter, die mit solch hoher Auflösung und Genauigkeit bisher noch nicht gemessen wurde. Unsere Ergebnisse unterstützen das Model eines frei präzessierenden Neutronensternes mit einem komplexen Magnetfeld. Die von uns beobachtete starke spektrale Variabilität wird der Emission aus verschiedenen Komponenten, d.h. verschiedener Emissionsregionen auf dem Neutronenstern, zugeschrieben.







# Contents

<b>List of Figures</b>	<b>I</b>
<b>List of Tables</b>	<b>V</b>
<b>1 Introduction</b>	<b>1</b>
<b>2 X-ray pulsars</b>	<b>5</b>
2.1 Neutron star X-ray binaries . . . . .	5
2.1.1 Low-mass X-ray binaries . . . . .	6
2.1.2 High-mass X-ray binaries . . . . .	7
2.1.3 Neutron stars . . . . .	9
2.2 Accreting X-ray pulsars . . . . .	10
2.2.1 The accretion flow in the magnetosphere . . . . .	10
2.2.2 The accretion column . . . . .	15
2.3 Properties of accreting X-ray pulsars . . . . .	18
2.3.1 Spectral formation . . . . .	18
2.3.2 Timing properties . . . . .	24
<b>3 Satellites</b>	<b>29</b>
3.1 <i>RXTE</i> . . . . .	29
3.1.1 <i>ASM</i> . . . . .	29
3.1.2 <i>PCA</i> . . . . .	30
3.1.3 <i>HEXTE</i> . . . . .	31
3.2 <i>INTEGRAL</i> . . . . .	33
3.2.1 <i>JEM-X</i> . . . . .	34
3.2.2 <i>IBIS</i> . . . . .	35

3.2.3	<i>SPI</i>	36
3.2.4	<i>OMC</i>	36
3.3	<i>XMM-Newton</i>	37
3.3.1	<i>XMM-OM</i>	37
3.3.2	<i>RGS</i>	38
3.3.3	<i>EPIC</i>	38
<b>4</b>	<b>Be/X-ray binary system A 0535+26</b>	<b>41</b>
4.1	Overview	41
4.1.1	History	41
4.1.2	Properties of the system	42
4.2	A 0535+26 in quiescence	44
4.3	Timing properties	45
4.3.1	Pulse period evolution	45
4.3.2	Power spectrum	45
4.3.3	Pulse profiles	47
4.4	Spectral properties	50
<b>5</b>	<b><i>RXTE</i> and <i>INTEGRAL</i> observations of A 0535+26</b>	<b>55</b>
5.1	The April 2010 outburst	55
5.2	Observations	56
5.3	<i>RXTE</i> data reduction	58
5.4	<i>INTEGRAL</i> data reduction	58
5.5	Timing analysis	61
5.5.1	Light curve	61
5.5.2	Pulse profiles	62
5.5.3	Pulsed fraction	63
5.5.4	Discussion	69
5.6	Spectral analysis	71
5.6.1	Pulse phase averaged spectrum	71
5.6.2	Pulse phase resolved analysis	78
5.6.3	Pulse amplitude resolved analysis	84
5.6.4	Discussion	89
<b>6</b>	<b>Her X-1</b>	<b>93</b>
6.1	System overview	93
6.2	Timing properties	94

6.2.1	35 day periodicity . . . . .	94
6.2.2	Pulse period evolution . . . . .	97
6.2.3	Pulse profiles . . . . .	99
6.3	Spectral properties . . . . .	102
<b>7</b>	<b><i>XMM-Newton</i> observations of Her X-1</b>	<b>107</b>
7.1	Observations . . . . .	107
7.2	Data reduction . . . . .	107
7.2.1	<i>RGS</i> data reduction . . . . .	110
7.2.2	<i>EPIC</i> data reduction . . . . .	112
7.3	Timing analysis . . . . .	113
7.3.1	Light curve . . . . .	113
7.3.2	Pulse profiles . . . . .	116
7.4	Spectral analysis . . . . .	116
7.4.1	Phase averaged analysis . . . . .	116
7.4.2	Pulse phase resolved analysis . . . . .	129
7.5	Discussion . . . . .	130
<b>8</b>	<b>Summary and conclusions</b>	<b>139</b>
	<b>Bibliography</b>	<b>145</b>
<b>A</b>	<b>Appendix</b>	<b>159</b>
A.1	<i>RXTE</i> and <i>INTEGRAL</i> observations of A 0535+26 . . . . .	159
A.2	<i>XMM-Newton</i> observations of Her X-1 . . . . .	162
	<b>Publications</b>	<b>165</b>
	<b>Acknowledgment</b>	<b>169</b>
	<b>Curriculum vitae</b>	<b>171</b>



# List of Figures

1.1	Attenuation of X-ray radiation in the atmosphere . . . . .	2
2.1	Distribution of HMXB and LMXB . . . . .	7
2.2	Be/X-ray binary system . . . . .	8
2.3	Roche lobe . . . . .	11
2.4	Quasi-spherical accretion . . . . .	13
2.5	Accretion onto a neutron star . . . . .	14
2.6	Boundary layer . . . . .	15
2.7	Accretion funnel . . . . .	16
2.8	Model of accretion scenario . . . . .	21
2.9	Evolution of $E_{\text{cyc}}$ . . . . .	22
2.10	Illuminated fraction of neutron star surface . . . . .	23
2.11	Pulse profiles . . . . .	26
3.1	<i>RXTE</i> satellite . . . . .	30
3.2	<i>PCA</i> detector . . . . .	31
3.3	<i>HEXTE</i> detector . . . . .	32
3.4	<i>INTEGRAL</i> satellite . . . . .	33
3.5	<i>JEM-X</i> imager . . . . .	34
3.6	<i>IBIS</i> imager . . . . .	35
3.7	<i>XMM-Newton</i> observatory . . . . .	37
3.8	<i>RGS</i> grating . . . . .	38
3.9	<i>MOS</i> CCDs . . . . .	39
3.10	<i>pn</i> CCD camera . . . . .	40
4.1	A 0535+26 long time light curve . . . . .	43

4.2	A 0535+26 pulse period evolution . . . . .	46
4.3	A 0535+26 pulse profiles . . . . .	48
4.4	A 0535+26 pulse-to-pulse variability . . . . .	49
4.5	A 0535+26 X-ray spectrum . . . . .	51
4.6	A 0535+26 $E_{\text{cyc}}$ evolution . . . . .	52
4.7	A 0535+26 pulse phase resolved spectral parameters . . . . .	53
5.1	Daily long term light curve of <i>Swift</i> / <i>BAT</i> . . . . .	56
5.2	Daily light curve of <i>Swift</i> / <i>BAT</i> of the April 2010 outburst . . . . .	57
5.3	Fit of Tungsten line . . . . .	60
5.4	Tungsten line energy distribution . . . . .	60
5.5	<i>IBIS</i> / <i>ISGRI</i> mosaic images . . . . .	61
5.6	<i>RXTE</i> / <i>PCA</i> pulse profiles . . . . .	64
5.7	<i>RXTE</i> / <i>PCA</i> low energetic pulse profiles . . . . .	65
5.8	<i>INTEGRAL</i> pulse profiles . . . . .	66
5.9	Pulsed fraction as a function of energy . . . . .	67
5.10	Pulsed fraction as a function of flux . . . . .	68
5.11	Geometry of A 0535+26 . . . . .	70
5.12	<i>INTEGRAL</i> spectrum of rev. 0912 . . . . .	73
5.13	<i>RXTE</i> spectrum of observation 95347-02-01-01 . . . . .	74
5.14	Spectral fit parameters . . . . .	75
5.15	Contour plot in the $E_{\text{rolloff}}-\Gamma$ plane . . . . .	76
5.16	Averaged pulse profiles . . . . .	79
5.17	Pulse phase resolved analysis: fit . . . . .	80
5.18	Pulse phase resolved analysis: linear fit . . . . .	81
5.19	Pulse profiles with marked pulse phase intervals . . . . .	82
5.20	Pulse phase resolved analysis of $\Gamma$ and $E_{\text{cyc}}$ . . . . .	83
5.21	Pulse profiles of pulse amplitude resolved analysis . . . . .	85
5.22	Pulse amplitude resolved analysis: light curves . . . . .	86
5.23	Pulse amplitude distribution . . . . .	87
5.24	Pulse amplitude resolved analysis: fit parameters . . . . .	88
6.1	Her X-1 flux modulation . . . . .	95
6.2	Her X-1 35 d cycle . . . . .	96
6.3	Her X-1 pulse period evolution . . . . .	98
6.4	Her X-1 pulse profiles . . . . .	100
6.5	Her X-1 pulse profiles . . . . .	101



6.6	Her X-1 pulse profiles as a function of 35 day phase . . . .	102
6.7	Her X-1 broad band spectrum . . . . .	103
6.8	Her X-1 spectrum . . . . .	104
7.1	<i>Swift</i> / <i>BAT</i> light curves . . . . .	108
7.2	Her X-1 pulse period evolution . . . . .	109
7.3	Her X-1 <i>RGS</i> images . . . . .	111
7.4	<i>EPIC</i> extraction regions . . . . .	113
7.5	(O-C) diagram for pulse arrival times . . . . .	115
7.6	<i>XMM EPIC-pn</i> pulse profiles . . . . .	117
7.7	<i>XMM EPIC-pn</i> 4–6 keV pulse profiles . . . . .	118
7.8	<i>RGS</i> spectra . . . . .	120
7.9	<i>RGS</i> fit parameters . . . . .	121
7.10	Her X-1 <i>EPIC-MOS 1</i> , <i>-MOS 2</i> and <i>EPIC-pn</i> spectrum . .	123
7.11	<i>EPIC-pn</i> spectrum . . . . .	126
7.12	Her X-1 iron line profiles . . . . .	127
7.13	<i>EPIC-pn</i> fit parameters . . . . .	128
7.14	Her X-1 iron line fit . . . . .	129
7.15	Pulse phase resolved analysis . . . . .	131
7.16	Emission regions of Her X-1 . . . . .	136
7.17	Contributions to pulse profile of Her X-1 . . . . .	137
A.1	A 0535+26 pulse phase resolved analysis . . . . .	160
A.2	<i>EPIC-pn</i> pattern distribution plot . . . . .	162
A.3	<i>EPIC-pn</i> fit parameters of 1 Gaussian line . . . . .	163



# List of Tables

2.1	Critical luminosity . . . . .	17
3.1	<i>JEM-X</i> instrumental parameters . . . . .	34
3.2	<i>IBIS</i> instrumental parameters . . . . .	35
3.3	<i>SPI</i> instrumental parameters . . . . .	36
4.1	A 0535+26 giant outbursts . . . . .	42
5.1	Observations of the April 2010 outburst . . . . .	57
5.2	Pulse period and $T_0$ values . . . . .	62
5.3	Fit parameters . . . . .	77
5.4	Probability values of the F-test . . . . .	81
5.5	Pulse phase resolved analysis: linear fit values . . . . .	83
5.6	Pulse amplitude resolved analysis: linear fit parameters . . . . .	87
6.1	Her X-1 ephemeris . . . . .	94
7.1	Her X-1 <i>XMM-Newton</i> observations . . . . .	110
7.2	Her X-1 pulse period and $T_0$ . . . . .	115
7.3	Her X-1 X-ray emission lines . . . . .	119
7.4	Her X-1 fit parameters phase averaged spectra . . . . .	125
7.5	Her X-1 fit of 1 Gaussian line . . . . .	126
A.1	A 0535+26 <i>INTEGRAL</i> probability values . . . . .	161



# Chapter 1

## Introduction

X-ray astrophysics is still a very young field of physics. About 50 years ago, the first extrasolar X-ray emitting source Sco X-1 was detected in 1962 during a rocket experiment (Giacconi et al. 1962, 1964). X-ray observations of celestial sources can only be made using ballon or rocket experiments or by satellites since the earth's atmosphere is opaque to X-ray radiation (see Fig. 1.1). The first X-ray satellite *UHURU* (Giacconi et al. 1971b, 1972, Kellogg 1975) was launched in 1970 and discovered many bright sources (339 X-ray sources are listed in the fourth *UHURU* catalogue, Forman et al. 1978), as e.g. Cygnus X-1 or Her X-1. *UHURU* provided the first all sky survey in X-rays. Before *UHURU*, only 59 X-ray sources were known. Progress and innovation of more than 4 decades yield a number of  $\sim 1\,100\,000$ <sup>1</sup> X-ray sources in 2013.

The launch of *UHURU* initiated an age of numerous X-ray missions to observe X-ray radiation from e.g. white dwarfs, neutron stars, black holes, gamma-ray burst afterglows, active galactic nuclei, supernova remnants or hot gas in clusters of galaxies. The first imaging telescope, the *Einstein* observatory (formerly HEAO-2, in operation from 1978–1981, Giacconi et al. 1979), located thousands of X-ray sources and provided high-resolution images. The *EXOSAT* satellite (1983–1986, White & Peacock 1988) enabled continuous observations of X-ray sources and studied the transient behavior of many of these

---

<sup>1</sup>[http://heasarc.gsfc.nasa.gov/docs/heasarc/headates/how\\_many\\_xray.html](http://heasarc.gsfc.nasa.gov/docs/heasarc/headates/how_many_xray.html)

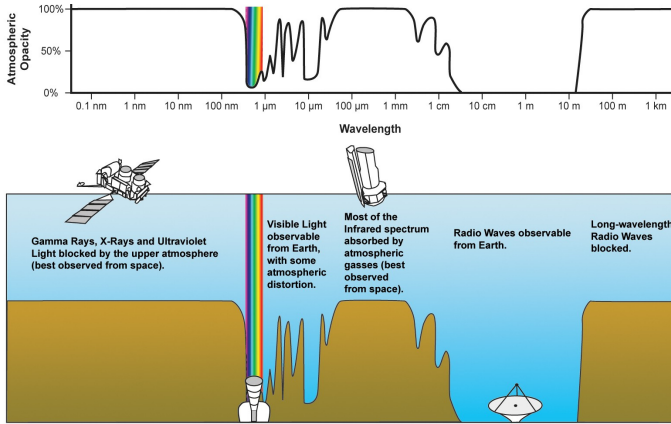


Figure 1.1: Attenuation of X-ray radiation in the earth's atmosphere. Figure is taken from NASA/IPAC.

sources. *EXOSAT* was focused on the observation of X-ray bursts and the variability of active galactic nuclei and led to the discovery of quasi-periodic oscillations. A large number of sources ( $\sim 80\,000$  X-ray sources) were detected by the *ROSAT X-ray satellite observatory* (Trümper 1984), which was in operation from 1990–1999. The X-ray observatory *RXTE* (1995–2012, Bradt et al. 1993) observed X-ray sources with an unprecedented timing resolution in the energy range  $\sim 2\text{--}200$  keV. Some highlights of the *RXTE* mission are the discovery of X-ray oscillations from accreting neutron stars and black holes and the measurement of the fastest oscillation of a black hole. *RXTE* contributed a lot to the knowledge of accreting millisecond X-ray pulsars. *BeppoSAX* (1996–2002, Boella et al. 1997) provided broad-band spectroscopy ( $\sim 0.1\text{--}300$  keV) and monitored the first X-ray follow-up observations of gamma-ray bursts.

Today, data from many X-ray observatories are available. The *Chandra X-ray observatory* (Weisskopf et al. 2002) was launched in 1999 and provides high-resolution imaging and spectroscopy. *Chandra* observes X-ray emission from very hot regions of the universe, e.g. hot gas in galaxies and clusters of galaxies, hot stars, matter around neutron stars

and black holes or supernova explosions and remnants. The large effective area and ability of long uninterrupted observations of the *XMM-Newton* observatory (1999–today, Jansen et al. 2001) allows the observation of very faint X-ray sources. *XMM-Newton* contributed to the knowledge of gamma-ray burst afterglows, supernova remnants, planetary nebula or clusters of galaxies. The *INTEGRAL* satellite (2002–today, Winkler et al. 2003) is designed for the observation of celestial gamma-ray sources and provides broad-band X-ray and gamma-ray ( $\sim 3\text{ keV}$ – $10\text{ MeV}$ ) spectra and imaging with a high resolution. *Suzaku* (formerly *Astro-E2*, 2005–today, Mitsuda et al. 2004) provides high-sensitivity broad-band high-resolution spectra in the energy range  $\sim 0.2$ – $600\text{ keV}$ . The mission contributed to the knowledge of supernovae and the black hole spin and light bending around black holes. *Swift* (2004–today, Gehrels et al. 2005) is designated to the study of gamma-ray bursts and transient sources. The observatory detected the most distant object in the universe, a gamma-ray burst with a red shift of  $\sim 8.2$  (Tanvir et al. 2009). *AGILE* (2007–today, Tavani et al. 2008) was the first mission to combine a hard X-ray ( $\sim 18$ – $60\text{ keV}$ ) and a gamma-ray ( $\sim 30\text{ MeV}$ – $50\text{ GeV}$ ) imager to study gamma-ray bursts, active galactic nuclei, supernova remnants or galactic compact objects. The *Fermi Gamma-Ray Space Telescope* (formerly *GLAST*, 2008–today, Ritz et al. 2006) operates in the  $\sim 10\text{ keV}$ – $300\text{ GeV}$  energy range and provides an unprecedented view of the high-energy gamma-ray sky. The detection of multiple gamma-ray flares from the Crab nebula is one of the highlights of the *Fermi* and *AGILE* missions. *MAXI* (2009–today, Matsuoka et al. 2009) is the first observatory that operates on the International Space Station. *MAXI* monitors, in a systematic survey, the long-term variability of X-ray sources and can alert other X-ray observatories as it detects transient X-ray events.

Amongst the variety of X-ray emitters observed by these instruments, a very interesting class of objects are accreting X-ray pulsars. Accreting X-ray pulsars are neutron stars with intense magnetic field, powered by the accretion of matter from a companion star (e.g. Giacconi et al. 1971a, Schreier et al. 1972, Tananbaum et al. 1972). The first accreting X-ray pulsars were discovered in the 1970s, when pulsations were detected for Cen X-3 (Giacconi et al. 1971a) and Her X-1 (Tananbaum et al. 1972).

Since the discovery, the knowledge about the X-ray emission of accreting X-ray pulsars improved considerably, but still, many details, e.g. on the formation of the accretion column, remain unclear.

This thesis describes the study of two accreting X-ray binary systems, A 0535+26 and Her X-1/HZ Her. We analyzed the spectral and timing properties of these two sources using data from the *RXTE*, the *INTEGRAL* and the *XMM-Newton* satellites. Chapter 2 provides an introduction to the physics of neutron stars and a review of neutron star X-ray binaries, i.e. accreting X-ray pulsars. We give an overview of the classes of neutron star X-ray binary systems, the origin of X-ray emission, of the spectral formation and of the timing properties. Chapter 3 summarizes the properties of the *RXTE*, the *INTEGRAL* and the *XMM-Newton* observatories which provided the data for our analysis. In Chapter 4, the Be/X-ray binary system A 0535+26 is described. In Chapter 5, the analysis of A 0535+26 is reported. We describe the reduction of data from the *RXTE* and *INTEGRAL* observatories and summarize and discuss the results of the timing (i.e. light curve, pulse profiles, pulsed fraction) and spectral (i.e. phase averaged, pulse phase resolved and pulse amplitude resolved spectra) analysis. Chapter 6 provides an overview of the properties of Her X-1. In Chapter 7, we describe the data reduction of the *XMM-Newton* observations. We provide and discuss the results of the timing analysis (i.e. light curve and pulse profiles) and of the analysis of pulse phase averaged spectra (*EPIC* and *RGS*) and pulse phase resolved spectra (*EPIC-pn*). Our results are summarized in Chapter 8.



# Chapter 2

## X-ray pulsars

Nearly four decades after the prediction of neutron stars in the 1930s (e.g. Landau 1932, Baade & Zwicky 1934a), the first rotation-powered pulsar was discovered by Bell and Hewish (Hewish et al. 1968). Rotation-powered pulsars are strongly magnetized neutron stars that emit strongly beamed radiation from radio to ultra-high gamma-ray energies. In the 1970s, another class of pulsars was discovered: the accreting X-ray pulsars (Giacconi et al. 1971a). These objects are powered by the conversion of gravitational energy of the accreted matter to radiation. The X-ray emission is modulated with the spin and orbital period of the system. The pulsed emission is caused by a misalignment of the magnetic field axis with respect to the rotation (spin) axis.

In this chapter, we review the physics of X-ray pulsars, i.e. neutron stars, neutron star X-ray binaries, accretion, the X-ray emission and spectral formation and the timing properties.

### 2.1 Neutron star X-ray binaries

Binary systems are composed of two stars that orbit each other around the common center of mass. One group of binaries are the X-ray binary systems. They consist of a companion star and a compact object, i.e. a white dwarf, a neutron star or a black hole. The first observational evidence of neutron star X-ray binaries were made in the beginning

of the 1970s. The X-ray satellite *Uhuru* detected pulsations in the sources Cen X-3 (Giacconi et al. 1971a, Schreier et al. 1972) and Her X-1 (Tananbaum et al. 1972). A classification as rotation-powered pulsar could be excluded due to a much larger X-ray luminosity and a long-term spin-up of the neutron star (i.e. a decrease of the pulse period). The spin-up is caused by the accretion of angular momentum of the infalling material, while rotation-powered pulsars show a spin-down due to the loss of rotational energy. The pulse periods of the neutron star in accreting X-ray binaries range between milliseconds and hundreds of seconds, the orbital periods between minutes and months (e.g. Tauris & van den Heuvel 2006). In many systems, the companion star can be detected, either with optical observations or by the Doppler shift caused by periodic orbital variations of the spin period (Mészáros 1992). In X-ray binaries, the neutron star masses  $M_{\text{NS}}$  can be derived from the analysis of the mass function plus spectroscopic observations of the companion star (e.g. Joss & Rappaport 1984, Nagase 1989). The observed masses of neutron stars in X-ray binaries are distributed around the Chandrasekhar mass  $M_{\text{Ch}} \sim 1.4 M_{\odot}$  (see Sec. 2.1.3). Some binaries show a transient behavior, i.e. exhibit outbursts during which pulsations can be detected, while other systems are quasi-steady and observable over longer timescales. Typical luminosities range between  $10^{34} - 10^{39} \text{ erg s}^{-1}$ . Reviews on observational characteristics of neutron star X-ray binaries are e.g. White et al. (1983), Joss & Rappaport (1984), Nagase (1989), Tauris & van den Heuvel (2006).

Depending on the type of the companion star, there exist different types of binary systems. High-mass X-ray binary systems (HMXBs) with either a massive early-type companion (e.g. Cen X-3, Vela X-1) or a Be-star companion (e.g. 4U 0115+63, A 0535-26) and low-mass X-ray binary systems (LMXBs), in which the companion has a lower mass (e.g. Her X-1, GX 1+4).

### 2.1.1 Low-mass X-ray binaries

LMXBs are formed by a collapsed star (black hole or neutron star) and a main sequence or white dwarf companion. In case of a main sequence companion, the star is of spectral type A or later and has a relatively small mass ( $M_{\text{star}} \leq 2 M_{\odot}$ , van Paradijs 1988). The optical counterpart

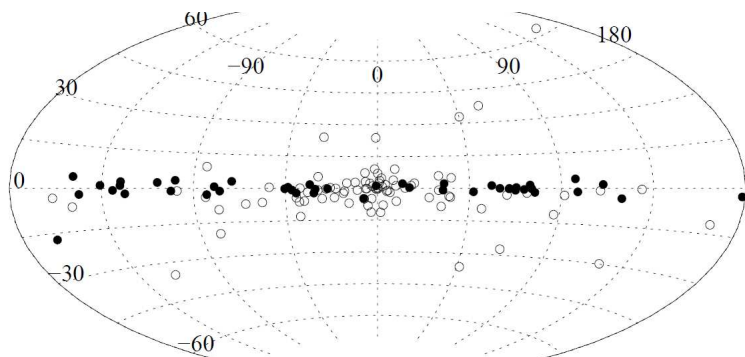


Figure 2.1: The distribution of HMXBs (filled circles) and LMXBs (open circles) in the Galaxy is shown. Figure is taken from Grimm et al. (2002).

is usually faint. The systems are much older than HMXBs (e.g. Verbunt et al. 2008) and typically concentrated in the direction of the Galactic center and in globular clusters (see Fig. 2.1). The magnetic field of the neutron star is of the order of  $\sim 10^8$  G. LMXBs are usually powered by Roche lobe overflow (see Sec. 2.2.1) and exhibit a high variability, i.e. can show different types of bursts. Type I bursts are produced by thermonuclear explosions on the neutron star surface, type II bursts are due to accretion instabilities and occur less common (Lewin et al. 1993).

### 2.1.2 High-mass X-ray binaries

HMXBs consist of a collapsed star (neutron star or black hole) and a usually giant main sequence companion of spectral type O-B with a mass of  $M_{\text{star}} > 8 - 10 M_{\odot}$  (van Paradijs 1988). HMXBs are relatively young systems with an age of  $\lesssim 10^7$  yr and usually located in the Galactic plane, along the spiral arms where the star formation takes place (see Fig. 2.1). The systems are generally fed by quasi-spherical accretion from a stellar wind (e.g. Henrichs 1983, see Sec. 2.2.1), producing X-ray luminosities of  $\sim 10^{34} - 10^{38}$  erg/s. The values for the wind velocity and the mass loss rate of the optical star can be as high as  $v_w \sim 10^3$  km s $^{-1}$  and  $\dot{M} \sim 10^{-6} M_{\odot}$  yr $^{-1}$ , respectively (e.g. Lamers et al. 1976). The magnetic field of the neutron star is of the order of  $\sim 10^{11} - 10^{13}$  G.

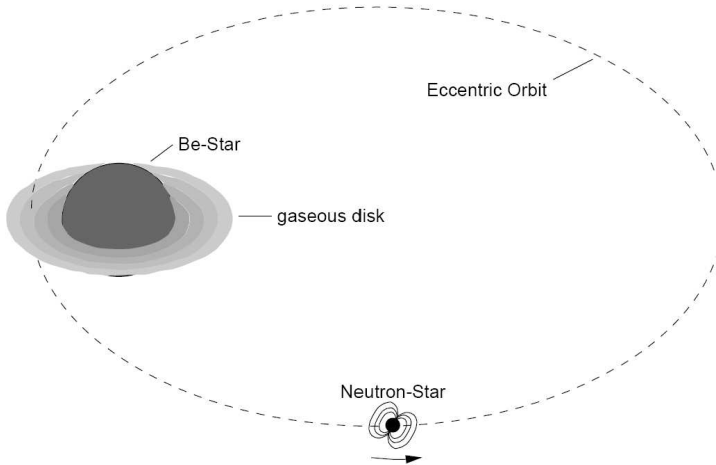


Figure 2.2: Schematic view of a Be/X-ray binary system. Figure is taken from Kretschmar (2006).

A subclass of the HMXBs are the Be/X-ray binaries (e.g. Slettebak 1988, Hanuschik 1996, Porter & Rivinius 2003, Negueruela 2004, Reig 2011, and references therein). More than half of the known HMXBs belong to the Be systems which are described in the following. The companion star is a star of spectral class B (or sometimes also late O) with a mass of  $\sim 10 - 20 M_{\odot}$  that shows spectral emission lines due to a disk of ejected material by the star. Be/X-ray binaries present a highly eccentric orbit (Fig. 2.2). The outbursts in these systems are often divided into *normal* and *giant* outbursts. Normal outbursts can repeat periodically at times close to periastron passage. The accretion rate increases by a factor of  $L_{\max}/L_{\min} \sim 100$  compared to the quiescence state due to the closer position of the neutron star to the Be star companion (Stella et al. 1986). During giant outbursts, the X-ray luminosity increases by a larger fraction ( $L_{\max}/L_{\min} \sim 100 - 1000$ ) and the outbursts can last several tens of days (Stella et al. 1986).

### 2.1.3 Neutron stars

A neutron star evolves from a supernova explosion of a massive star. At the end of life of a star, the chemical evolution progressed so far that the thermal pressure of the star cannot sustain gravitational forces anymore. The star collapses and large amounts of gravitational energy liberate within the free-fall time scale. During this supernova explosion, the star's envelope is blown away. The leftover is a neutron star (if the primary has a mass of  $M_{\text{star}} \gtrsim 8 - 10 M_{\odot}$ ), a black hole (if the primary has a mass of  $M_{\text{star}} \gtrsim 25 M_{\odot}$ ) or a white dwarf (see e.g. Mészáros 1992, Tauris & van den Heuvel 2006, and references therein). The latter can again evolve to a neutron star after an accretion-induced collapse. The subsequent evolution of a single star depends on the initial stellar masses (e.g. Lewin et al. 1995). If the mass of the star is slightly above  $9 M_{\odot}$  (Woosley & Weaver 1986), the CO core mass exceeds the Chandrasekhar mass of  $M_{\text{Ch}} \sim 1.4 M_{\odot}$ , the maximum mass for a stable white dwarf (Chandrasekhar 1931, 1935). The core then undergoes a gravitational collapse. If  $M_{\text{star}} \gtrsim 9 M_{\odot}$  (e.g. Woosley & Weaver 1986), further nuclear reactions are possible. The final collapse can be stopped by the degeneracy of neutrons. If the mass of the core  $M_{\text{core}} < 4 M_{\odot}$ , the star evolves to a neutron star. Otherwise, a black hole is formed by the onset of a general relativistic instability.

As for a white dwarf, the basic physical parameters of a neutron star can be calculated considering that the collapse of a supernova is stopped by the degeneracy pressure of particles. Chandrasekhar (1935) calculated the maximum mass of a white dwarf in which the gravitational pressure is balanced by the degeneracy pressure of electrons. The dimensions for the radius and the magnetic field of a white dwarf are:  $R \sim 10^9$  cm,  $B \leq 10^6 - 10^7$  G. For neutron stars, one must consider the degeneracy of neutrons since protons absorb most of the electrons (Landau 1932, Baade & Zwicky 1934a,b, Oppenheimer & Volkoff 1939). Following basic physical parameters can be estimated:  $R \sim 10^6$  cm,  $B \sim 10^{12} - 10^{13}$  G,  $M \sim 1.4 M_{\odot}$ .

## 2.2 Accreting X-ray pulsars

Accretion-powered pulsars are powered by the conversion of the gravitational energy of accreted matter to radiation. The accretion luminosity can be calculated as

$$L_{\text{acc}} = \frac{dE_{\text{acc}}}{dt} = \frac{GM\dot{m}}{R} \quad (2.1)$$

with the gravitational constant  $G$ , the mass  $M$  and radius  $R$  of the accretor and the mass accretion rate  $\dot{m}$ . The luminosity is thus directly coupled to the mass accretion rate until reaching a critical luminosity, referred to as the Eddington luminosity  $L_{\text{Edd}}$ ,

$$L_{\text{Edd}} = \frac{4\pi GMm_{\text{p}}c}{\sigma_{\text{T}}} = 1.26 \times 10^{38} \left( \frac{M}{M_{\odot}} \right) \text{ erg s}^{-1}, \quad (2.2)$$

where  $m_{\text{p}}$  is the proton mass,  $c$  the speed of light and  $\sigma_{\text{T}}$  the Thompson cross section. Above  $L_{\text{Edd}}$ , the accretion of matter is prevented since the radiation pressure is larger than the gravitation.  $L_{\text{Edd}}$  represents the maximum luminosity for spherically symmetric accretion. In spherically non-symmetric case, it correlates with the fraction of area on the neutron star surface where the accreted matter is funneled.

### 2.2.1 The accretion flow in the magnetosphere

There exist two types of accretion depending on the distance at which matter is gravitationally captured by the neutron star and on the angular momentum of the matter: disk accretion and quasi-spherical accretion from a stellar wind. These two types of accretion are described in the following sections. A special case are the Be/X-ray binary systems (see Sec. 2.1.2).

#### Disk accretion

Disk accretion is typical for binaries with a low-mass companion. Matter can be gravitationally captured by the neutron star when the atmosphere/envelope of the companion fills its Roche lobe. The Roche lobe is the equipotential surface of the binary system in the frame rotating

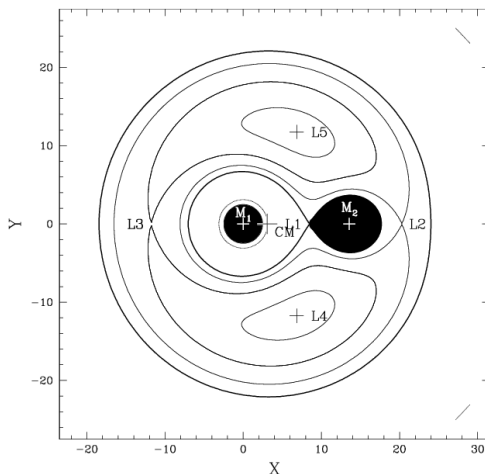


Figure 2.3: The equipotential lines of a binary system are shown. The Roche lobe is the equipotential line that goes through the inner Lagrangian point  $L_1$ . Matter on the Roche lobe can be accreted through  $L_1$  if the companion fills its Roche lobe. Figure is taken from Carrier et al. (2003).

with the binary, that connects the gravitational potentials of both stars (Fig. 2.3). If the two stars are approximated by point masses, the equipotential lines are given by (Roche 1873)

$$\phi = \frac{GM_1}{r_1} + \frac{GM_2}{r_2} - \frac{1}{2}\omega^2 r^2 = \text{constant} \quad (2.3)$$

with  $r_1$ ,  $r_2$  being the distances to the center of mass of the two stars,  $\omega^2 r^2$  - the centrifugal potential because of the binary motion,  $r$  - the distance to the rotation axis and  $\omega$  - the angular velocity of the binary system.

The accreted matter remains in a circular orbit because the angular momentum of the particles is too high for the matter to be directly accreted by the neutron star. The circulation radius  $R_{\text{circ}}$  is given by (Pringle 1981)

$$R_{\text{circ}} = \frac{J^2}{GM} \quad (2.4)$$

with the angular momentum  $J$  of the particle and the mass  $M$  of the neutron star. Due to viscosity, the matter loses angular momentum to sink closer in the gravitational well of the neutron star. An accretion disk is formed by streams of accreted matter, spiraling inwards. The physics of accretion disks is discussed in e.g. Shakura & Sunyaev (1973), Pringle (1981), Frank et al. (1985).

### Quasi-spherical accretion

Quasi-spherical accretion from a stellar wind might take place if the companion does not fill its Roche lobe or is of an early type and emitting a stellar wind (Fig. 2.4). Matter can be gravitationally captured from a cylinder with radius  $r_{\text{acc}}$  (Bondi & Hoyle 1944, Davidson & Ostriker 1973, Henrichs 1983, Blondin et al. 1990):

$$r_{\text{acc}} = \xi \frac{2GM}{(v_{\text{rel}}^2 + c_s^2)} \approx 2.65 \times 10^{10} \times M \left[ \frac{v_{\text{rel}}^2 + c_s^2}{1000 \text{ km s}^{-1}} \right]^{-1} \text{ cm} \quad (2.5)$$

with the geometry factor  $\xi \sim 1$ , the neutron star mass  $M$ , the speed of sound  $c_s$ , the relative velocity between neutron star and gas  $v_{\text{rel}}$ . The dimension of the accretion radius is  $\sim 10^{10}$  cm for typical parameters of HMXBs. This is about two magnitudes smaller compared to a binary separation of  $a \sim 10^{12}$  cm, thus only a fraction of the wind can be accreted.

The accretion rate (Bondi rate) for quasi-spherical accretion is given by (Bondi & Hoyle 1944, Davidson & Ostriker 1973):

$$\dot{M} = \frac{\dot{M}_{\text{w}}}{\Omega a^2} \times (\pi r_{\text{acc}}^2). \quad (2.6)$$

The first part of equation (2.6) describes the wind flux at a distance  $a$  from the companion star with  $\Omega = 4\pi$  for isotropic winds. The second part gives the capture cross section.

The accretion is described by the Bondi-Hoyle-Littleton accretion theory



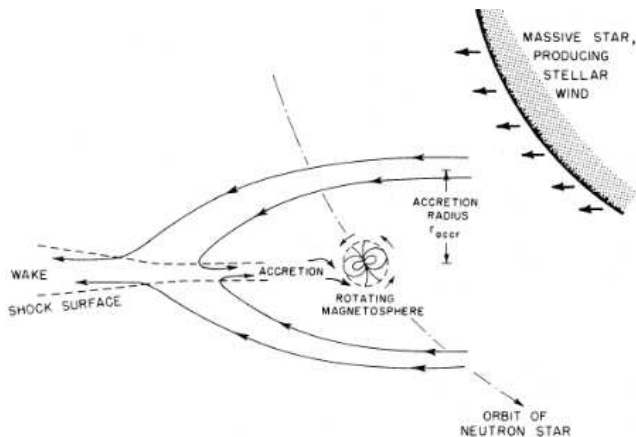


Figure 2.4: The quasi-spherical accretion from a stellar wind of a companion onto a neutron star is illustrated. Figure is taken from Davidson & Ostriker (1973).

(Bondi 1952, Bondi & Hoyle 1944, Hoyle & Lyttleton 1941).

For quasi-spherical accretion, the angular momentum of the captured material is lower compared to accretion via Roche lobe overflow, such that the condition for the disk formation ( $R_{\text{circ}} > R_{\text{NS}}$ ) is not always fulfilled.

### Accretion flow

At the magnetospheric radius  $r_m$  (or Alfvén radius,  $r_m \sim 10^8$  cm for typical neutron star parameters, Lamb et al. 1973), the matter is stopped by the growing magnetic pressure and funneled along the magnetic field lines onto the neutron star’s magnetic poles (Fig. 2.5, 2.6). Beyond  $r_m$ , the accretion flow can be quasi-spherically symmetric (e.g. accretion from a stellar wind if accreted matter has a low angular momentum) or an accretion disk can be formed (e.g. for Roche lobe overflow).

$r_m$  can be calculated for spherically symmetric accretion by equating the ram pressure of the infalling material with the pressure of the magnetic field  $B$ ,

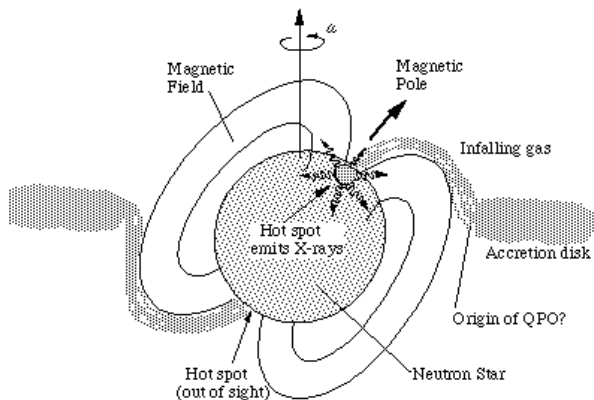


Figure 2.5: The accretion in the magnetic field of a neutron star is illustrated. Figure is taken from [http://heasarc.gsfc.nasa.gov/Images/xte/xray\\_pulsar.gif](http://heasarc.gsfc.nasa.gov/Images/xte/xray_pulsar.gif).

$$\rho v_r^2 \approx \frac{B^2}{8\pi}, \quad (2.7)$$

yielding a magnetospheric radius of (Lamb et al. 1973)

$$r_{m,\text{symm}} \approx 2.6 \times 10^8 \mu_{30}^{4/7} (M/M_\odot)^{1/7} L_{37}^{-2/7} R^{-2/7} \text{ cm} \quad (2.8)$$

with the magnetic moment  $\mu_{30} = BR^3$  in terms of the surface magnetic field in units of  $10^{30} \text{ G cm}^3$ , the stellar radius  $R$  in units of 10 km, the stellar mass  $M$  and the luminosity  $L_{37}$  in units of  $10^{37} \text{ erg s}^{-1}$ .

For disk accretion, this formula is slightly modified (Lamb & Pethick 1974, Kiraly & Meszaros 1988, Lamb 1988).

The corotation radius  $r_{\text{co}}$  is specified as the distance where the centrifugal force equals gravity, i.e. the angular velocity of the magnetosphere equals the Keplerian velocity of the disk:

$$r_{\text{co}} = \left( \frac{GM}{\Omega_s^2} \right)^{1/3}, \quad (2.9)$$

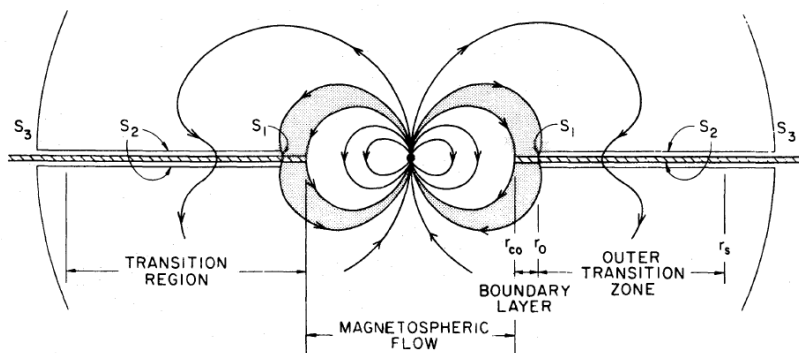


Figure 2.6: The transition region of the accretion flow is shown. In the boundary layer, the magnetic field dominates the accretion flow. Figure is taken from Ghosh & Lamb (1979b).

with  $\Omega_s$  being the angular velocity of the neutron star.

For  $r_m > r_{co}$ , i.e. when the neutron star rotates faster than the Keplerian disk at the magnetospheric radius, a centrifugal barrier arises. In this case, accretion is prohibited and matter can be thrown out. This is called the propeller effect (Illarionov & Sunyaev 1975). For  $r_m < r_{co}$ , i.e. when the angular velocity of the neutron star is smaller than the Keplerian velocity of the disk at its inner radius, matter can be accreted.

## 2.2.2 The accretion column

At  $r \sim r_m$ , the accreted matter is funneled along the magnetic field lines and moves down to the magnetic poles in a more or less azimuthally symmetric column (Fig. 2.7). In this region, the flow of matter is completely governed by the magnetic field. The X-ray emission is produced close to the surface of the neutron star in a region of  $\sim 0.1 R_{NS} \sim 1 \text{ km}^2$  (Davidson & Ostriker 1973). The exact shape of the column and the physics behind the formation are still unclear. Different models of the geometry of accretion columns are discussed, e.g. the formation of a hollow column, a partial hollow or a filled column (e.g. Basko & Sunyaev 1976b, Meszaros 1984). The accreted gas has a

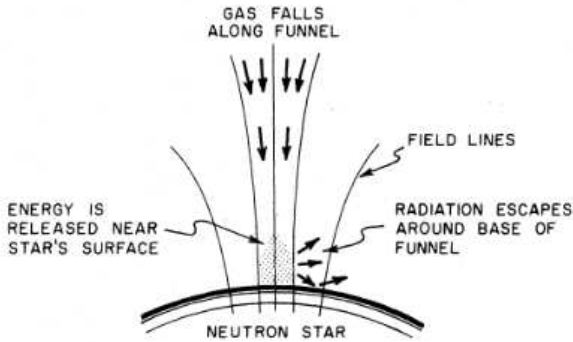


Figure 2.7: The accretion funnel close to the magnetic pole of the neutron star. Figure is taken from Davidson & Ostriker (1973).

temperature  $T \leq \text{few keV}$  when it couples to the magnetic field lines at  $r_m$  (e.g. Basko & Sunyaev 1976a, Syunyaev 1976). The gas cools while moving inwards to the magnetic poles and radiates via synchrotron radiation and inverse Compton effect. Close to the magnetic poles, the cooled down gas is decelerated in a radiation-dominated or a collisionless shock above the surface of the neutron star or through Coulomb or nuclear collisions in its atmosphere.

The geometry of the polar emitting structure is expected to depend on the mass accretion rate. Basko & Sunyaev (1976b) introduced a critical luminosity  $L_{\text{crit}}$ . In the following, X-ray pulsars with a luminosity that exceeds  $L_{\text{crit}}$  are called *super-critical* sources, those with a luminosity smaller than  $L_{\text{crit}}$  – *sub-critical* sources. The critical luminosity  $L_{\text{crit}}$  depends strongly on the properties of the pulsar.

The critical luminosity is associated with the transition between two accretion scenarios. For higher luminosities,  $L > L_{\text{crit}}$ , a radiation shock forms and the pressure of the radiation field is big enough to decelerate the infalling gas to rest at the stellar surface. For lower luminosities,  $L < L_{\text{crit}}$ , the final deceleration occurs via Coulomb interactions (Becker et al. 2012). Recent theoretical calculations of the critical luminosity  $L_{\text{crit}}$  by Becker et al. (2012) report a value of

Table 2.1: Critical luminosity for a long-term phase-averaged study for several cyclotron line sources from Becker et al. (2012).

source	$L_{\text{crit}} [10^{37} \text{ erg/s}]$
4U 0115+63	2.24
V 0332+53	4.06
Her X-1	6.11
A 0535+26	6.78
GX 304-1	8.30

$$L_{\text{crit}} = 1.49 \times 10^{37} \text{ erg s}^{-1} \left( \frac{\Lambda}{0.1} \right)^{-7/5} w^{-28/15} \times \left( \frac{M_*}{1.4 M_{\odot}} \right)^{29/30} \left( \frac{R_*}{10 \text{ km}} \right)^{1/10} \left( \frac{B_*}{10^{12} \text{ G}} \right)^{16/15} \quad (2.10)$$

where  $\Lambda$  is a constant with  $\Lambda = 1$  for spherical accretion and  $\Lambda < 1$  for disk accretion, the index  $w$  describes the spectrum and ranges between  $w \sim 1$  for bremsstrahlung and  $w \sim 3$  for a Planck spectrum and  $M_*$ ,  $R_*$ ,  $B_*$  are the parameters for the mass, radius and magnetic field of the neutron star.

For typical neutron star parameters ( $M_*=1.4 M_{\odot}$ ,  $R_*=10 \text{ km}$ ) and using  $\Lambda = 0.1$  and  $w=1$ , assuming that the spectrum inside the column is dominated by bremsstrahlung emission (Becker & Wolff 2007), the equation can be written as

$$L_{\text{crit}} = 1.49 \times 10^{37} \text{ erg s}^{-1} B_{12}^{16/15}. \quad (2.11)$$

Under the previous assumptions, Becker et al. (2012) calculated  $L_{\text{crit}}$  for some known cyclotron line sources. The values are shown in Table 2.1. The calculations by Becker et al. (2012) are based on several assumptions, e.g.  $L_{\text{crit}}$  is associated with the Eddington limit (see (2.2)) and mixed polarization states and resonances in the cross section are not taken into account. Mushtukov et al. (2014) calculate  $L_{\text{crit}}$  based on the model by Basko & Sunyaev (1976b), in which the value for  $L_{\text{crit}}$  is not connected

to  $L_{\text{Edd}}$ . Here,  $L_{\text{crit}}$  is calculated as a function of the magnetic field by using the exact Compton scattering cross section in a strong magnetic field. The influences of resonant scattering, of polarization and of the geometry of the accretion stream are considered.

## 2.3 Properties of accreting X-ray pulsars

### 2.3.1 Spectral formation

The X-ray spectrum of an accreting pulsar is generally modeled by different components: a power law continuum with a cutoff at around 20–30 keV, a blackbody component at lower energies, a Fe K $\alpha$  fluorescent emission line at  $\sim 6.4$  keV and often a cyclotron resonant scattering feature (CRSF) (e.g. Becker & Wolff 2005). The principal mechanism that powers the X-ray emission is conversion of gravitational potential energy to radiation. As the gas couples to the magnetic field lines at  $r_m$ , it has a temperature of  $\leq$  few keV (e.g. Basko & Sunyaev 1976a, Sunyaev 1976). The emitted radiation is upscattered (Comptonized) to higher energies by infalling electrons via bulk and thermal Comptonization processes and then eventually escapes through the column walls or top, carrying away kinetic energy (Ostriker & Davidson 1973, Becker & Wolff 2007, Becker et al. 2012). A part of the emitted radiation might also be reflected on the neutron star surface. The accreted gas falls down on the pole with velocities of  $\sim 0.6 c$  and does not equilibrate during the accretion process (Becker et al. 2012).

Cyclotron lines are an important diagnostic tool and provide the only direct measurement of the magnetic field of a neutron star. The first cyclotron line was discovered in Her X-1 (Trümper et al. 1978), and since then in  $\sim 20$  systems. Caballero & Wilms (2012), Pottschmidt et al. (2012) give an overview of the observational status of cyclotron lines. Cyclotron lines are absorption-like features in the X-ray spectrum, formed due to resonant scattering of photons on electrons (e.g. Nagel 1981). The energy distribution of electrons propagating parallel to the magnetic field is thermal, while the energies of electrons propagating perpendicular to the magnetic field are quantized into discrete energy levels (Landau levels). The energy levels are given by (Daugherty & Harding 1986,

Mészáros 1992)

$$E_n = m_e c^2 \frac{\sqrt{1 + 2n \frac{B}{B_{\text{crit}}} \sin^2 \Theta} - 1}{\sin^2 \Theta} \quad (2.12)$$

with  $B_{\text{crit}} = \frac{m_e c^3}{e \hbar} \sim 4.4 \times 10^{13}$  G being the quantum-electrodynamical critical magnetic field at which the energy of the electron equals the electron rest mass  $m_e c^2$ ,  $m_e$  the electron mass and  $\Theta$  the angle between the photon direction and the magnetic field.

At these energies, the cross section for scattering of photons on electrons is highly increased. For  $B \ll B_{\text{crit}}$ , the Landau levels have an energy difference of

$$E_{\text{cyc}} = \frac{\hbar e}{m_e c} B = 11.6 \text{ keV} \left( \frac{B}{10^{12} \text{ G}} \right). \quad (2.13)$$

Due to the large gravitational red shift, the observed  $E_{\text{cyc}}$  is shifted from the value in (2.13) as

$$E_{\text{cyc,obs}} = \frac{E_{\text{cyc}}}{1 + z} \quad (2.14)$$

where  $1 + z = \left(1 - \frac{2GM}{Rc^2}\right)^{-1/2}$  is the gravitational red shift correction with the mass  $M$  and radius  $R$  of the star. For typical neutron star parameters the red shift is  $z \sim 0.3$ .

Photons with an energy of  $E_n = n E_{\text{cyc}}$  ( $n=1,2,3,\dots$ ) are scattered on the Landau electrons. These photons are absorbed by the Landau electrons and can leave the accretion column only after undergoing several scattering (absorption and re-emission) processes, hence when their energy differs sufficiently from the energies of the Landau levels.

The shape of cyclotron lines is complex (e.g. Schönherr et al. 2007) but in general can be modeled with a Gaussian or Lorentzian profile since the complex shape cannot be resolved in the observation.  $E_{\text{cyc}}$  depends on the pulse phase, caused by a dependence of the scattering cross section on the scattering angle and on the luminosity, related to a change of the geometry of the region where the line is produced.

The formation of cyclotron line in the spectra of accreting X-ray pulsars and its dependence on flux is still subject of discussion. Different models

are proposed to explain the observed variation of the line centroid  $E_{\text{cyc}}$ . In the following section, we describe possible accretion scenarios for *sub-* and *super-critical* sources (see Sec. 2.2.2).

In the super-critical accretion regime, the total pressure is dominated by radiation pressure and the matter is decelerated in a vertically extended region referred to as "radiative shock" (see Fig. 2.8, plot *d*, Becker et al. 2012). This region can be located a few kilometers above the stellar surface. When the accreted gas passes the deceleration region, the free-falling plasma is slowed down by scattering processes with the escaping photons and the velocity is reduced by a factor of  $\sim 7$  (Basko & Sunyaev 1976b). Below the shock, the matter is further decelerated in the *sinking zone* where it loses the remaining momentum and radiates sideways through the column walls (Basko & Sunyaev 1976b). Becker et al. (2012) argue that the characteristic emission height  $h_c$ , where most of the radiation is emitted, is much lower than that of the shock and changes proportional to the luminosity of the source. With increasing luminosity, the height of the emission region is also increasing, moving towards the region with a lower magnetic field. This is reflected in the behavior of the cyclotron line energy, which decreases with increasing source flux, i.e. is negatively correlated with flux (see Fig. 2.9). This was observed for V 0332+53 (Mowlavi et al. 2006, Tsygankov et al. 2006, 2007, 2010).

However, this model has problems to explain the observed variation of  $E_{\text{cyc}}$  for high luminosities. The large gradient of magnetic field strength within the line-forming region complicates the detection of a line-like feature and the observed variation of  $E_{\text{cyc}}$  is much smaller than expected from the model. An alternative model for the CRSF formation is suggested by Poutanen et al. (2013). Here, the cyclotron line is formed by reflection of emitted radiation from the accretion column on the neutron star surface, where the gradient of magnetic field strength is smaller. An increase of the mass accretion rate, i.e. the luminosity, is reflected by a higher accretion column. The fraction of intercepted column radiation depends on the height of the accretion column. For high accretion rates, the accretion column is high and a large part of the stellar surface can be illuminated (Fig. 2.10). While for low accretion rates, only the region around the magnetic poles is illuminated. The reflected spectrum



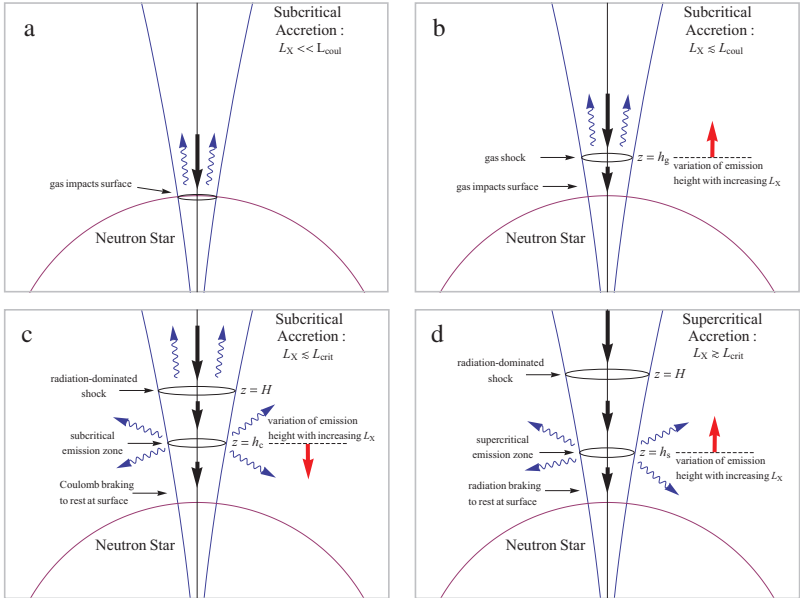


Figure 2.8: Accretion scenario for different source luminosities. The shock height  $H$  and the variation of the characteristic emission height  $h_c$ , where the largest part of the radiation is emitted, are shown. Figure is taken from Becker et al. (2012).

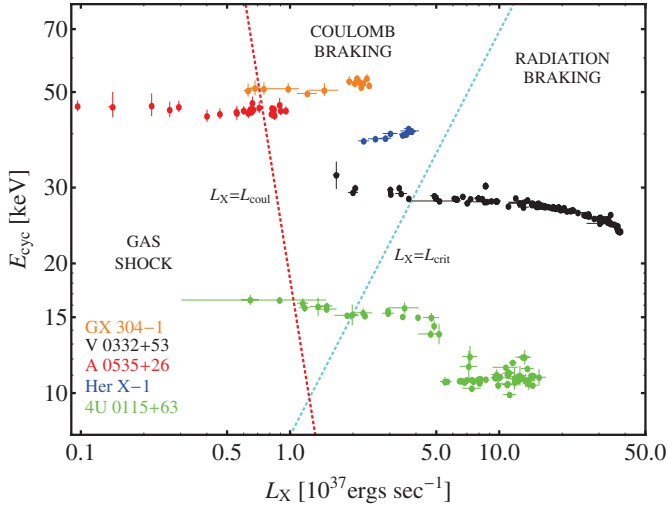


Figure 2.9: Dependencies of the long-term cyclotron line energy on the source luminosity for a number of known cyclotron line sources. Three regions are indicated: at low luminosities, the infalling gas is mainly decelerated in a gas shock, while for higher luminosities, the final deceleration occurs via Coulomb braking. For very high luminosities, the accreted matter is stopped in a radiative shock. For 4U 0115+63, however, Müller et al. (2013b) showed that the correlation strongly depends on the modeling of the continuum. Figure is taken from Becker et al. (2012).

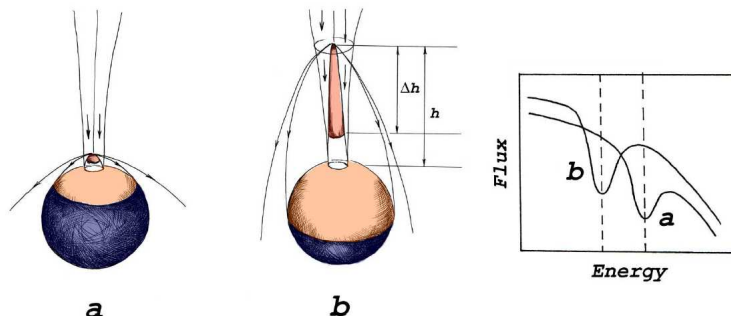


Figure 2.10: The accretion scenario is shown for two different luminosities, i.e. accretion column heights. The intercepted radiation on the neutron star surface depends on the height of the accretion column. a) The region around the magnetic pole is illuminated by a small accretion column. b) The accretion column and thus the illuminated fraction on the neutron star surface is higher, causing a lower CRSF due to a lower averaged magnetic field strength. The spectrum (*right*) shows schematically the shift of  $E_{cyc}$  for the two luminosity states. Figure is taken from Poutanen et al. (2013).

shows a CRSF at the energy corresponding to the local magnetic field strength, thus can vary between a value corresponding to the magnetic field strength at the magnetic pole and a value averaged over the whole surface of the neutron star. A negative correlation between  $E_{cyc}$  and flux is expected.

In sub-critical sources, the pressure of the radiation field is not large enough to decelerate the infalling plasma to zero at the stellar surface (Becker et al. 2012). The final stopping probably occurs via Coulomb interactions at the base of the accretion column (see Fig. 2.8, plot *c*, Becker et al. 2012) (Basko & Sunyaev 1976b, Staubert et al. 2007). The characteristic emission height is the height where the Coulomb interactions begin to decelerate plasma and is found to be proportional to  $L_x^{-5/7}$  (Becker et al. 2012). The height of the emitting region decreases with increasing luminosity since the ram pressure of the infalling material grows (Staubert et al. 2007, Becker et al. 2012). Therefore, the energy

of the cyclotron line is positively correlated (i.e. increases) with the luminosity of the source (see Fig. 2.9). This behavior was found for the accreting pulsars Her X-1 (Staubert et al. 2007), GX 304-1 (Klochkov et al. 2012), A 0535+26 (Klochkov et al. 2011) and Vela X-1 (Fürst et al. 2014).

## 2.3.2 Timing properties

### Accretion torques

The pulse period evolution is subject to internal and external torques. Angular momentum can be transferred from the disk to the magnetospheric boundary layer close to  $r_m$  as the magnetosphere of a neutron star couples magnetically to matter in the accretion disk (e.g. Ghosh & Lamb 1979b, Nagase 1989). The strength of the external torque depends on the magnetic field configuration and on the geometry of the accretion flow. For accretion from a stellar wind, it is rather difficult to determine the sign and value of the torque because the angular momentum of the accreted material is uncertain. Pringle & Rees (1972) calculate the torque for disk accretion, assuming the inner edge of the accretion disk at  $r_m$  and the material moving with the Keplerian velocity:

$$K_0 = (GMr_m)^{1/2} \dot{M}. \quad (2.15)$$

The resulting torque on the neutron star is related to the dimensions of the magnetospheric ( $r_m$ ) and corotation ( $r_{co}$ ) radius and can be calculated as

$$K \approx n(\omega_s) K_0 \quad (2.16)$$

where  $n(\omega_s)$  is a dimensionless function whose sign changes depending on the fastness parameter  $\omega_s$ . The parameter  $\omega_s$  is defined as the ratio of the stellar angular velocity  $\Omega_s$  and the Keplerian angular velocity  $\Omega_K$  at  $r_m$  (Elsner & Lamb 1977):

$$\omega_s = \frac{\Omega_s}{\Omega_K(r_m)} = \left( \frac{r_m}{r_{co}} \right)^{3/2}. \quad (2.17)$$

A spin-up of the neutron star (i.e. decrease of pulse period) can occur

for  $\omega_s \ll 1$ , while for  $\omega_s > \omega_c$  (with  $\omega_c = 0.8 - 0.9$  being the critical value for the fastness parameter, Lamb 1988) the neutron star spins-down. For higher values of  $\omega_s$  ( $\omega_s > 1$ ) accretion is prevented and matter centrifugally ejected (Ghosh & Lamb 1978). The parameter  $\omega_s$  depends on  $r_m$  and therefore on the accretion rate, the magnetic field strength and the geometry of the magnetic field. Ghosh & Lamb (1979b) calculate an equation for the pulse period change for disk accretion:

$$-\dot{P} = n(\omega_s) f_2(\mu, M) P^2 L_{37}^{6/7}, \quad (2.18)$$

where  $f_2$  is a dimensionless function of the magnetic moment  $\mu$  and the mass  $M$ , and  $L_{37}$  is the luminosity in units of  $10^{37} \text{ erg s}^{-1}$ . More specific studies on disk torques are e.g. Ghosh & Lamb (1978, 1979a,b).

Usually, the pulse period shows a long-term spin-up caused by accretion torques (e.g. Joss & Rappaport 1984, Nagase 1989). Typical pulse period changes are of the order of  $\dot{P}/P \sim 10^{-2} - 10^{-5} \text{ yr}^{-1}$ . In some objects (short) spin-down episodes are observed (e.g. Her X-1, Cen X-3). A possible explanation for this behavior can be ejection of matter or a decrease of the mass transfer rate from the donor star.

Interactions, e.g. between core and crust, in the interior of a neutron star can also become noticeable as short time scale fluctuations (hours to months), leading to internal torques (e.g. Boynton et al. 1984, 1986, Lamb et al. 1988, Deeter et al. 1989).

## Pulse profiles

Characteristics on the emission geometry of pulsars can be investigated by analyzing pulse profiles, obtained by folding of the X-ray light curve with the pulse period. The bulk of X-ray radiation is produced close to the neutron star surface and is influenced by the angle and frequency dependent opacity. Therefore, the pulse shape depends (strongly) on the energy band (see e.g. Fig. 2.11). Since the accretion scenario/geometry changes with luminosity (e.g. Sec. 2.3.1), the pulse profile shape also depends on the luminosity of the pulsar. Typically, the pulse maximum and minimum are shifted in phase by a factor 0.5. During the minimum the intensity does not drop to zero but a (significant) fraction of emission is observed. The variety of pulsars is reflected in a number of differing

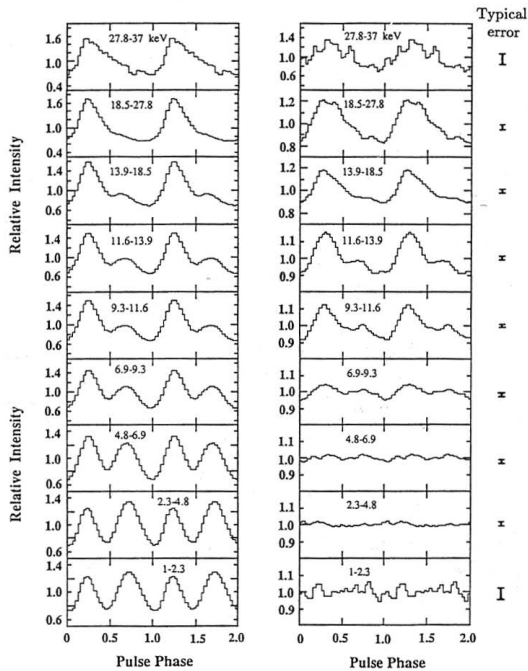


Figure 2.11: Pulse profiles of Cen X-3 for different energy bands (energy increases from bottom to top) taken during the high-on noneclipse phase (*left*) and the pre-eclipse phase (*right*) of the source. Figure is taken from Nagase et al. (1992).

pulse profile shapes. Pulse profiles can be single- or double-peaked or evolve from a single- to double-peaked structure or vice versa. Sometimes, asymmetric single peaks are observed. At low energies, many sources exhibit a variety of complex pulse shapes.

In some systems (e.g. Her X-1, Cen X-3, A 0535+26, V 0332+53), the pulse shape changes on time scales of individual pulses (e.g. Staubert et al. 1980, Frontera et al. 1985). This pulse-to-pulse variability can yield information about the interaction of the neutron star's magnetosphere with the surrounding material, especially at higher energies when the

effects of absorption become negligible.





# Chapter 3

## Satellites

### 3.1 *RXTE*

The Rossi X-ray Timing Explorer *RXTE* observes the sky in a broad energy band of 2–200 keV (Bradt et al. 1993). The instrument is designed for the observation of bright X-ray sources in a wide energy range and with a time resolution of microseconds. *RXTE* monitors the timing properties of transient sources and keeps track of the long-term behavior of other bright X-ray sources. The observatory consists of three instruments: the All-Sky-Monitor *ASM* (Levine et al. 1996), the Proportional Counter Array *PCA* (Jahoda et al. 1996) and the High Energy X-ray Timing Experiment *HEXTE* (Gruber et al. 1996, Rothschild et al. 1998). A schematic drawing of the observatory is shown in Figure 3.1.

#### 3.1.1 *ASM*

The All-Sky-Monitor *ASM* scans the entire sky every 90 minutes (Levine et al. 1996). One of the main objectives of the *ASM* is to keep track of long-term intensity changes of X-ray sources. But also short-term variations of the behavior of transient X-ray sources, e.g. start of outbursts, can be tracked (Levine et al. 1996). The instrument consists of 3 Scanning Shadow Cameras *SSCs*, each with a position-sensitive

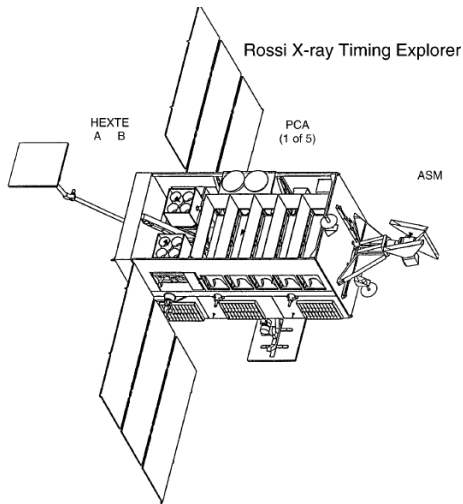


Figure 3.1: The *RXTE* satellite. Figure is taken from Rothschild et al. (1998).

proportional counter and a slit mask (Levine et al. 1996). The counters are filled with a xenon-CO<sub>2</sub> mixture and each of them is fragmented into 8 carbon-coated quartz fiber anodes (Levine et al. 1996). The field of view of each *SSC* is  $6^\circ \times 90^\circ$  FWHM (Full Width at Half Maximum) and the respective effective area is  $\sim 10 \text{ cm}^2$  @ 2 keV,  $\sim 30 \text{ cm}^2$  @ 5 keV and  $\sim 23 \text{ cm}^2$  @ 10 keV (Levine et al. 1996). The *ASM* is sensitive from 1.5–12 keV (Levine et al. 1996). The data are compressed by two Event Analyzers and processed with the Experiment Data System *EDS* aboard *RXTE* (Bradt et al. 1993).

### 3.1.2 *PCA*

The Proportional Counter Array *PCA* observes the sky in the 2–60 keV energy band (Jahoda et al. 1996). A schematic drawing of the detector is shown in Figure 3.2. The *PCA* consists of 5 detector units that altogether have an effective area of  $6250 \text{ cm}^2$  (Bradt et al. 1993). The 5 Proportional Counter Units (*PCUs*) are filled with xenon gas and have an

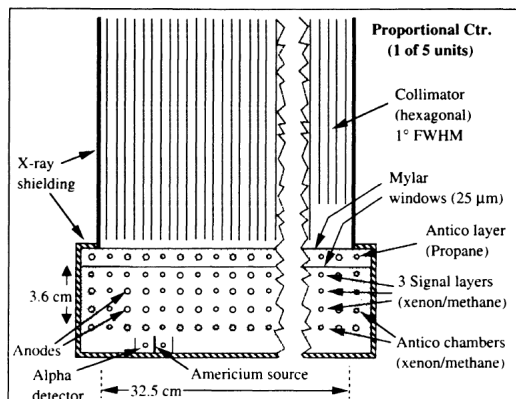


Figure 3.2: The *PCA* detector. Figure is taken from Bradt et al. (1993).

anticoincidence system and a propane top layer to reduce the background. For further background reduction, a collimator is used which narrows the field of view to  $1^\circ$  FWHM (Bradt et al. 1993). The energy resolution of the *PCA* is  $18\%$  @  $6\text{ keV}$  (Bradt et al. 1993). As for the *ASM*, the data are processed by the *EDS* and compressed by 6 Event Analyzers (Bradt et al. 1993).

### 3.1.3 *HEXTE*

The High Energy X-ray Timing Explorer *HEXTE* is the high energy detector of *RXTE* (Gruber et al. 1996, Rothschild et al. 1998). The instrument operates in the  $15\text{--}250\text{ keV}$  energy range with an energy resolution of  $\sim 17\%$  @  $60\text{ keV}$  (Rothschild et al. 1998). Figure 3.3 gives an overview of the instrument. *HEXTE* consists of 2 independent clusters, *HEXTE A* and *HEXTE B*, that together have a total effective area of  $1600\text{ cm}^2$  (Rothschild et al. 1998). Each cluster contains 4 NaI/CsI phoswich scintillation detectors that are optically coupled to photomultiplier tubes (Rothschild et al. 1998). Besides collecting primary light from the NaI scintillation crystals, NaI also works as an active anticoincidence shield (Rothschild et al. 1998). The calibration is done

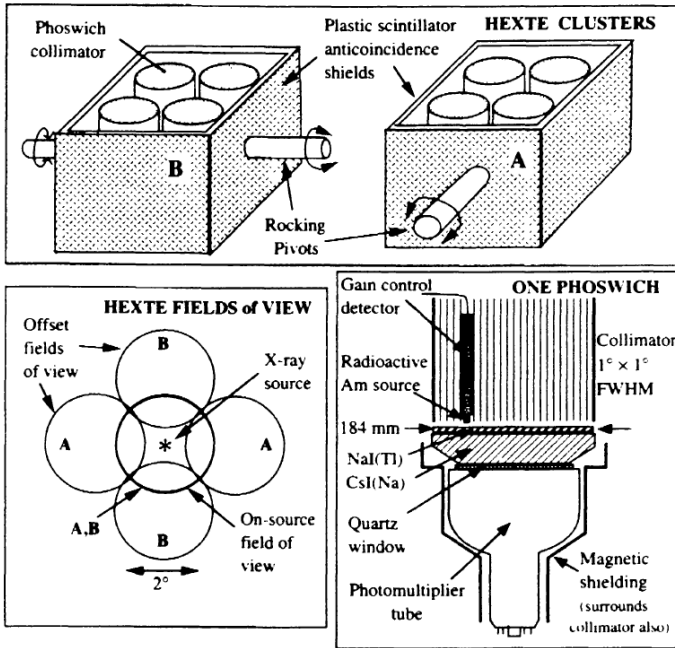


Figure 3.3: The *HEXTE* detector. In the *upper* plot the two clusters *HEXTE A* and *HEXTE B* are illustrated. In the figures beneath, the *HEXTE* fields of view and the schematic layout of a phoswich detector is shown. Figure is taken from Bradt et al. (1993).

with an  $^{241}\text{Am}$  source (Rothschild et al. 1998). The collimators confine a field of view of  $1^\circ$  for each cluster (Rothschild et al. 1998). For a continuous monitoring of source and background, the two clusters rock on source and off source every  $\sim 15$  s, with one of the clusters always pointing in source direction (Bradt et al. 1993). The timing resolution of *HEXTE* is  $7.6 \mu\text{s}$  and the sensitivity to detect sources at  $100 \text{ keV}$  in  $10^5$  s is  $10^{-6} \text{ photons cm}^{-2} \text{ s}^{-1} \text{ keV}^{-1}$  (Rothschild et al. 1998).

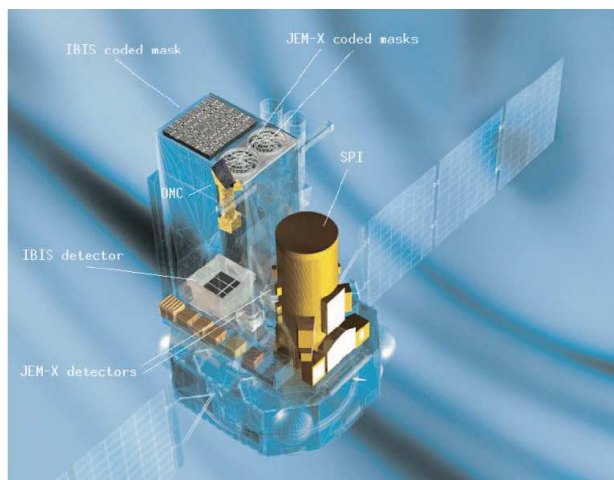


Figure 3.4: Drawing of the *INTEGRAL* satellite. Figure is taken from Winkler et al. (2003).

## 3.2 *INTEGRAL*

The International Gamma-Ray Astrophysics Laboratory *INTEGRAL* is a medium-size ESA mission designed for the observation of celestial gamma-ray sources (Winkler et al. 2003). *INTEGRAL* was launched from Baikonur/Kazakhstan in October 2002. It provides spectra (2.5 keV FWHM @ 1 MeV) and imaging (12 arcmin FWHM angular resolution) in gamma-rays, X-rays and visible light (Winkler et al. 2003). In Figure 3.4, a drawing of the *INTEGRAL* satellite is shown. The observatory carries two gamma-ray instruments, the spectrometer *SPI* (20 keV–8 MeV) (Vedrenne et al. 2003) and the imager *IBIS* (15 keV–10 MeV) (Ubertini et al. 2003), the X-ray monitor *JEM-X* (3–35 keV) (Lund et al. 2003), and an optical monitor, *OMC* (550 nm) (Mas-Hesse et al. 2003). The *INTEGRAL* observatory permits the observation of sources in X-ray, gamma-ray and optical light simultaneously due to the co-aligned position of its instruments.

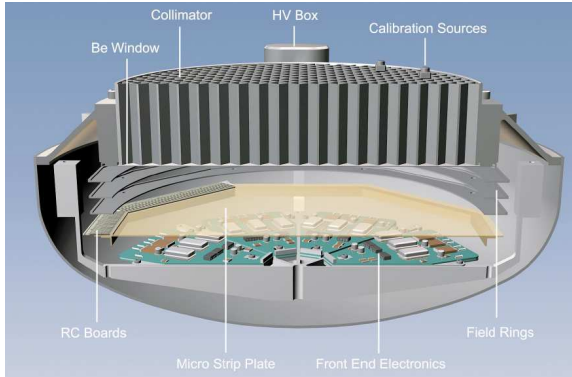


Figure 3.5: The *JEM-X* imager. Figure is taken from Lund et al. (2003).

Table 3.1: Key parameters of *JEM-X*. Values from Lund et al. (2003) and Winkler et al. (2003).

Energy range	3–35 keV
Spectral resolution (FWHM)	2.0 keV @ 22 keV
Angular resolution (FWHM)	3.35'
Field of view	4.8° fully coded
Point source location	15" (for a $10\sigma$ source)
Time resolution	122 $\mu$ s
Continuum sensitivity $3\sigma$ , $10^6$ s	$1.2 \times 10^{-5}$ @ 6 keV
(photons $\text{cm}^{-2} \text{s}^{-1} \text{keV}^{-1}$ )	$1.3 \times 10^{-5}$ @ 30 keV

### 3.2.1 *JEM-X*

*JEM-X* (Lund et al. 2003) is the low energetic X-ray monitor on board of the *INTEGRAL* observatory (Fig. 3.5). It generates spectra and imaging from 3–35 keV with arcminute angular resolution (Lund et al. 2003). *JEM-X* consists of two identical gas chambers with coded aperture masks that are rotated by  $180^\circ$  with respect to each other (Lund et al. 2003). The sensitive area of each gas chamber is  $500 \text{ cm}^2$  (Lund et al. 2003). Table 3.1 lists the instrumental values of *JEM-X*.

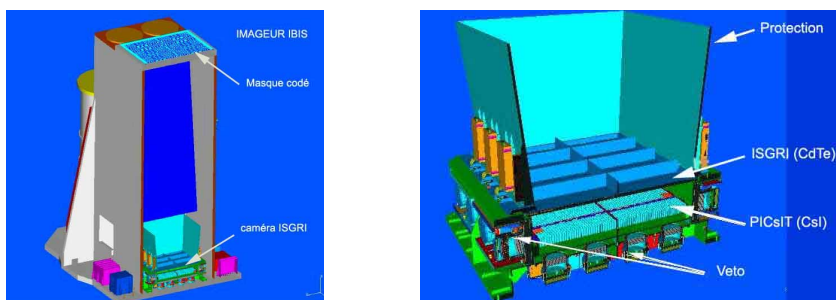


Figure 3.6: The *IBIS* imager. Figure is taken from *irfu.cea.fr*.

Table 3.2: Key parameters of the *IBIS* imager. Values from Ubertini et al. (2003) and Winkler et al. (2003).

Energy range	15 keV–10 MeV
Spectral resolution (FWHM)	8.0 keV @ 100 keV
Angular resolution (FWHM)	12'
Field of view	9° × 9° fully coded
Point source location	30"
Time resolution	61 μs for E < 1 MeV
Continuum sensitivity 3σ, 10 <sup>6</sup> s (photons cm <sup>-2</sup> s <sup>-1</sup> keV <sup>-1</sup> )	3.8 × 10 <sup>-7</sup> @ 100 keV 5.0 × 10 <sup>-7</sup> @ 1 MeV

### 3.2.2 *IBIS*

The *IBIS* imager (Ubertini et al. 2003) consists of two camera layers, the low energy detector *ISGRI* (Lebrun et al. 2003) and the high energy camera *PICsIT* (Labanti et al. 2003) (Fig. 3.6). The instrument has a coded mask and produces images with an angular resolution of 12 arcmin. The soft gamma-ray camera *ISGRI* is sensitive from 15 keV–1 MeV (Ubertini et al. 2003). It consists of 128×128 CdTe detector crystals that make up a sensitive area of 2621 cm<sup>2</sup> (Lebrun et al. 2003). The high energy detector *PICsIT* operates from 175 keV–20.4 MeV (Labanti et al. 2003). 64×64 CsI scintillators which are read out by photodiodes

Table 3.3: Key parameters of the *SPI* spectrometer. Values from Vedrenne et al. (2003) and Winkler et al. (2003).

Energy range	20 keV–8 MeV
Spectral resolution (FWHM)	2.5 keV @ 1.3 MeV
Angular resolution (FWHM)	2.5°
Field of view	16° fully coded
Point source location	$\leq 1.3^\circ$
Time resolution	52 $\mu$ s
Continuum sensitivity $3\sigma$ , $10^6$ s	$5.5 \times 10^{-6}$ @ 100 keV
(photons $\text{cm}^{-2} \text{s}^{-1} \text{keV}^{-1}$ )	$1.2 \times 10^{-6}$ @ 1 MeV

compose the detector plane that is divided into 8 subpanels (Labanti et al. 2003). The instrumental key parameters are shown in Table 3.2.

### 3.2.3 *SPI*

The spectrometer *SPI* provides high-resolution spectra from 20 keV–8 MeV (Vedrenne et al. 2003). It consists of 19 germanium detectors with an anticoincidence shield and a coded aperture mask (Vedrenne et al. 2003). *SPI* produces spectra with an energy resolution of 2.5 keV @ 1.3 MeV and has an angular resolution of 2.5° (Vedrenne et al. 2003). Table 3.3 lists the instrumental characteristics of the spectrometer.

### 3.2.4 *OMC*

*OMC* is the Optical Monitoring Camera aboard of *INTEGRAL* (Mas-Hesse et al. 2003). The camera is designed to observe the target source simultaneously with the gamma-ray and X-ray detectors. This is essential for a better understanding of the underlying physics of the production of hard X-ray and gamma-ray photons. The *OMC* consists of a CCD detector with a field of view of  $5^\circ \times 5^\circ$  (Mas-Hesse et al. 2003). The point source location accuracy is about 6 arcsec and the time resolution around 3 s (Mas-Hesse et al. 2003).



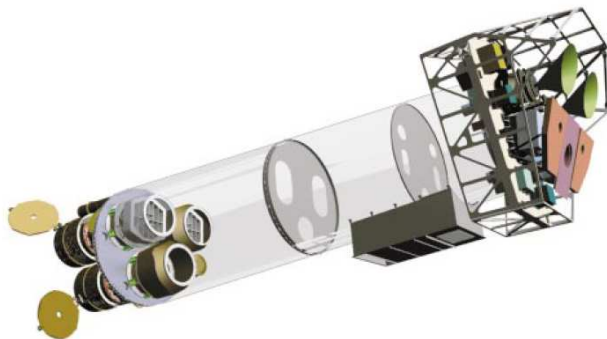


Figure 3.7: A schematic view of the *XMM-Newton* observatory. The X-ray mirror assemblies, *XMM-OM* and *RGS* are located behind the entrance windows on the left. A long carbon fibre tube connects the mirror platform with the focal plane where the *RGS* cameras and the *EPIC PN* and *EPIC MOS* detectors are located (on the right). Figure is taken from Jansen et al. (2001).

### 3.3 *XMM-Newton*

The ESA mission *XMM-Newton* (X-ray Multi Mirror) was launched in December 1999 (Jansen et al. 2001). The *XMM-Newton* observatory carries 4 instruments: an Optical and UV Monitor telescope *XMM-OM* (Mason et al. 2001), the Reflection Grating Spectrometer *RGS* (den Herder et al. 2001) and the *EPIC* (European Photon Imaging Camera) instrument with the *MOS* (Turner et al. 2001) and *pn* (Strüder et al. 2001) cameras. The observatory is put in a highly eccentric orbit with a period of  $\sim 48$  hours. A basic objective of *XMM-Newton* is the spectral analysis of faint sources. In Figure 3.7, an overview of the instrument is shown.

#### 3.3.1 *XMM-OM*

The *XMM-Newton* Optical and UV Monitor telescope (*XMM-OM*) operates at wavelengths from 170 nm to 650 nm (Mason et al. 2001). The

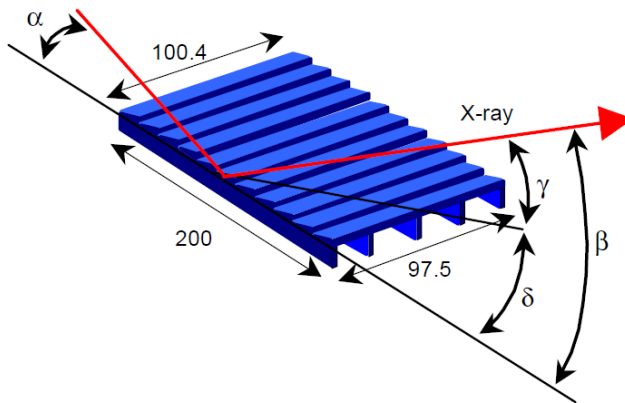


Figure 3.8: Layout of one of the 182 *RGS* gratings. Figure is taken from den Herder et al. (2001).

instrument owns a microchannelplate-intensified CCD detector and has a full FOV of  $17 \times 17$  arcmin (Mason et al. 2001).

### 3.3.2 *RGS*

The two identical Reflection Grating Spectrometer (*RGS*) operate in the soft X-ray energy range from 0.3–2.1 keV ( $38\text{--}6\text{ \AA}$ ) (den Herder et al. 2001). The spectral resolution is  $\Lambda/\Delta\Lambda(\text{FWHM}) = 100 - 500$  for line separation and the wavelength accuracy is about  $8\text{ m\AA}$ . The peak effective area of the instrument is  $140\text{ cm}^2$  at  $15\text{ \AA}$  (den Herder et al. 2001). Each *RGS* consists of 182 aligned reflection gratings (Fig. 3.8).

### 3.3.3 *EPIC*

The *EPIC* detector consists of 3 X-ray mirror modules (Turner et al. 2001). Each module is made of 58 nested Wolter 1 X-ray mirror shells with a focal length of 7.5 m and an effective area of  $1500\text{ cm}^2$  (Turner et al. 2001). In the focal plane of each telescope is an X-ray CCD camera: two

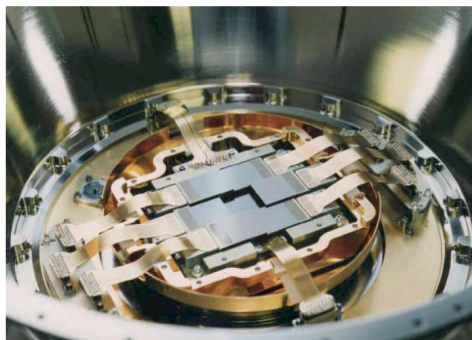


Figure 3.9: The 7 front-illuminated CCDs of the *MOS* camera. Figure is taken from Turner et al. (2001).

*MOS* CCD cameras and one *pn* CCD camera (Turner et al. 2001). The *MOS* cameras consist of 7 CCDs, the *pn* camera - of 12. A picture of the *MOS* CCD camera is shown in Figure 3.9.

The *MOS*- and *pn*-CCD cameras can be run in different operating modes (Strüder et al. 2001, Turner et al. 2001) (see Fig. 3.10 for the *pn* operating modes):

- full frame and extended full frame mode: all pixels of all CCDs of the *pn* camera are read out
- partial window mode (large and small window mode): the central CCD of the *MOS* camera can be operated in small window ( $100 \times 100$  pixels) and large window ( $300 \times 300$  pixels) mode; the large window mode of the *pn* camera uses only half of the CCDs while during the small window mode only a part of CCD 0 is read out
- timing mode: when the *MOS* and *pn* cameras are used in timing mode the imaging is only done in one dimension along the column axis; for the *pn* camera there is an additional burst mode with a very high time resolution

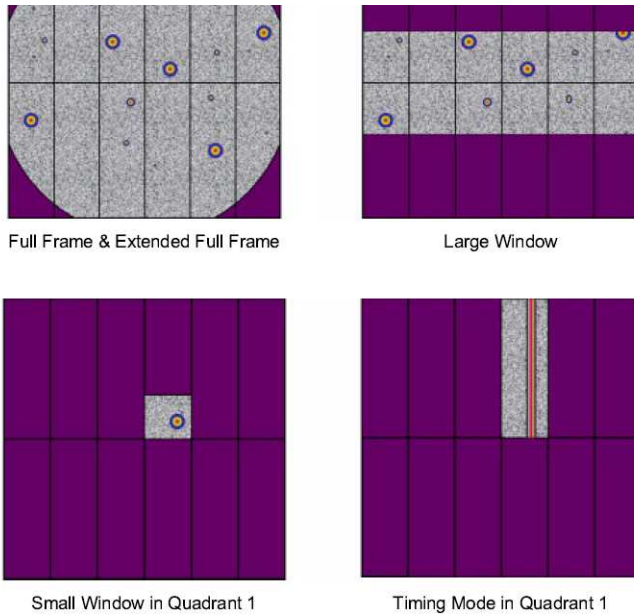


Figure 3.10: Illustration of the different operating modes of the *pn* CCD camera. Figure is taken from Strüder et al. (2001).

# Chapter 4

## Be/X-ray binary system A 0535+26

### 4.1 Overview

#### 4.1.1 History

The Be/X-ray binary system A 0535+26<sup>1</sup> was discovered in April 1975 by the satellite *Ariel V* during a giant outburst (Rosenberg et al. 1975). The system consists of a pulsating neutron star and the optical companion O9.7IIIe star HDE 245770 (Li et al. 1979, Giangrande et al. 1980). A 0535+26 regularly undergoes *normal* and *giant* outbursts but also phases of quiescence (Motch et al. 1991). According to the classification by Stella et al. (1986), normal outbursts can repeat periodically at times close to periastron passage. The outbursts last several days and can reach fluxes of about  $\sim 10^{36} - 10^{37} \text{ erg s}^{-1}$ . The increase of the accretion rate probably arises from a closer position of the neutron star to its Be star companion (Stella et al. 1986). Thereby, the neutron star can accrete matter from the circumstellar disk of the companion. Giant outbursts have a duration of several tens of days during which the luminosity increases to  $\gtrsim 10^{38} \text{ erg s}^{-1}$ . The onset of these outbursts is not correlated

---

<sup>1</sup>A 0535+26 is referred to as 1A 0535+262 in the SIMBAD Astronomical Database

Table 4.1: Reported giant outbursts of A 0535+26.

year	flux (Crab)	satellite	reference
1975 Apr	$\sim 2$ (3–7 keV)	Ariel V	Rosenberg et al. (1975)
1977 Dec	$\sim 1.5$ (28–40 keV)	Signe II	Violes et al. (1982)
1980 Oct	$\sim 1.5$ (1–22 keV)	Hakucho	Nagase et al. (1982)
1983 Jun	$\sim 2$ (32–91 keV)	SMM	Sembay et al. (1990)
1989 Apr	$\sim 4.3$ (16–26 keV)	Mir-Kvant	Makino et al. (1989)
1994 Feb	$\sim 6.2$ (20–40 keV)	CGRO-BATSE	Finger et al. (1994b)
2005 May	$> 3$ (15–195 keV)	Swift-BAT	Tueller et al. (2005)
2009 Dec	$\sim 3.7$ (15–80 keV)	Swift-BAT	Caballero et al. (2009)
2011 Feb	$\sim 3.6$ (5–200 keV)	INTEGRAL	Caballero et al. (2011b)

to an orbital phase of the system (Stella et al. 1986). Often there is no clear distinction between the two kinds of outbursts. Thus, some outbursts in A 0535+26 cannot be clearly assigned to one of those two groups.

A 0535+26 has experienced several giant outbursts since its discovery in 1975. Besides the 1975 giant outburst, the system went through giant outbursts in 1977 (Chartres & Li 1977, Violes et al. 1982), 1980 (Nagase et al. 1982), 1983 (Sembay et al. 1990), 1989 (Makino et al. 1989), 1994 (Finger et al. 1994a,b, 1996), 2005 (Tueller et al. 2005), 2009 (Caballero et al. 2009, 2011c, Krimm et al. 2009, Wilson-Hodge et al. 2009) and 2011 (Caballero et al. 2011b, Camero-Arranz et al. 2011, Tchernin et al. 2011). A list of the giant outbursts along with the reported fluxes is given in Table 4.1. The specified outbursts are marked in Figure 4.1, a plot taken from Camero-Arranz et al. (2012). In the three indicated panels, Camero-Arranz et al. (2012) show a normalized long time light curve accumulated with several instruments (*top panel*), the respective H $\alpha$  equivalent widths (*middle panel*) and visual magnitudes (*bottom panel*).

## 4.1.2 Properties of the system

The distance of the system was first determined to be  $\sim 1.3$  kpc (Hutchings et al. 1978) while newer measurements report a value of about 2 kpc (Steele et al. 1998). Nagase et al. (1982) found that the

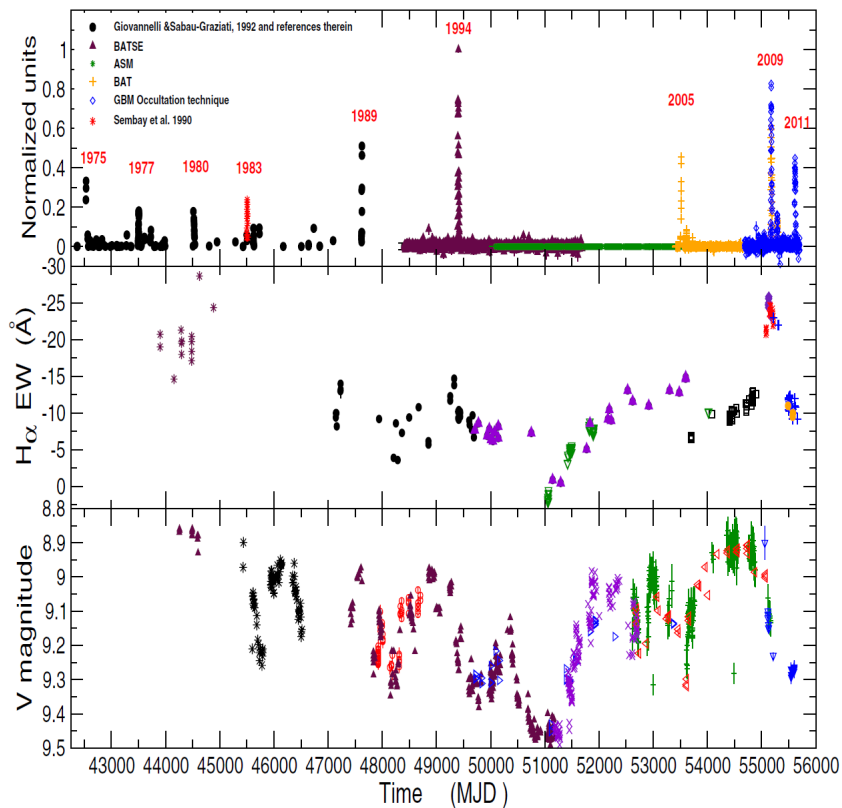


Figure 4.1: Long time light curve of A 0535+26 of different instruments (marked by different symbols and colors). In the *top panel*, the history of outbursts is plotted in normalized units (not corrected for the energy range of the respective instruments); the years of the giant outbursts are given. The *middle* and *bottom panels* show the  $H\alpha$  equivalent width and the visual magnitude. Figure is taken from Camero-Arranz et al. (2012).

recurrence time of outbursts is about 110 days, likely related to the orbital period. During a long-time survey of Vela 5B from 1969–1979, an orbital period of  $111.0 \pm 0.4$  days was confirmed (Priedhorsky & Terrell 1983). Finger et al. (2006) report the latest orbital ephemeris: the orbital period  $P_{\text{orb}} = 111.1 \pm 0.3$  d, the time of periastron passage  $\tau_{\text{periastron}} = \text{MJD } 53613.0 \pm 1.3$ , the projected semi-major axis  $a \sin i = 267 \pm 13$  lt-sec with the inclination  $i$ , the argument of periastron  $\omega = 130 \pm 5^\circ$  and the eccentricity  $e = 0.47 \pm 0.02$ . A review of the system is e.g. Giovannelli & Graziati (1992).

## 4.2 A 0535+26 in quiescence

The light curve of A 0535+26 shows episodes of quiescence (e.g. Fig. 4.1). By measurements of the  $\text{H}\alpha$  and  $\text{He I}$  line widths and of the visual magnitude of the star, it is possible to estimate the circumstellar disk size (Camero-Arranz et al. 2012). The size of the equatorial disk (that provides the material for accretion in normal outbursts) of the companion star HDE 245770 varies with time (Camero-Arranz et al. 2012). A particularly long period of quiescence occurred after the 1998 normal outburst, when the source remained quiet until 2005. During quiescence episodes, the source is supposed to be in the centrifugally inhibited "propeller" regime (Illarionov & Sunyaev 1975). In some cases however, pulsations can still be observed (e.g. Rothschild et al. 2013, Doroshenko et al. 2014), suggesting that accretion still takes place. Since this behavior is only seen in some observations, accretion might still occur but is not always funneled along the magnetic field lines onto the magnetic poles (Rothschild et al. 2013). Rothschild et al. (2013) analyzed *RXTE* and other observations past a giant outburst. They find that the flux level is reduced to  $\sim 2 \times 10^{-11} \text{ erg s}^{-1} \text{ cm}^{-2}$  6–12 months after the outburst. The absorption column density  $N_{\text{H}}$  by neutral material on the line of sight also decreases with time after the outburst but does not show any dependence on the orbital phase. The power law index does not change with flux, but is found to indicate a steeper spectrum in quiescence compared to that during outbursts. Rothschild et al. (2013) suggest a different mode of accretion during the quiescence episodes. For some observations, Rothschild et al. (2013) found small flares indicating ongoing and variable



accretion onto the neutron star during quiescence. Doroshenko et al. (2014) analyzed *XMM* observations during quiescence. They found that many properties of the system, e.g. the power spectrum, are similar to those during outbursts (see also Motch et al. 1991, Ikhsanov 2001). This suggests that the observed emission during quiescence is powered by disk accretion and that the accretion geometry is similar to the one during outbursts.

## 4.3 Timing properties

### 4.3.1 Pulse period evolution

The first measurement of the system's pulse period was done during the 1975 giant outburst when Rosenberg et al. (1975) measured a pulse period of  $P \sim 104$  s. Subsequent analyses refined this value to 103.84 s (Li et al. 1979), 103.61 s (Nagase et al. 1982) or  $103.4 \pm 0.3$  s in the 1989 giant outburst (Makino et al. 1989). During the 1983 outburst, Sembay et al. (1990) reported a spin-up rate of  $-6 \times 10^{-8} \text{ s s}^{-1}$ . At the peak of the 1994 outburst, a period change of  $\dot{P} = -1.2 \times 10^{-11} \text{ s s}^{-1}$  was measured by Finger et al. (1996). Caballero et al. (2008) report a pulse period of 103.396 s and  $\dot{P} = (-1.69 \pm 0.04) \times 10^{-8} \text{ s s}^{-1}$  during the August/September 2005 outburst. Figure 4.2 shows the pulse period evolution of A 0535+26. The observed spin-up values show that the pulse period of the source decreases during episodes of higher mass accretion, i.e. during outbursts. In quiescence, a spin-down of  $\dot{\nu} = -7 \times 10^{-14} \text{ Hz s}^{-1}$  was measured (Doroshenko et al. 2014). The model for disk accretion by Ghosh & Lamb (1979b) can describe the evolution of the spin period during outbursts and in between (Doroshenko et al. 2014).

### 4.3.2 Power spectrum

The power spectrum of A 0535+26 shows quasi-periodic oscillations (QPOs). The QPOs are thought to be associated with the inner region of the accretion disk. During the 1994 giant outburst, Finger et al. (1996) observed QPOs with a frequency that changed from 27 mHz to 72 mHz and then returned to 25 mHz. This frequency variation was also reflected in the evolution of the flux and the spin-up rate during the outburst,



### 4.3.3 Pulse profiles

The X-ray pulse profiles of A 0535+26 have a double-peaked structure with an asymmetric main and a more symmetric secondary peak (Frontera et al. 1985, Kendziorra et al. 1994). The high energy (above  $\sim 20$  keV) pulse profiles show less complex pulse shapes, the main minimum (at phase 0.0) gets deeper with increasing energy (Ricker et al. 1976). At lower energies (below  $\sim 8$ – $10$  keV), several irregularly spaced maxima are observed for both pulses (Bradt et al. 1976). Naik et al. (2008) report a diplike structure around phase 0.65–0.8 in the low energy (most prominent  $< 1$  keV) pulse profiles. Caballero et al. (2008) found differing pulse profiles during the pre-outburst flare of the August/September 2005 outburst (Fig. 4.3). During quiescence, the shape of the pulse profile is simplified but shows similar features as the ones during outbursts (Doroshenko et al. 2014) .

### Pulse-to-pulse variability

The light curve of A 0535+25 exhibits high pulse-to-pulse variability (Frontera et al. 1985, Kendziorra et al. 1994). This behavior is known for many X-ray binary systems including accreting neutron stars. The pulse shape and intensity vary from one pulse to the other (e.g. Fig. 4.4). Sometimes the main peak splits into narrower peaks. This variability is unrelated to the pulse phase and likely results from processes related to the variability of the local accretion flow (Frontera et al. 1985). For low energies, the variation of the pulse profile can be explained by absorption, while for higher energies, the pulse profile variation might be induced by a highly non-stationary accretion flow. Inhomogeneity of the accretion flow is generally expected (e.g. by accretion from a non-stationary stellar wind, see e.g. Morfill et al. 1984, Demmel et al. 1990) but can also be caused by instabilities at the magnetospheric boundary. This can lead to variations of the emitting structure and thereby to pulse profile variations on time scales of the pulsar's period or shorter (Klochkov et al. 2011). Variations of the pulse shape averaged over longer time scales (several 100/1000 s) can be correlated with changes in the luminosity of the source and with the related changes in the intrinsic beam pattern (Frontera et al. 1985).

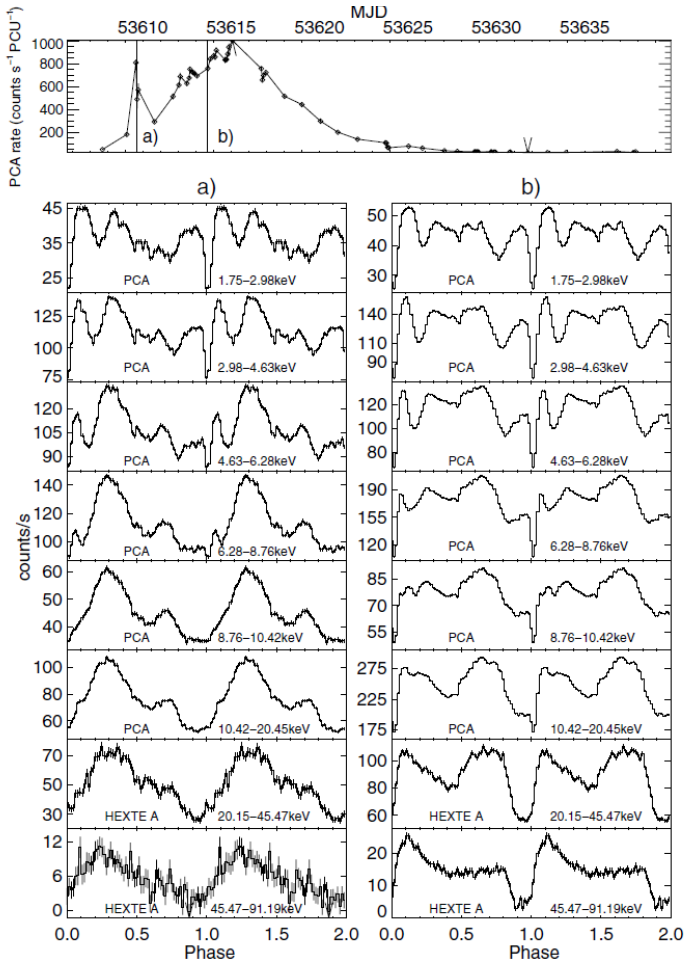


Figure 4.3: The background-subtracted pulse profiles of the 2005 outburst of the pre-outburst flare (*first column*) and of the main outburst (*second column*). In the *upper panel*, a plot of the light curve of the respective outburst is shown. The times of the observations used for the pulse profile extraction are marked by vertical lines. Figure is taken from Caballero et al. (2008).

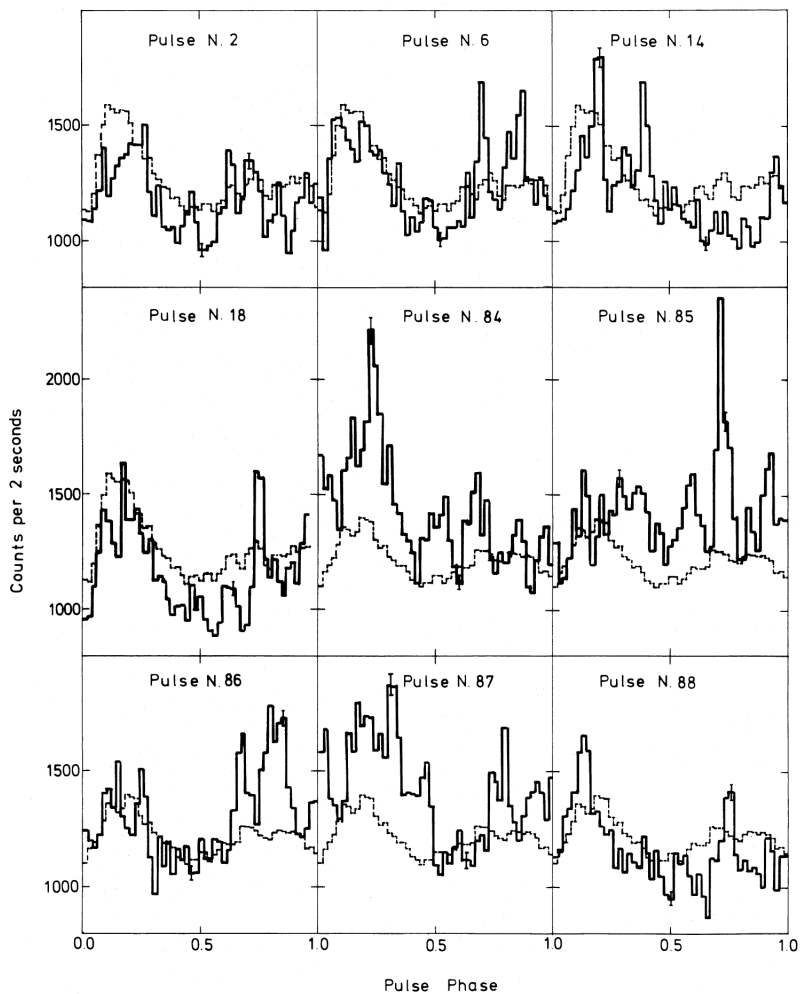


Figure 4.4: The panels show single pulses (*solid line*) of A 0535+26 of the 27–100 keV energy band taken during the 1980 giant outburst, together with the averaged light curve (*dashed line*). A high pulse-to-pulse variability is noticeable. Figure is taken from Frontera et al. (1985).

### Pulsed fraction

The pulsed fraction is determined as

$$\text{PF} = \frac{F_{\text{max}} - F_{\text{min}}}{F_{\text{max}} + F_{\text{min}}} \quad (4.1)$$

with the minimum  $F_{\text{min}}$  and maximum  $F_{\text{max}}$  flux in the pulse profile. The pulsed fraction increases with increasing energy (Frontera et al. 1985, Kendziorra et al. 1994). In the 20–100 keV band, an increase from  $\sim 0.3$ – $0.4$  to  $\sim 0.8$ – $0.9$  was reported by Kendziorra et al. (1994).

## 4.4 Spectral properties

The X-ray spectrum of A 0535+26 can be described by the following phenomenological model: a hard power law  $E^{-\Gamma}$  ( $\Gamma \sim 0.8$ – $1.1$ , Ricketts et al. 1975) modified by an exponential cutoff (Kendziorra et al. 1994) (Fig. 4.5). Maisack et al. (1996) observed a spectral softening with increasing source intensity during the 1994 giant outburst whereas Caballero (2009) found a hardening of the photon index during the 2005 normal outburst. The spectrum shows two absorption lines at about 50 keV and 100 keV interpreted as cyclotron resonant scattering features (CRSFs, see Sec. 2.3.1) (Kendziorra et al. 1994). The line energies correspond to a magnetic field strength of about  $4.3 \times 10^{12}$  G (Kendziorra et al. 1994). Newer measurements of the spectral parameters indicate a line energy of  $\sim 46.3 \pm 0.5$  keV during the August/September 2005 outburst and a significantly higher line energy of  $\sim 52.0^{+1.6}_{-1.4}$  keV at the pre-outburst flare that preceded this outburst (Caballero et al. 2008). The cyclotron line energy of A 0535+26 stays rather constant with changing source luminosity (Terada et al. 2006, Caballero et al. 2007) (Fig. 4.6).

The spectral parameters of A 0535+26 change with the pulse phase (e.g. Fig. 4.7). In the pulse phase resolved analysis, a harder spectrum of the main peak (pulse phase  $\sim 0.0$ – $0.4$  in Fig. 4.3) with respect to the secondary peak (pulse phase  $\sim 0.5$ – $0.9$  in Fig. 4.3) was reported (Kendziorra et al. 1994, Maisack et al. 1996, Borkus et al. 1998, Caballero 2009). The main peak shows a lower CRSF energy (Caballero 2009)

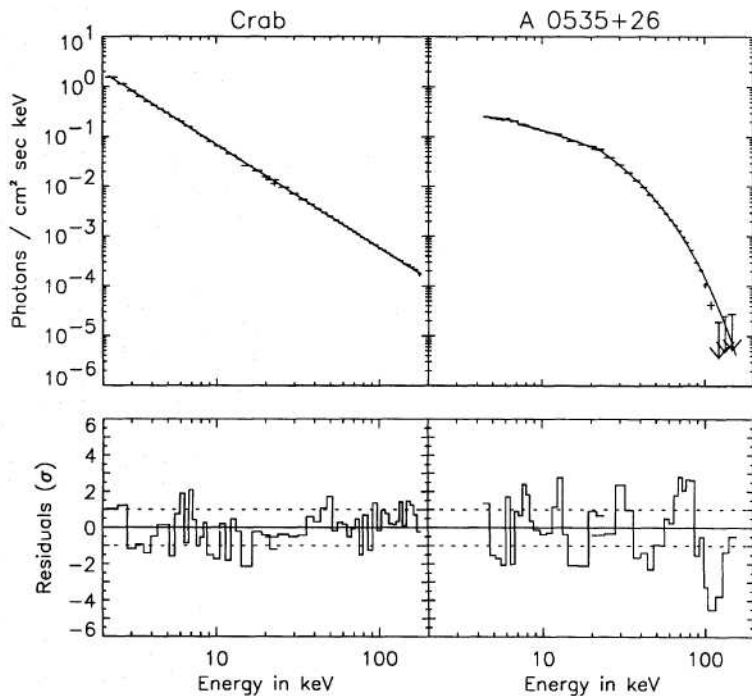


Figure 4.5: X-ray spectrum of A 0535+26 (*right* subplot). The spectrum is fitted with a power law with an exponential cutoff. The residuals indicate two absorption lines around 50 and 100 keV. Figure is taken from Kendziorra et al. (1994).

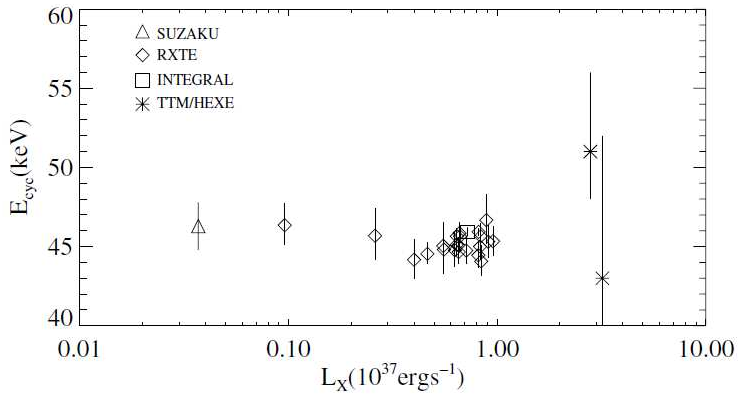


Figure 4.6: Evolution of the CRSF energy as a function of the source luminosity. Figure is taken from Caballero et al. (2007).

and a higher centroid energy and line depth of the first CRSF harmonic (Maisack et al. 1996, 1997).



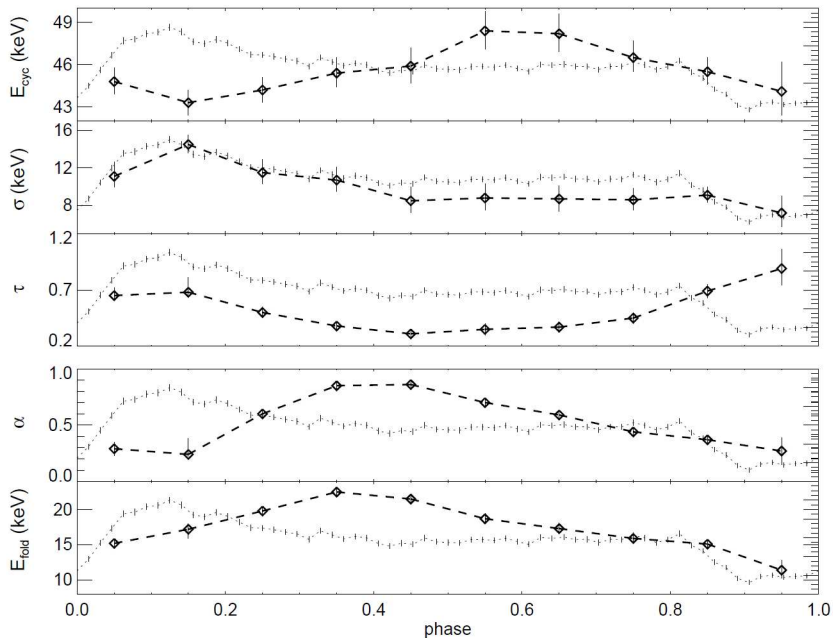


Figure 4.7: Pulse phase resolved spectral parameters of an *RXTE* observation of A 0535+26 together with the 44.5–80.6 keV pulse profile (*dotted line*). The CRSF line parameters  $E_{\text{cyc}}$ ,  $\sigma$  and  $\tau$  and the continuum parameters  $\alpha$  and  $E_{\text{fold}}$  (model `cutoffpl`,  $F(E) = \text{const} \cdot E^{-\alpha} \cdot e^{-E/E_{\text{fold}}}$ , see (5.1)) are shown as a function of the pulse phase. Figure is taken from Caballero (2009).



## Chapter 5

# *RXTE* and *INTEGRAL* observations of A 0535+26

### 5.1 The April 2010 outburst

The first brightening related to the 2010 outburst of A 0535+26 was detected by *Swift/BAT* on April 3rd 2010, (Caballero et al. 2010a). The source reached a flux of about 1.18 Crab in the 15–50 keV *Swift/BAT* light curve (Caballero et al. 2010a). For the same outburst, *INTEGRAL/ISGRI* measurements yielded a flux of about 0.92 Crab in the 20–100 keV energy band and detected a CRSF at about 47.6 keV (Caballero et al. 2010a). The April 2010 outburst followed the giant outburst of December 2009 that reached a flux of about 5.14 Crab in the 15–50 keV *Swift/BAT* light curve (Caballero et al. 2010a). The December 2009 giant outburst was not observed by most X-ray satellites due to sun constraints (Caballero et al. 2010c).

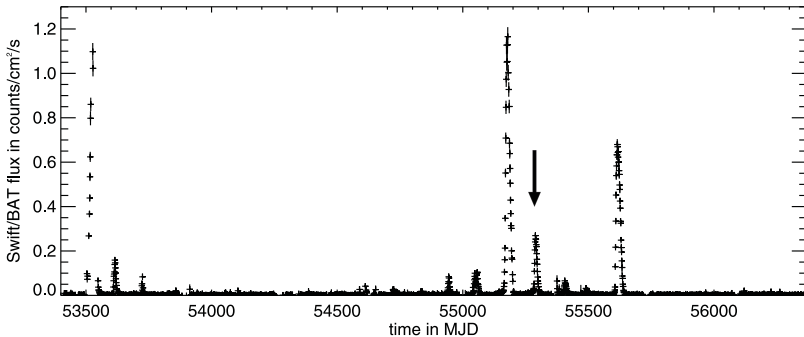


Figure 5.1: The daily light curve of *Swift/BAT* from February 2005 (MJD 53414) to March 2013 (MJD 56369). The bright peaks in the 15–50 keV *Swift/BAT* light curve correspond to the giant outbursts of 2005 May (MJD  $\sim$  53500), 2009 December (MJD  $\sim$  55180) and 2011 February (MJD  $\sim$  55600). We analyzed the outburst (marked with the arrow) that succeeded the giant outburst of December 2009 (at  $\sim$  MJD 55280–55310).

## 5.2 Observations

We analyzed 5 *INTEGRAL* and 3 *RXTE* observations (Fig. 5.2 and Table 5.1). All observations have FITS file data format<sup>1</sup>. The observations cover the maximum and the decline of the April 2010 outburst. The flux varied from a maximum value of about 1 Crab in the 10–100 keV light curve (*RXTE* observation 95347-02-01-01) to about 0.1 Crab at the end of the outburst (*INTEGRAL* observation 0917). The flux was calculated from the spectra with the `cflux` command in the X-ray spectral fitting program *XSPEC* (Arnaud 1996).

<sup>1</sup>[http://fits.gsfc.nasa.gov/fits\\_home.html](http://fits.gsfc.nasa.gov/fits_home.html)

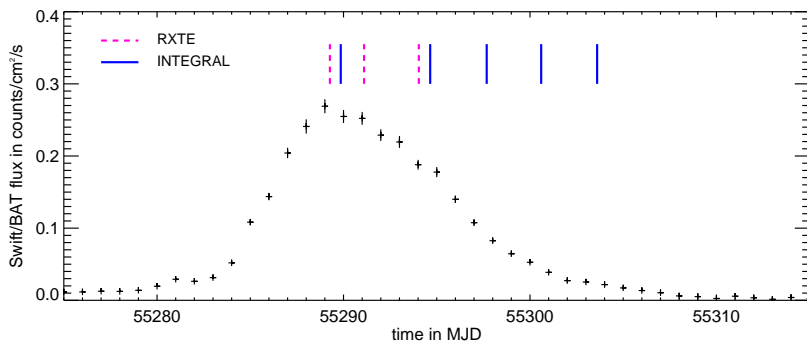


Figure 5.2: The daily light curve of *Swift*/*BAT* of the April 2010 outburst of A 0535+26. The *INTEGRAL* and *RXTE* observations that we used for our analysis are marked by solid blue (*INTEGRAL*) and dashed purple (*RXTE*) lines.

Table 5.1: *INTEGRAL* and *RXTE* observations of the April 2010 outburst.

observation	MJD	exposure [ks]	flux in Crab [10-100 keV]
<i>INTEGRAL</i>			
0912	55289	65.1	0.978
0914	55294	23.8	0.675
0915	55297	28.6	0.368
0916	55300	29.4	0.191
0917	55303	31.7	0.096
<i>RXTE</i>			
95347-02-01-00	55289	3.3	0.908
95347-02-01-01	55291	3.3	0.986
95347-02-01-02	55294	3.0	0.715

### 5.3 *RXTE* data reduction

For *RXTE* data processing, we used the HEASoft Version 6.11<sup>2</sup>. We extracted *PCA* and *HEXTE* data using the following filtering criteria: data from 0–10 minutes after passing the South Atlantic Anomaly (SAA) was discarded since the background increases dramatically. The *PCA* instrument suffers from contamination by electrons that originate from solar flare activity or which are trapped in the earth’s magnetosphere. We excluded data above a threshold value for the electron ratio of 0.15 and only used data with an elevation above 10° to prevent X-ray contamination from the earth. The *PCA* data were taken in *Generic Event mode*<sup>3</sup>, consisting of a time-series of unevenly spaced events. In this mode, each event is described by its arrival time, pulse height and PCU ID. We only had data from PCU 2 available. The data have a time bin size of 125 microseconds, 64 energy channels, and are read out every 1 s. The *HEXTE* data are in *Science Event* format<sup>4</sup>. Since *HEXTE Cluster A* stopped rocking in 2006 and *HEXTE Cluster B* in December 2009, we needed to add systematic errors to the *HEXTE* data. Since then, the two clusters are fixed on-source (*HEXTE Cluster A*) and off-source (*HEXTE Cluster B*). The measured background from *Cluster B* was converted to a background for *Cluster A* using the task `hextebackest` (Pottschmidt et al. 2006).

We added systematic errors of 1% to *PCA* and 1% to *HEXTE* data as recommended by the instrument teams. For the *RXTE* analysis, we used the `recorn` model in *XSPEC* to consider the uncertainties in the background normalization, similar to the analysis described in Rothschild et al. (2011).

### 5.4 *INTEGRAL* data reduction

The *INTEGRAL* data are grouped in *Science Window Groups* and *Observational Groups*. The data for one observation are split into pointings of  $\sim 30$  minutes that are separated by slews. A pointing

---

<sup>2</sup><http://heasarc.nasa.gov/docs/software/lheasoft/>

<sup>3</sup>[http://heasarc.gsfc.nasa.gov/docs/xte/abc/pca\\_configs-egen.html](http://heasarc.gsfc.nasa.gov/docs/xte/abc/pca_configs-egen.html)

<sup>4</sup>[http://heasarc.gsfc.nasa.gov/docs/xte/abc/data\\_files.html#event](http://heasarc.gsfc.nasa.gov/docs/xte/abc/data_files.html#event)

together with the adjacent slew is called a *Science Window* (ScW). The data of one ScW are combined in a *Science Windows Group*. In general, one observation consists of many ScWs. All data which belong to one observation compose an *Observational Group*. The *INTEGRAL* data were processed using the Off-line Scientific Analysis Software *OSA* 9.0<sup>5</sup>. We added a systematic error of 3% for *JEM-X* and 2% for *ISGRI*. The systematic errors were estimated by analyzing the Crab spectrum that was observed simultaneously with A 0535+26 in the field of view of *INTEGRAL*. The Crab spectrum was accumulated with the respective instruments and fitted with a canonical power law with a photon index of  $\sim 2.1$ .

Because of known problems in the energy calibration of *OSA* 9.0, we had to apply an additional gain correction. We fitted the Tungsten line complex of each observation by a Gaussian and compared the energy to its nominal value (Fig. 5.3). The energy values for each revolution<sup>6</sup> were fitted by polynomials (Fig. 5.4). The value used for the calibration is 58.8297 keV. This energy value was calculated as a weighted mean value of the two harmonics  $W K\alpha 1$  and  $W K\alpha 2$  at 59.3 keV and 57.98 keV (reference values from NIST<sup>7</sup>) using an intensity ratio of  $\text{intensity}(W K\alpha 2) / \text{intensity}(W K\alpha 1) = 0.57$  (Kasagi et al. 1986) since the two lines could not be resolved in our analysis (see also "Calibration" on *INTEGRAL* Science Data Center<sup>8</sup>). In our observations, we detected the line at  $\sim 60.2\text{--}60.25$  keV, thus with an offset of  $\sim 1.5$  keV to its nominal energy. We assume that a linear relation between measured and real photon energies is valid (as a first approximation) for energies up to  $\sim 100$  keV, i.e. the energy range used in our analysis. From the measured and theoretical values of the Tungsten line, we calculated the gain  $g$  ( $g = W_{\text{measured}}/W \approx 1.02\text{--}1.03$ ) and corrected the event files of all Science Windows.

In Figure 5.5, a 20–40 keV sky image of *IBIS/ISGRI* from our observation is shown. It is possible to identify the bright sources A 0535+26 and Crab in the field of view. The catalogue sources (*left image*) and the detected sources (*right image*) are marked in the intensity and significance mosaic

<sup>5</sup><http://isdc.unige.ch/integral/analysis#Software>

<sup>6</sup>referred to as rev. in the following

<sup>7</sup>NIST: National Institute of Standards and Technology

<sup>8</sup>[http://isdc.unige.ch/integral/download/osa/doc/10.0/isgri\\_energy\\_calib.pdf](http://isdc.unige.ch/integral/download/osa/doc/10.0/isgri_energy_calib.pdf)

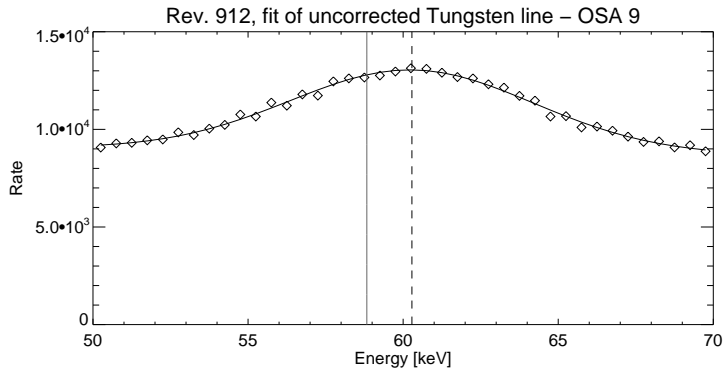


Figure 5.3: The count rate as a function of energy is shown for one Science Window (ScW 091200410010.001) of *INTEGRAL* observation 0912. The nominal value of the Tungsten line complex is 58.8297 keV (*solid line*) and the fitted value is  $\sim 60.15$  keV (*dashed line*) are indicated.

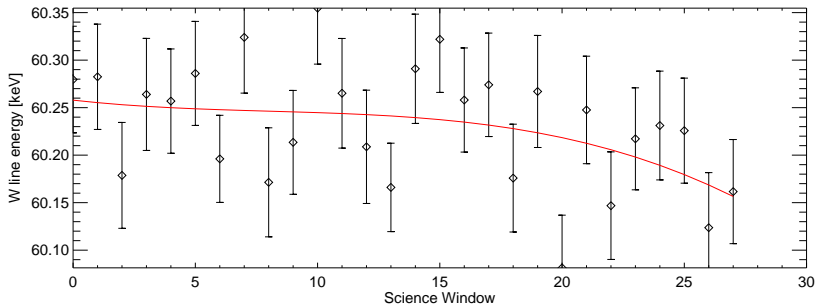


Figure 5.4: Tungsten line energy of each *INTEGRAL* science window of rev. 0912.



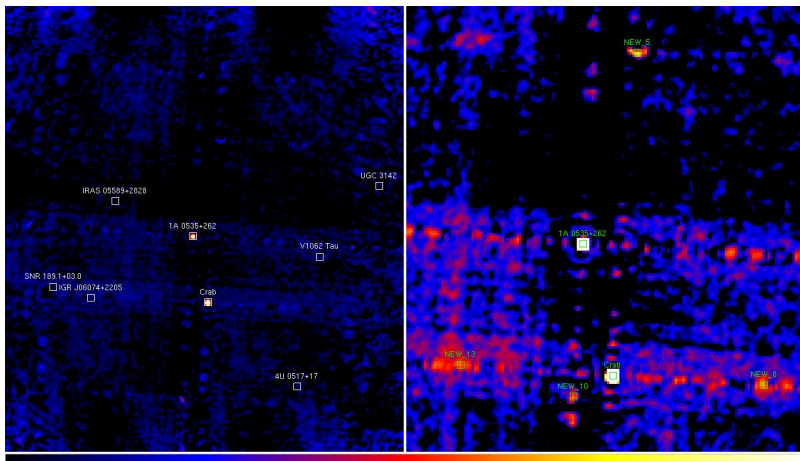


Figure 5.5: *IBIS/ISGRI* intensity (*left*) and significance (*right*) mosaic images of the 20–40 keV energy band. All catalogue sources are marked on the left, while on the right - only the detected ones.

images. Many of the detected sources are ghost sources resulting from the emission of the coded mask detector and needed to be excluded from the source catalogue used for the subsequent analysis. In our source catalogue, we excluded all faint and ghost sources and only included the bright source Crab beside our source of interest, A 0535+26. It is important to include Crab since the count rate of the spectrum and background of A 0535+26 is influenced by the strong emission of Crab.

## 5.5 Timing analysis

### 5.5.1 Light curve

*INTEGRAL/ISGRI* (20–120 keV) and *RXTE/PCA* (3–60 keV) light curves were extracted. We then subtracted the background and corrected the photon arrival times of the *INTEGRAL* and *RXTE* light curves for the motion of the satellite around the earth and the sun (barycentric correction) and for the binary motion of the pulsar around his companion

Table 5.2: Pulse period and  $T_0$  value (phase 0) of the *INTEGRAL* and *RXTE* observations.

observation	period [s]	$T_0$ [MJD]
<i>INTEGRAL</i> 0912	103.3357	55289.0007277752
<i>INTEGRAL</i> 0914	103.3247	55294.0011388439
<i>INTEGRAL</i> 0915	103.3245	55297.0003993061
<i>INTEGRAL</i> 0916	103.3222	55300.0007869947
<i>INTEGRAL</i> 0917	103.3220	55303.0011599808
<i>RXTE</i> 95347-02-01-00	103.3365	55289.0007253887
<i>RXTE</i> 95347-02-01-01	103.3181	55291.0004849015
<i>RXTE</i> 95347-02-01-02	103.3170	55294.0011269206

star (binary correction). For the binary correction, we used the ephemeris from Finger et al. (2006).

The pulse period was calculated using the epoch folding technique (`efsearch` in `FTOOLS`<sup>9</sup>). In this method the light curve is folded with a series of pulse periods in a selected pulse period range. For each trial period, the chi-square value of the folded light curve (pulse profile) is calculated. Possible coherent pulsations are indicated by peaks in the  $\chi^2$ -distribution over periods.

## 5.5.2 Pulse profiles

For the pulse profile analysis, we extracted *INTEGRAL* light curves of the *JEM X-2* energy bands 3.04–5.04 keV, 5.04–8.00 keV, 8.00–14.08 keV and 14.08–20.24 keV and of the *ISGRI* energy bands 20–25 keV, 25–35 keV, 35–60 keV and 60–80 keV. The light curves were extracted using the *OSA* tasks `ii.light` and `lc.pick` with a time resolution of 1 s. For the *RXTE* observations we used the *PCA* 3–5 keV, 5–8 keV, 8–14 keV, 14–20 keV, 20–25 keV, 25–35 keV and 35–60 keV energy bands. The light curves were extracted with a time resolution of  $2^{-7}$  s. We applied a bary- and binary correction (see above). Then, each light curve was folded with the pulse period found with `efsearch` (Table 5.2). The pulse profiles were produced with 64 phase bins (except for *INTEGRAL* observation

<sup>9</sup>[http://heasarc.gsfc.nasa.gov/ftools/ftools\\_menu.html](http://heasarc.gsfc.nasa.gov/ftools/ftools_menu.html)

0917 for which we used 32 bins). As a reference phase (phase 0) we selected the deep minimum in the pulse profile and fitted it with a Gaussian. For the *INTEGRAL* analysis, we used data of the energy bands 20–25 keV, 25–35 keV and 35–60 keV - for *RXTE* 14–20 keV, 20–25 keV and 25–35 keV.

In Figures 5.6, 5.7 and 5.8 we show the *RXTE* and *INTEGRAL* pulse profiles of different flux levels and energy bands.

The pulse profiles have a double-peaked structure that changes to single-peaked at lowest luminosities (e.g. *INTEGRAL* observation 0917). For energies from  $\sim 14$  keV to  $\sim 35$  keV, the pulse profiles show a symmetric double-peaked structure with a broad minimum at phase  $\sim 0.0$  and a smaller minimum at phase  $\sim 0.5$ , separating main and secondary peak. For energies above  $\sim 25$ – $35$  keV, the secondary peak gets lower. At low energies ( $\sim 3$ – $8$  keV), a notch in the main peak at phase  $\sim 0.25$  and a sharp minimum at phase  $\sim 0.1$  are noticed (see Fig. 5.7). We attribute this minimum to an excess of emission at phases  $\sim 0.85$ – $0.95$ .

### 5.5.3 Pulsed fraction

The pulsed fraction was calculated from the pulse profile data as given in Equation 4.1.

The flux maxima and minima were selected as the average values of the three highest/lowest successive count rates in the pulse profile data to reduce statistical uncertainties. We calculated the pulsed fraction in the same energy bands which we used for the pulse profile analysis. In Figure 5.9, we show the pulsed fraction from *INTEGRAL* revs. 0912, 0914, 0915 and 0916 and of the three *RXTE* observations as a function of energy. The results from *INTEGRAL* rev. 0917 are not shown due to insufficient statistics.

The pulsed fraction increases with decreasing source luminosity (Fig. 5.10). It also shows an increase with energy above  $\sim 15$  keV while at lower energies the pulsed fraction decreases with energy. We observe an offset between the pulsed fraction of *INTEGRAL* and *RXTE/PCA*, especially at higher energies.

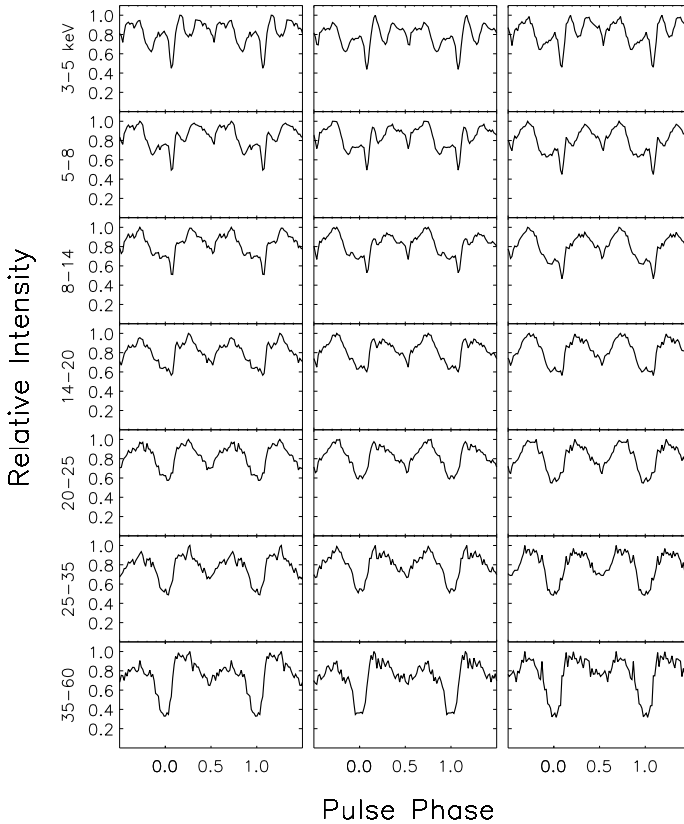


Figure 5.6: *RXTE/PCA* pulse profiles of A 0535+26. We show the normalized flux as a function of pulse phase for several energy bands (energy is increasing from *top* to *bottom*) and for different flux levels of the source (*left* - obs 95347-02-01-00 with  $F_{10-100\text{keV}} \sim 0.9\text{Crab}$ , *middle* - obs 95347-02-01-01 with  $F_{10-100\text{keV}} \sim 1.0\text{Crab}$ , *right* - obs 95347-02-01-02 with  $F_{10-100\text{keV}} \sim 0.7\text{Crab}$ ). All pulse profiles were produced with 64 phase bins.

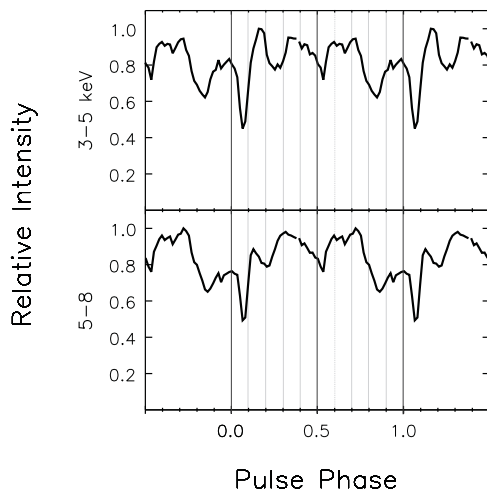


Figure 5.7: Zoom on the low energetic *RXTE/PCA* pulse profiles of A 0535+26. The normalized flux is shown as a function of pulse phase for energy bands 3–5 keV and 5–8 keV of obs 95347-02-01-00.

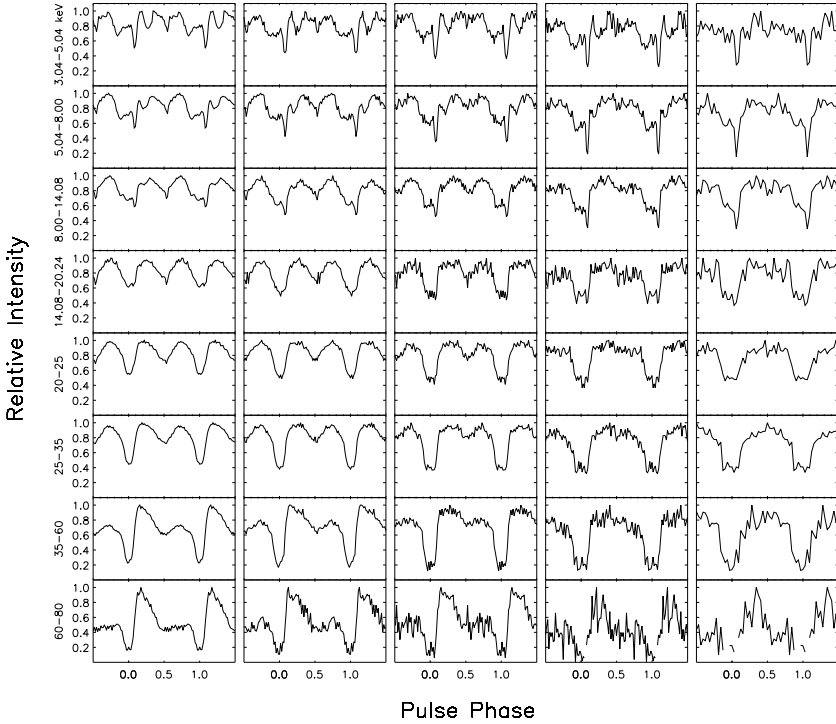


Figure 5.8: *INTEGRAL* pulse profiles of A 0535+26. The normalized flux is plotted as a function of pulse phase. Pulse profiles are shown for different flux levels (flux is decreasing from *left to right*: obs 0912 with  $F_{10-100\text{ keV}} \sim 1.0\text{ Crab}$  - obs 0917 with  $F_{10-100\text{ keV}} \sim 0.1\text{ Crab}$ ) and for different energy bands (energy is increasing from *top to bottom*). As a reference phase (phase 0) we selected the deep minimum in the pulse profiles of the 20–60 keV energy band. For *INTEGRAL* observations 0912, 0914, 0915 and 0916, we used 64 phase bins for observation 0917 – 32 bins. The pulse profiles in energy bands 3.04–5.04 keV, 5.04–8.00 keV, 8.00–14.08 keV and 14.08–20.24 keV are produced with *JEM X-2*, the 20–25 keV, 25–35 keV, 35–60 keV and 60–80 keV pulse profiles – with *ISGRI*.

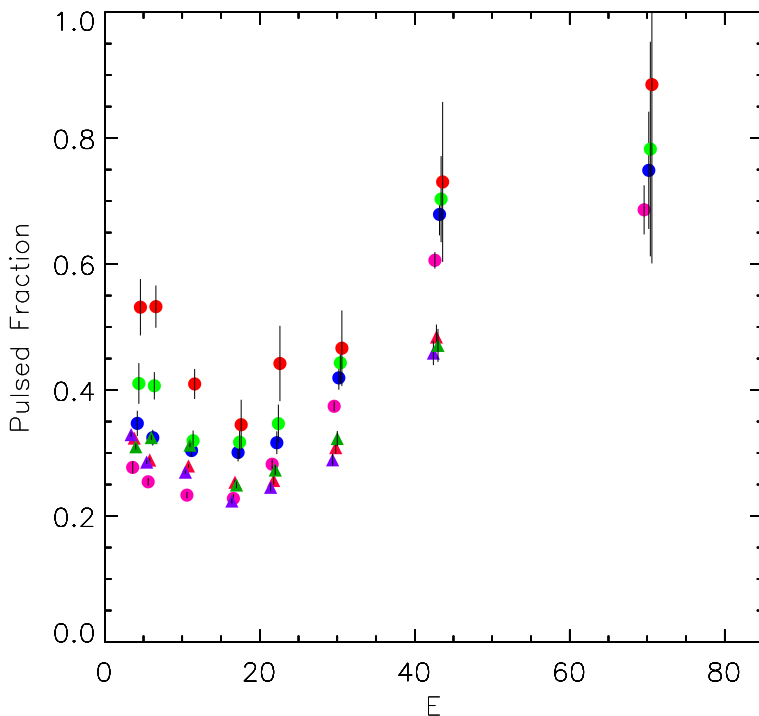


Figure 5.9: The pulsed fraction of A 0535+26 from the *INTEGRAL* and *RXTE/PCA* observations as a function of energy. The selected energy ranges of *INTEGRAL* are 3.04–5.04 keV, 5.04–8.00 keV, 8.00–14.08 keV and 14.08–20.24 keV (*JEM-X*) and 20–25 keV, 25–35 keV, 35–60 keV, 60–80 keV 80–120 keV (*ISGRI*). For *RXTE/PCA* we used the energy bands 3–5 keV, 5–8 keV, 8–14 keV, 14–20 keV, 20–25 keV, 25–35 keV and 35–60 keV. The *INTEGRAL* observations are marked with colored circles. Observation 0912 is marked in pink, observation 0914 in blue, observation 0915 in green and observation 0916 in red. The *RXTE* observations are marked with triangles - observation 95347-02-01-00 in red, 95347-02-01-01 in blue and 95347-02-01-02 in dark green. For a better illustration, the observations are plotted with a small horizontal offset with respect to each other.

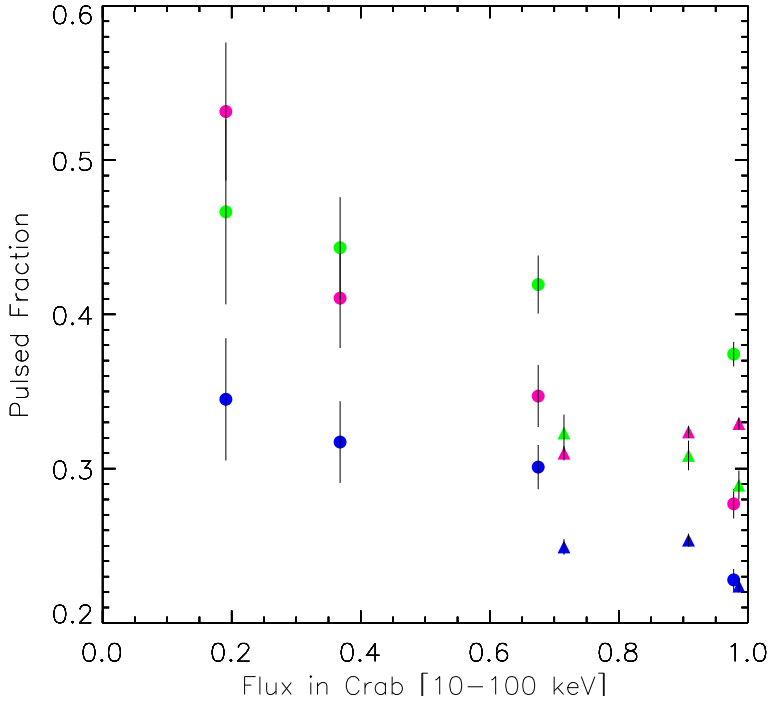


Figure 5.10: The pulsed fraction of A 0535+26 from the *INTEGRAL* and *RXTE/PCA* observations as a function of flux. We show the pulsed fraction in three selected energy bands: 3–5 keV (magenta), 14–20 keV (blue) and 25–35 keV (green). The *INTEGRAL* observations are marked with circles, the *RXTE* observations - with triangles.



### 5.5.4 Discussion

We analyzed 5 *INTEGRAL* and 3 *RXTE* observations of A 0535+26. The observed pulse profiles are consistent with the ones reported from other outbursts of the source (e.g. Kendziorra et al. 1994, Finger et al. 1996, Caballero et al. 2007, 2010b, 2013). The intensity of the secondary peak around the pulse phase 0.6–1.0 is strongly reduced at high energies and the profile gets single-peaked with decreasing luminosity. Tsygankov et al. (2007) report a similar behavior for 4U 0115+63 and interpret it with following simple geometrical model: During a rotational cycle, one magnetic pole of the neutron star is observed entirely while only the upper part of the column above the other pole is seen (see Fig. 5.11). The emission from this column forms the secondary peak. Hence, only the emission of softer photons is detected from this pole. The emission of harder photons that are produced closer to the neutron star surface (Basko & Sunyaev 1976b) can be screened by the neutron star (Tsygankov et al. 2007, Lutovinov & Tsygankov 2008). Thus, the intensity of the secondary peak decreases with increasing energy. The same applies for lower accretion rates: the column height decreases and the secondary peak of the pulse profile gets smaller.

The dependence of the pulsed fraction on energy and luminosity is common for X-ray pulsars (Ferrigno et al. 2007, Tsygankov et al. 2007, Barnstedt et al. 2008, Lutovinov & Tsygankov 2008). Tsygankov et al. (2007) describe this behavior for 4U 0115+63 with the model given above. The pulsed fraction increases with energy as the region where harder photons are emitted is located closer to the neutron star surface. With increasing energy, the emitting region gets more compact and therefore can be obscured during a higher fraction of the pulsation cycle. The model by Tsygankov et al. (2007) is only a toy model and does not include e.g. a distinct temperature distribution along the accretion column, the light bending or the shape of the beam function and its dependence on the object's luminosity and energy band. A more general explanation for the observed dependence of the pulse profiles and of the pulsed fraction on energy and luminosity can be the emission diagram changing from a more "pencil" to a more "fan" beam configuration with increasing flux.

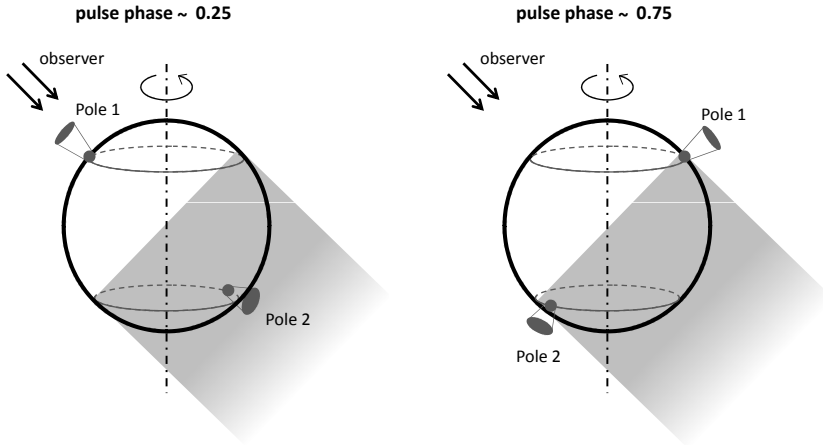


Figure 5.11: A layout of a possible geometry of A 0535+26 is shown for two pulse phases, pulse phase  $\sim 0.25$  (corresponding to the main peak in the pulse profile) and pulse phase  $\sim 0.75$  (corresponding to the secondary peak in the pulse profile). The pictures show the magnetic poles of the neutron star and its rotation axis. In grey, we indicate the region which is "shadowed" by the neutron star and therefore cannot be seen directly by the observer. In this picture, during the main peak, Pole 1 is seen from on top, while Pole 2 is shadowed by the neutron star. During the secondary peak, the upper part of the accretion columns of Pole 1 and Pole 2 are seen perpendicular to the emission axis. During one pulsation cycle Pole 1 is observed entirely, while only the upper part of the accretion column of Pole 2 is seen.

## 5.6 Spectral analysis

### 5.6.1 Pulse phase averaged spectrum

We analyzed the dependence of the spectral fit parameters on the source flux for the *RXTE* and *INTEGRAL* observations. The following analysis has been published in Müller et al. (2013a).

In the spectral analysis of the *RXTE* data, we used a range of 5–60 keV for *PCA* and 20–145 keV for *HEXTE*. We only used data above 5 keV due to an instrumental background feature at the xenon *L* edge at  $\sim 4.8$  keV. This feature is not sufficiently well modeled and could introduce systematic effects to our spectral fits (Rothschild et al. 2006, Caballero et al. 2008). For the spectral analysis of the *INTEGRAL* data, we used the energy bands 5–30 keV for *JEM-X* and 20–145 keV for *ISGRI*. We fitted the *RXTE* and *INTEGRAL* spectra of the various luminosity states of A 0535+26 with the X-ray spectral fitting program *XSPEC*. The continuum spectra were fitted with a power law with a photon index  $\Gamma$  modified by an exponential rolloff at the rolloff energy  $E_{\text{rolloff}}$ . This model is referred to as the `cutoffpl` model in *XSPEC*:

$$F(E) = \text{const} \cdot E^{-\Gamma} \cdot e^{-E/E_{\text{rolloff}}}. \quad (5.1)$$

To model the Fe  $K\alpha$  fluorescence line, we included a Gaussian emission line at  $\sim 6.4$  keV. The residuals of the fit require an absorption line at around 44 keV (Fig. 5.12 and 5.13). We interpret this feature as a cyclotron resonant scattering feature (CRSF) and fitted the line with a multiplicative absorption line with a Gaussian optical depth profile (model `gabs` in *XSPEC*) with a centroid energy of  $\sim 44.4$  keV:

$$F(E) = \exp \left[ -\frac{\tau_{\text{cyc}}}{\sqrt{2\pi}\sigma_{\text{cyc}}} \exp \left( -\frac{(E - E_{\text{cyc}})^2}{2\sigma_{\text{cyc}}^2} \right) \right], \quad (5.2)$$

here  $E_{\text{cyc}}$  is the cyclotron line centroid energy,  $\tau_{\text{cyc}}$  and  $\sigma_{\text{cyc}}$  characterize the line strength and width respectively. The residuals of the fit with the inclusion of the CRSF are shown in Figures 5.12 and 5.13 c). In the *RXTE* observations, the residuals indicate the presence of the first harmonic CRSF at  $\sim 104$  keV. However, for the further analysis we included only the fundamental CRSF in the *RXTE* spectra since the

first harmonic CRSF is not statistically significant (except for observation 95347-02-01-01). We also wanted to be consistent with the *INTEGRAL* spectral model.

In Table 5.3 and Figure 5.14, the fit parameters of the phase-averaged spectrum as a function of the source flux are shown. The photon index  $\Gamma$  is decreasing with increasing source flux implying a hardening of the power law part of the spectrum, while the rolloff energy  $E_{\text{rolloff}}$  is decreasing as a function of the flux, denoting a softening of the spectrum above the rolloff energy. To examine the evolution of the spectral hardness in a model-independent way, we calculated the hardness ratio of each observation. The ratio in the 5–20 keV and 20–50 keV energy band flux is negatively correlated with the source flux (bottom panel of Fig. 5.14), implying an overall hardening of the spectrum. To check a possible coupling between  $\Gamma$  and  $E_{\text{rolloff}}$ , we produced contour plots of the *INTEGRAL* observations (Fig. 5.15; Müller et al. 2013a). We do not detect a correlation between the cyclotron line energy and the source luminosity. The energy of the fundamental CRSF varies between  $\sim 43$ –46 keV.

Following the approach of Acciari et al. (2011), we also fitted the spectrum using a thermal model, the `compTT` model in *XSPEC*. We find that this model describes the spectrum well for energies up to  $\sim 35$  keV (the energy range used in Acciari et al. 2011) but does not provide an acceptable fit when applying it to the entire energy range used in our analysis. It yields high residuals especially at highest and lowest energies. Nevertheless, the evolution of the cyclotron line energy with source flux with this alternative spectral model is found to be consistent with our results from the fit with the `cutoffpl` model.

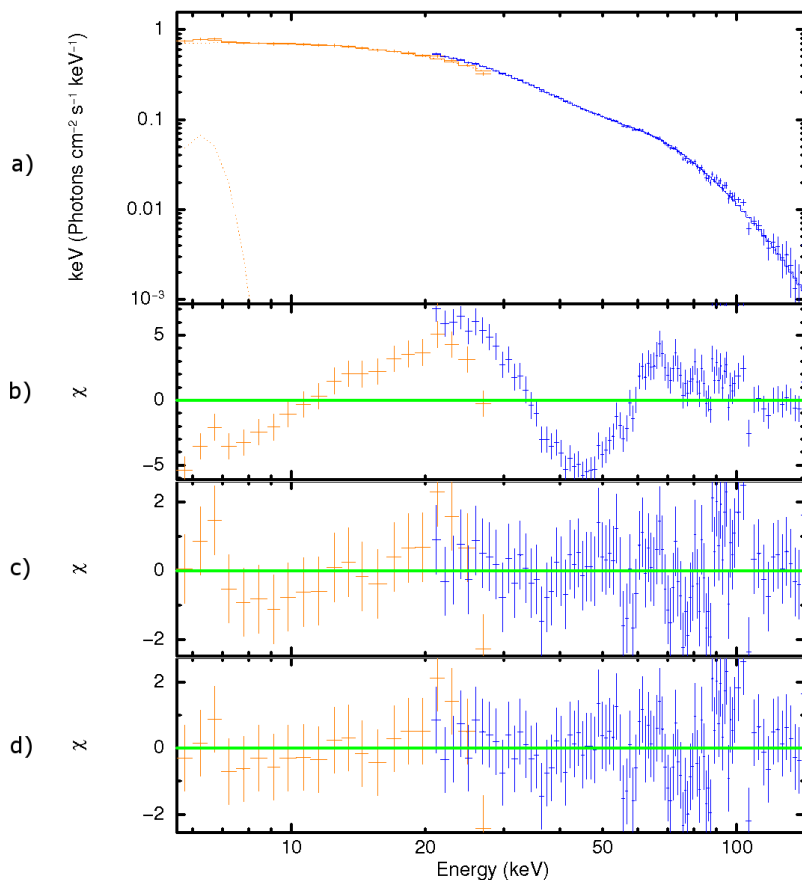


Figure 5.12: The *INTEGRAL* spectrum of A 0535+26 from rev. 0912: a) The unfolded spectrum of *JEM X-2* and *ISGRI* with the inclusion of a Gaussian emission line at  $\sim 6.4$  keV and the fundamental CRSF at  $\sim 44$  keV b) Residuals of a power law fit with exponential rolloff c) Residuals after the inclusion of a Gaussian absorption line to account for the CRSF  $\sim 44$  keV d) Residuals after the inclusion of an additional Gaussian emission line  $\sim 6.4$  keV to account for the fluorescence Fe K $\alpha$  line.

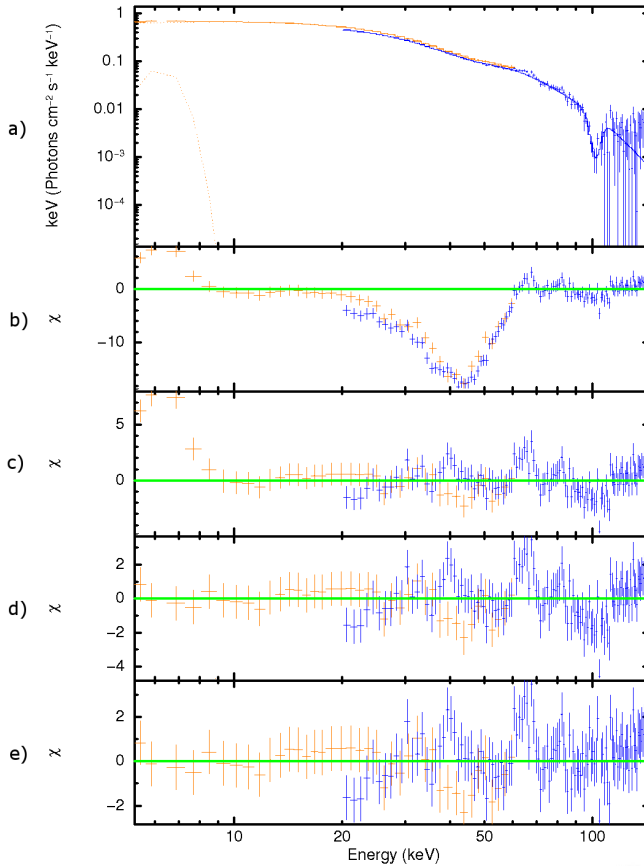


Figure 5.13: The *RXTE* spectrum of A 0535+26 from observation 95347-02-01-01: a) The unfolded spectrum for *PCA* and *HEXTE* with the inclusion of a Gaussian emission line at  $\sim 6.4$  keV, the fundamental CRSF at  $\sim 44$  keV and the first harmonic CRSF at  $\sim 104$  keV b) Residuals of a power law fit with exponential rolloff c) Residuals after the inclusion of a Gaussian absorption line to account for the CRSF at  $\sim 44$  keV d) Residuals after the inclusion of an additional Gaussian emission line at  $\sim 6.4$  keV to account for the fluorescence Fe  $K\alpha$  line e) Residuals after the inclusion of an additional Gaussian absorption line to account for the first harmonic CRSF at  $\sim 104$  keV.

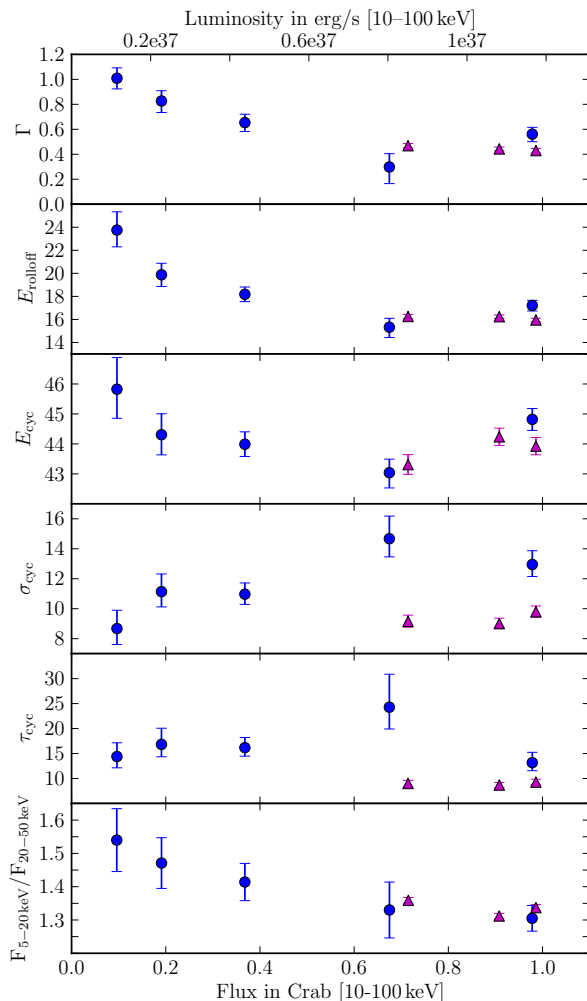


Figure 5.14: The spectral fit parameters as a function of the source flux/luminosity. The *INTEGRAL* observations are marked with blue circles, the *RXTE* observations - with purple triangles. We show the fit parameters of the photon index  $\Gamma$ , the rolloff energy  $E_{\text{rolloff}}$ , the cyclotron line energy  $E_{\text{cyc}}$ , the cyclotron line width  $\sigma_{\text{cyc}}$  and depth  $\tau_{\text{cyc}}$  and the hardness ratio calculated with the 5–20 keV and 20–50 keV energy bands.

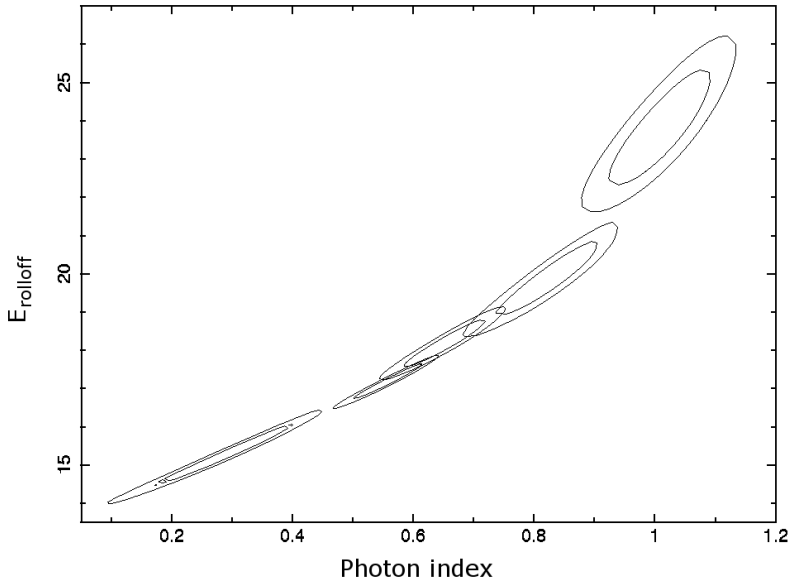


Figure 5.15: The confidence contour plot in the  $E_{\text{rolloff}}-\Gamma$  plane for all 5 *INTEGRAL* observations of A 0535+26. The indicated contour levels are at  $\chi_{\text{min}}^2 + 1.0$  (corresponds to 68% confidence for one chosen parameters) and  $\chi_{\text{min}}^2 + 2.3$  (corresponds to 68% confidence for two chosen parameters). Figure is taken from Müller et al. (2013a).



Table 5.3: The fit parameters of the phase averaged spectra of A0535+26 from the *INTEGRAL* observations 0912, 0914, 0915, 0916 and 0917 and the *RXTE* observations 95347-02-01-00, 95347-02-01-01 and 95347-02-01-02. The errors are at  $1\sigma$  confidence level.

\*For the fit of the first harmonic cyclotron line at  $E_{\text{cyc},2}$ , we fixed all other parameters.

observation	$\Gamma$	$E_{\text{rolloff}}$ [keV]	$E_{\text{cyc},1}$ [keV]	$E_{\text{cyc},2}$ * [keV]	$\sigma_{\text{cyc},1}$ [keV]	$\sigma_{\text{cyc},2}$ * [keV]	$\tau_{\text{cyc},1}$	$\tau_{\text{cyc},2}$ *	$\chi^2_{\text{red}}$ /d.o.f.
<i>INTEGRAL</i>									
0912	$0.56^{+0.06}_{-0.06}$	$17.21^{+0.44}_{-0.48}$	$44.82^{+0.36}_{-0.37}$		$12.95^{+0.92}_{-0.80}$		$13.16^{+2.08}_{-1.60}$		1.1/110
0914	$0.30^{+0.11}_{-0.13}$	$15.32^{+0.77}_{-0.90}$	$43.04^{+0.45}_{-0.51}$		$14.67^{+1.51}_{-1.21}$		$24.29^{+6.62}_{-4.37}$		0.9/110
0915	$0.65^{+0.07}_{-0.07}$	$18.18^{+0.64}_{-0.64}$	$43.99^{+0.41}_{-0.41}$		$10.97^{+0.75}_{-0.68}$		$16.18^{+2.04}_{-1.70}$		0.9/110
0916	$0.83^{+0.08}_{-0.09}$	$19.88^{+1.00}_{-1.01}$	$44.31^{+0.70}_{-0.67}$		$11.14^{+1.18}_{-1.02}$		$16.82^{+3.24}_{-2.47}$		0.8/110
0917	$1.01^{+0.08}_{-0.09}$	$23.75^{+1.59}_{-1.45}$	$45.83^{+1.06}_{-0.97}$		$8.67^{+1.22}_{-2.26}$		$14.40^{+2.75}_{-2.26}$		0.9/110
<i>RXTE</i>									
95347-02-01-00	$0.44^{+0.02}_{-0.02}$	$16.24^{+0.15}_{-0.15}$	$44.24^{+0.29}_{-0.29}$		$9.01^{+0.36}_{-0.34}$		$8.69^{+0.52}_{-0.49}$		1.2/152
			$106.44^{+2.61}_{-2.57}$		$2.15^{+4.40}_{-1.62}$		$18.50^{+27.35}_{-11.82}$		1.08/156
95347-02-01-01	$0.43^{+0.02}_{-0.02}$	$15.95^{+0.15}_{-0.15}$	$43.92^{+0.29}_{-0.29}$		$9.80^{+0.39}_{-0.34}$		$9.28^{+0.59}_{-0.55}$		1.5/152
			$102.09^{+1.88}_{-1.78}$		$3.49^{+2.34}_{-2.90}$		$17.09^{+5.73}_{-5.15}$		1.14/156
95347-02-01-02	$0.47^{+0.02}_{-0.02}$	$16.26^{+0.18}_{-0.18}$	$43.31^{+0.33}_{-0.33}$		$9.16^{+0.41}_{-0.40}$		$9.00^{+0.63}_{-0.59}$		1.3/152
			$104.88^{+5.24}_{-4.02}$		$7.05^{+3.47}_{-3.35}$		$18.08^{+9.82}_{-6.27}$		1.06/156

### 5.6.2 Pulse phase resolved analysis

During one pulse period, the system is observed from different viewing angles, i.e. we monitor different emitting structures and emission regions or the same regions at different angles. To analyze the spectral changes during one pulse period, we made a pulse phase resolved analysis. The selected pulse phase intervals are shown in Fig. 5.16. For each pulse phase interval, we extracted spectra of the *RXTE* and *INTEGRAL* observations. We summed up the two *INTEGRAL* observations with the lowest luminosity, observation 0916 and 0917, to increase the statistics. The spectra were fitted with the same phenomenological model as in the pulse phase averaged studies (see previous section). In Figure 5.17, the best fit values of the photon index  $\Gamma$  and of the cyclotron line energy  $E_{\text{cyc}}$  are plotted for each observation in different pulse phase intervals (numbered from "1" to "10"). For all individual pulse phase intervals, we applied a linear fit to the  $\Gamma$ -flux and  $E_{\text{cyc}}$ -flux dependencies (solid coral lines in Fig. 5.17). In Figure 5.18, we show the slope values of the linear fit of the  $\Gamma$ -flux and  $E_{\text{cyc}}$ -flux dependencies for different pulse phase intervals.

We observe a decrease of the photon index with increasing flux in all phase bins (Figs. 5.17, 5.18). This behavior was also seen in the pulse phase averaged analysis (see Fig. 5.14). In the right panel of Figure 5.17, the dependence of  $E_{\text{cyc}}$  on the source flux is shown for all phase intervals. For most phase bins, the line energy does not show a clear correlation with the source flux, except for phase bins 8-10, i.e. pulse phases 0.7–1.0. In this interval, we detect an indication of a positive  $E_{\text{cyc}}$ -flux correlation, although with a marginal significance of  $\sim 3\sigma$  (see also Fig. 5.18). A plot of all fit parameters as a function of the pulse phase and the flux is provided in the appendix (Fig. A.1).

To quantify the significance of the flux dependencies, we used the F-test to check whether a linear fit with a non-zero slope is statistically preferred over a fit with a constant. This test evaluates the probability that the improvement of  $\chi^2$ , while moving from a fit with a constant line to a fit with a non-zero slope, is by chance (pure statistical fluctuation). We provide the values of the null hypothesis probabilities  $P$  of all phases in Table 5.4. The  $P$ -values of the photon index reveal a noticeable  $\Gamma$ -flux correlation, while the values of  $E_{\text{cyc}}$  show an indication of an  $E_{\text{cyc}}$ -flux

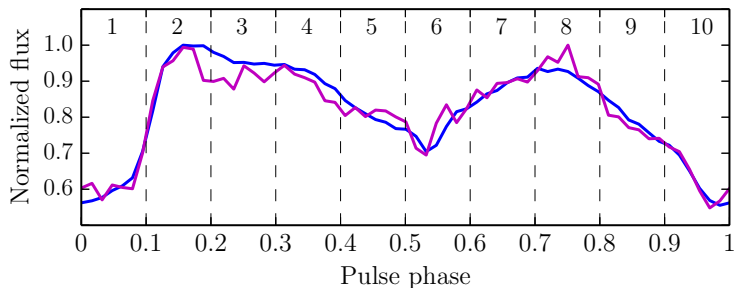


Figure 5.16: The averaged and normalized *RXTE* and *INTEGRAL* pulse profiles of A 0535+26. We accumulated *RXTE* data of observation 95347-02-01-01 from 3–60 keV (magenta) and data of *INTEGRAL* rev. 0912 from 3–80 keV (blue). The pulse phase intervals used for our pulse phase resolved analysis are numbered from "1" to "10" and marked with dashed vertical lines.

correlation in phase bins 0.7–1.0.

To check if the correlations are driven by systematic differences between the two instruments, we re-calculated the slopes and significances using only the *INTEGRAL* data points. The linear fits to the *INTEGRAL* data points yield very similar slopes (in some phase bins the slopes become even higher), although for some phases the fit shows a slight offset with respect to the fit with all observations (*INTEGRAL* and *RXTE*) together. The F-test probability values are shown in the appendix Table A.1. For the two pulses, we find probabilities of  $\sim 0.02$ – $0.2$  for  $\Gamma$ , suggesting that a linear fit is preferred over a fit with a constant. The  $E_{\text{cyc}}$  probability values of pulse phases 0.7–1.0 are 0.081, 0.169 and 0.047. This confirms the trend described in the paragraphs above. In general, we find no indication that the correlations are driven by the systematic differences between the two satellites.

Since an  $E_{\text{cyc}}$ -flux correlation is probably present in the secondary peak, we did another pulse phase resolved analysis in which we analyzed the spectra on the basis of the two pulses of the pulse profile. We choose two broad pulse phase intervals for each observation. For the main peak, we selected pulse phases 0.1–0.5, for the secondary peak - 0.6–1.0. In

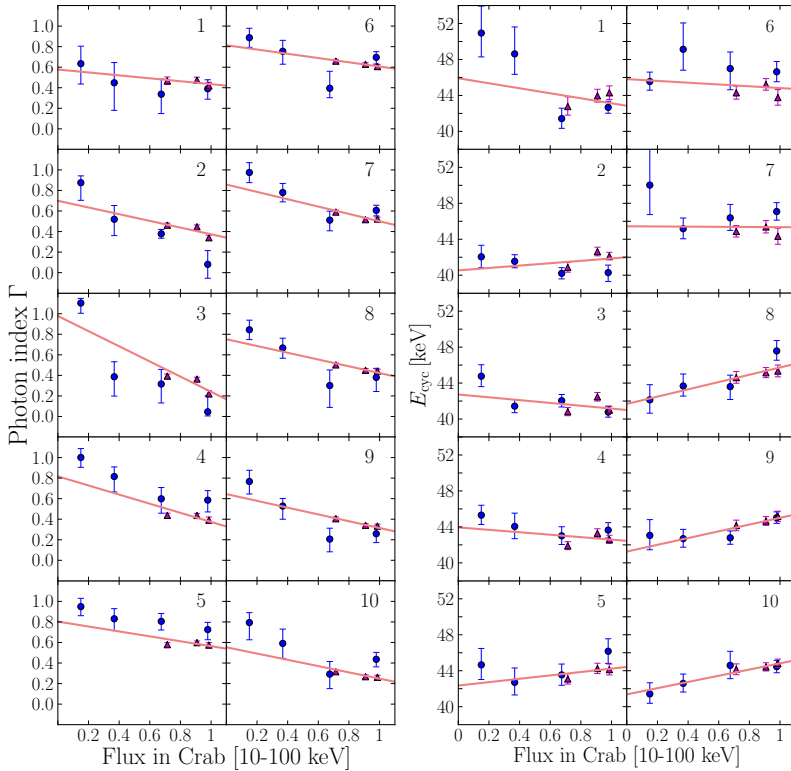


Figure 5.17: The photon index  $\Gamma$  and the cyclotron line energy  $E_{\text{cyc}}$  of A 0535+26 obtained from the *RXTE* and *INTEGRAL* observations for each pulse phase interval (numbered from "1" to "10", see Fig. 5.16). The plots in the *left* panel show the photon index  $\Gamma$  as a function of flux for each pulse phase interval. On the *right*, we show the same for the cyclotron line energy  $E_{\text{cyc}}$ . The *RXTE* observations are marked with magenta triangles, the *INTEGRAL* observations - with blue circles. We summed up the two *INTEGRAL* observations with the lowest luminosity, 0916 and 0917, to improve statistics. In each pulse phase bin, we applied a linear fit to the data (coral line).

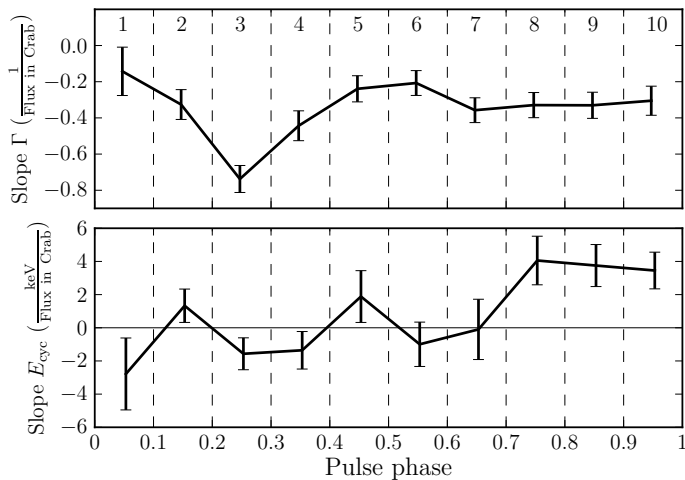


Figure 5.18: The slopes of the linear fits from Fig. 5.17 with the associated  $1\sigma$  uncertainties. Figure is taken from Müller et al. (2013a).

Table 5.4: Probability values of the F-test to evaluate whether a linear fit with a non-zero slope is statistically preferred over a fit with a constant. A low value indicates that a fit with a non-zero slope is preferred to a fit with a constant line.

phase bin	pulse phase	P-value $\Gamma$	P-value $E_{cyc}$
1	0.0–0.1	0.190	0.512
2	0.1–0.2	0.118	0.450
3	0.2–0.3	0.017	0.379
4	0.3–0.4	0.057	0.463
5	0.4–0.5	0.175	0.204
6	0.5–0.6	0.066	0.607
7	0.6–0.7	0.017	1.000
8	0.7–0.8	0.007	0.027
9	0.8–0.9	0.013	0.009
10	0.9–1.0	0.076	0.001

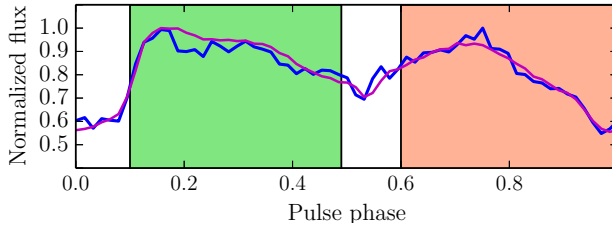


Figure 5.19: The averaged and normalized *RXTE* (observation 95347-02-01-01, 3–60 keV, magenta line) and *INTEGRAL* (rev. 0912, 3–80 keV, blue line) pulse profiles of A 0535+26. We mark the two broad pulse phase intervals, used for the spectral extraction. For the main peak, we extracted spectra in the phase interval 0.1–0.5 (green), for the secondary peak - in 0.6–1.0 (coral).

Figure 5.19, we mark the selected pulse phase intervals in the *RXTE* and *INTEGRAL* pulse profiles with the shaded area. In Figure 5.20, we show the photon index  $\Gamma$  and the cyclotron line energy  $E_{\text{cyc}}$  as a function of the source flux for the two selected pulse phase intervals. The hardness of the continuum is characterized by two independent parameters,  $\Gamma$  and  $E_{\text{rolloff}}$ . To characterize the continuum hardness by one single parameter (e.g. by the photon index  $\Gamma$ ), we fixed the rolloff energy  $E_{\text{rolloff}}$  to its mean value of 16.0 keV for the  $\Gamma$ -flux plot. We detect a harder spectrum for the main peak (smaller  $\Gamma$ ) and a lower  $E_{\text{cyc}}$  compared to the secondary peak. For the main peak (pulse phase 0.1–0.5),  $\Gamma$  and  $E_{\text{cyc}}$  are not correlated with the source flux. While for the secondary peak (pulse phase 0.6–1.0), we notice an indication of a negative  $\Gamma$ -flux and of a positive  $E_{\text{cyc}}$ -flux correlation.

The slopes of the linear fits with the corresponding Pearson correlation coefficients and the associated two-sided null-hypotheses probabilities are specified in Table 5.5. A lower value indicates a higher significance of the correlation.

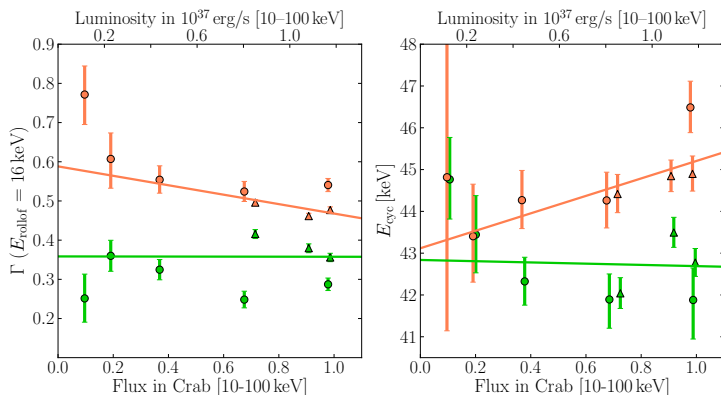


Figure 5.20: The photon index  $\Gamma$  (*left*) and the cyclotron line energy  $E_{\text{cyc}}$  (*right*) are plotted as a function of the flux for the two broad pulse phase intervals shown in Fig. 5.19 (referred to as the main and secondary peaks). The fit parameters of the main peak (pulse phase 0.1–0.5) are plotted in green, of the secondary peak (pulse phase 0.6–1.0) - in coral.

Table 5.5: The slopes of the linear fit to the pulse phase resolved spectral parameters as a function of flux with the corresponding Pearson correlation coefficients and the associated two-sided null-hypotheses probabilities (a lower value indicates a higher significance of the correlation). We give the parameters in pulse phase intervals 0.1–0.5 (main peak) and 0.6–1.0 (secondary peak). The uncertainties of the slopes are at  $1\sigma$  confidence level.

parameter	linear fit $\times (\text{Crab unit})^{-1}$	correlation coefficient	probability
<b>phase 0.1–0.5</b>			
$\Gamma$	$-0.00 \pm 0.03$	$\sim 0.28$	$\sim 0.51$
$E_{\text{cyc}}$	$-0.15 \pm 0.70 \text{ keV}$	$\sim -0.57$	$\sim 0.14$
<b>phase 0.6–1.0</b>			
$\Gamma$	$-0.12 \pm 0.03$	$\sim -0.83$	$\sim 0.01$
$E_{\text{cyc}}$	$2.09 \pm 0.95 \text{ keV}$	$\sim 0.60$	$\sim 0.12$

### 5.6.3 Pulse amplitude resolved analysis

We performed a pulse amplitude resolved spectral analysis similar to Klochkov et al. (2011). A description of the method is given in the following (for detailed explanations see Klochkov et al. 2011). A light curve is extracted with a time resolution that allows to observe single pulses. A bright pulse phase interval is selected in the pulse profile. In this pulse phase interval, an average count rate is calculated, referred to as *pulse amplitude* or *pulse height*. Because of restricted photon statistics, pulses with similar pulse amplitudes are grouped in pulse amplitude intervals with each interval containing similar statistics. For the spectral extraction, good time intervals (GTIs) are compiled for each pulse amplitude interval. The variation of the spectral parameters as a function of pulse amplitude can be analyzed.

Since we want to compare our results to the analysis of Klochkov et al. (2011), we choose the secondary peak in the pulse profile for the spectral extraction which is more pronounced in the observations analyzed by Klochkov et al. (2011). In Figure 5.21, we show the *RXTE* and *INTEGRAL* pulse profiles where we indicate the pulse phase interval used for our analysis.

In Figure 5.22, short fragments of the *RXTE* and *INTEGRAL* light curves are shown along with the repeated averaged pulse profile and the pulse amplitude of each individual pulse. We notice a high pulse-to-pulse variability in the respective light curves. For the *RXTE* analysis, we accumulated all three observations (taken at a similar flux level) to increase the statistics. The three observations are described by following solution for the pulse period and pulse period derivative:  $P = 103.3365$  s and  $\dot{P} \sim 1.5 \times 10^{-8}$  ss $^{-1}$ . We then computed an averaged pulse profile and calculated the pulse amplitudes of each single pulse (marked by the red circles in Fig. 5.22). The distribution of the measured amplitude of individual pulses is shown in Figure 5.23. We accumulated spectra of certain pulse amplitude intervals. For *RXTE*, we selected subsequent pulse amplitude intervals: 850–1040, 1040–1210, 1210–1310, 1310–1480 and 1480–1850 *PCA* counts/s. For *INTEGRAL*, we analyzed only data from rev. 0912 that was taken during the maximum of the outburst and therefore has the best statistics. A section of the *INTEGRAL* light curve and the corresponding pulse amplitude distribution are shown



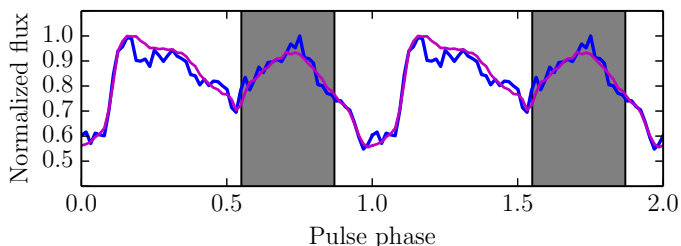


Figure 5.21: The averaged and normalized *RXTE* (observation 95347-02-01-01, 3–60 keV, magenta line) and *INTEGRAL* (rev. 0912, 3–80 keV, blue line) pulse profiles of A 0535+26. We marked the pulse phase interval that we used for the pulse amplitude resolved studies.

in Figures 5.22 and 5.23. To accumulate spectra, we selected five pulse amplitude intervals: 100–210, 210–235, 235–260, 260–290 and 290–450 *ISGRI* counts/s.

The best-fit parameters of  $\Gamma$  and  $E_{\text{cyc}}$  as a function of pulse amplitude for the *RXTE* and *INTEGRAL* data are shown in Figure 5.24. For both instruments, the photon index decreases with increasing pulse amplitude. For the  $\Gamma$  plots, we fixed the rolloff energy to  $E_{\text{rolloff}} = 15.2$  keV for *RXTE* and  $E_{\text{rolloff}} = 15.5$  keV for *INTEGRAL* to characterize the hardness of the spectrum by one single parameter. For the plot of the cyclotron line energy  $E_{\text{cyc}}$  all parameters were kept free. We see an indication of a positive  $E_{\text{cyc}}$ -pulse amplitude correlation in the *RXTE* analysis while we do not notice any correlation in the *INTEGRAL* analysis. The results of the linear fit with the corresponding Pearson correlation coefficients and the associated two-sided null-hypotheses probabilities are listed in Table 5.6.

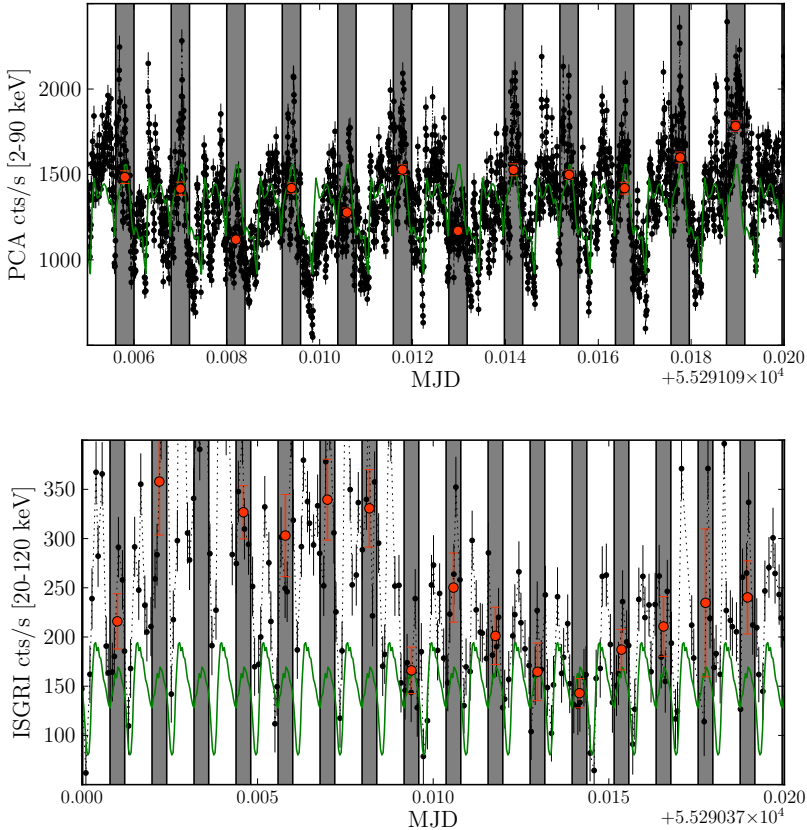


Figure 5.22: The *RXTE* (*top*) and *INTEGRAL* (*bottom*) light curves of A 0535+26 together with the overplotted repeated averaged pulse profile (solid green curve). We marked the pulse phase interval used for our pulse amplitude resolved analysis by the shaded areas. In the upper plot, we show a section of the 2–90 keV *RXTE/PCA* light curve of observation 95347-02-01-01, in the plot below - of the 20–120 keV *INTEGRAL/ISGRI* light curve of rev. 0912. We notice a high pulse-to-pulse variability in the respective light curves. The pulse amplitude (average count rate in the selected pulse phase interval) of each individual pulse is indicated with red circles.

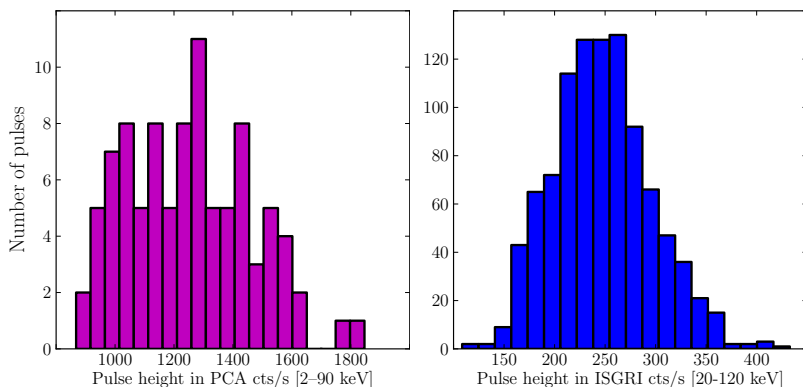


Figure 5.23: The distribution of individual pulse amplitudes of *RXTE* (left) and of *INTEGRAL* observation 0912 (right).

Table 5.6: The slopes of the linear fits to  $\Gamma$  and  $E_{\text{cyc}}$  as a function of pulse amplitudes with the corresponding Pearson correlation coefficients and the associated two-sided null-hypotheses probabilities (a lower value indicates a higher significance of the correlation). The uncertainties of the slopes are at  $1\sigma$  confidence level.

parameter	linear fit $\times (PCA/ISGRI \text{ cts s}^{-1})^{-1}$	correlation coefficient	probability
<b><i>RXTE</i> observations</b>			
$\Gamma$	$-9.12 \pm 1.84 \times 10^{-5}$	$\sim -0.99$	$\sim 6.89 \times 10^{-4}$
$E_{\text{cyc}}$	$2.02 \pm 1.26 \times 10^{-3} \text{ keV}$	$\sim 0.78$	$\sim 0.12$
<b><i>INTEGRAL</i> rev. 0912</b>			
$\Gamma$	$-5.79 \pm 1.66 \times 10^{-4}$	$\sim -0.96$	$\sim 0.01$
$E_{\text{cyc}}$	$0.69 \pm 6.78 \times 10^{-3} \text{ keV}$	$\sim -0.17$	$\sim 0.78$

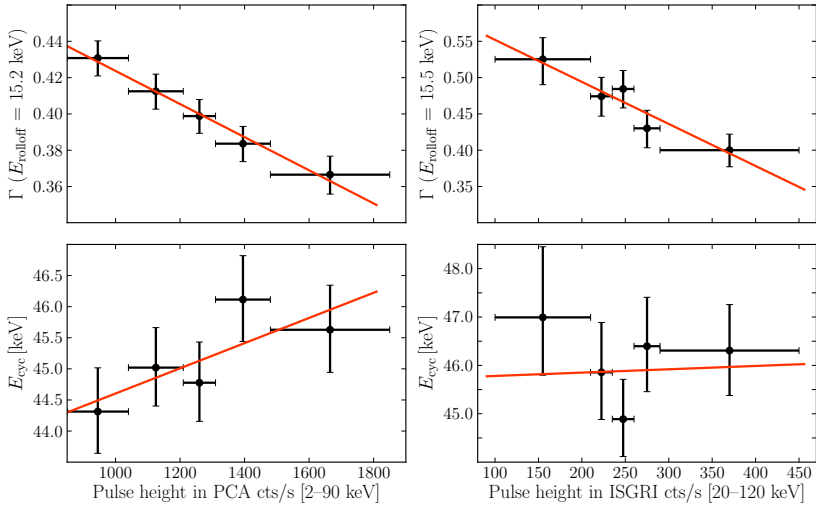


Figure 5.24:  $\Gamma$  and  $E_{\text{cyc}}$  as a function of pulse amplitudes of all *RXTE* observations (*left*) and of *INTEGRAL* observation 0912 (*right*). To characterize the hardness of the continuum by one single parameter, we fixed the rolloff energy for the  $\Gamma$ -amplitude plots to  $E_{\text{rolloff}} = 15.2 \text{ keV}$  (*RXTE*) and  $E_{\text{rolloff}} = 15.5 \text{ keV}$  (*INTEGRAL*). The vertical error bars indicate the  $1\sigma$  uncertainties. The horizontal error bars indicate the pulse amplitude bins used to accumulate the spectra. In solid red lines, we show the linear fit to the data.

### 5.6.4 Discussion

As reported in Sections 5.6.1, 5.6.2, 5.6.3 and Müller et al. (2013a), the data indicate a hardening of the continuum with increasing flux in the phase averaged, pulse phase resolved and pulse amplitude resolved analyses. We see an indication of a positive  $E_{\text{cyc}}$ -flux correlation in some phase bins, even though with a small significance ( $\sim 3\sigma$ ). In the phase averaged analyses, the cyclotron line centroid energy indicates some variation (Fig. 5.14) but does not show a correlation with the luminosity of the source. This behavior is known from previous analyses of the source (Caballero et al. 2007, 2008, 2011c).

#### Phase averaged spectral analysis

A dependence of the cyclotron line centroid energy on the source luminosity was reported for several accreting X-ray pulsars (e.g. Sec. 2.3.1). A negative  $E_{\text{cyc}}$ -flux correlation accompanied by a softening of the spectrum with increasing flux has been observed in the *super-critical* sources V 0332+53 and 4U 0115+63 (Mowlavi et al. 2006, Tsygankov et al. 2006, 2007, 2010, for 4U 0115+63 see however Müller et al. 2013b). For these pulsars, the infalling matter is most likely decelerated in a radiative shock, whose height increases with increasing luminosity of the source (Basko & Sunyaev 1976b, Becker et al. 2012). Poutanen et al. (2013) propose an alternative model, in which the CRSF is formed by reflection of emitted radiation from the accretion column on the neutron star surface. Here, an increase of the mass accretion rate, i.e. the luminosity, is reflected by a higher accretion column and thus a higher fraction of intercepted column radiation. A positive correlation and a hardening of the spectrum with increasing flux was detected for the *sub-critical* sources Her X-1 and GX 304-1 (Staubert et al. 2007, Klochkov et al. 2012). In the sub-critical accretion regime, the infalling matter is most likely stopped by the Coulomb drag and collective plasma effects (Basko & Sunyaev 1976b, Staubert et al. 2007, Becker et al. 2012).

The transition between the two accretion scenarios is associated with a critical luminosity  $L_{\text{crit}}$  (Basko & Sunyaev 1976b). Calculations of  $L_{\text{crit}}$  are given in Becker et al. (2012) or Mushtukov et al. (2014), based on different models/assumptions (see Sec. 2.2.2). In Table 2.1 of Section 2.2.2, we report calculations of  $L_{\text{crit}}$  by Becker et al. (2012) for

a number of known cyclotron line sources. For A 0535+26, Becker et al. (2012) predict a value of  $L_{\text{crit}} \sim 6.78 \times 10^{37}$  erg/s. The peak flux during the April 2010 outburst of A 0535+26 reached  $\sim 1.2 \times 10^{37}$  erg/s, thus  $\sim 5$ –6 times below  $L_{\text{crit}}$ . Therefore, A 0535+26 is expected to accrete in a sub-critical accretion regime during that outburst. Our data indicate a hardening of the X-ray continuum. However, we do not observe a positive  $E_{\text{cyc}}$ -flux correlation as it was detected in the other sub-critical sources Her X-1 and GX 304-1. If we assume that A 0535+26 operates in a similar accretion regime as Her X-1 and GX 304-1, the positive  $E_{\text{cyc}}$ -flux correlation might be smeared due to a special orientation of the system with respect to the observer's line of sight and/or a special geometry of the emitting structure. Otherwise, A 0535+26 could represent another accretion regime, in which the height of the emitting region does not change significantly in the observed range of luminosities (if we accept the model by Becker et al. 2012).

In Figure 2.9, we show the dependencies of  $E_{\text{cyc}}$  on the source luminosity and the corresponding critical luminosity for a number of accreting pulsars. If we compare A 0535+26 to the other sub-critical sources, Her X-1 and GX 304-1, we notice that the luminosity of A 0535+26 is far below  $L_{\text{crit}}$ . Her X-1 and GX 304-1 are much closer to their respective critical luminosities. Therefore, the accretion geometry of A 0535+26 might indeed be different compared to the other sub-critical pulsars. This idea seems to be supported by a new analysis of a giant outburst of A 0535+26 by Caballero et al. (2012). During this outburst, A 0535+26 reached a luminosity of  $\sim 3.8$  Crab, which is comparable to the luminosity range of Her X-1 and GX 304-1. In this preliminary analysis, some measurements of  $E_{\text{cyc}}$  suggest an increase of the CRSF at high fluxes, i.e. a positive  $E_{\text{cyc}}$ -flux correlation (Fig. 1 in Caballero et al. 2012).

### Pulse phase resolved spectral analysis

In Section 5.6.2, we report the results of the pulse phase resolved analysis. We notice a variation of the photon index and the cyclotron line energy with pulse phase and with luminosity at individual pulse phases (Fig. 5.17, 5.18). To interpret the results of the pulse phase resolved analysis, it is important to understand the geometry of the rotating neutron star and of its emitting regions. This can be done applying, e.g.

the decomposition method by Kraus et al. (1995). This method is based on the assumption that the asymmetry observed in most pulse profiles is caused by a distorted magnetic dipole field. The observed pulse profiles can be decomposed into single pole contributions and information about geometry and beam pattern can be derived. Caballero et al. (2011a) applied this method to A 0553+26. They found that the pulse profiles of the source can be reproduced in a model, including a hollow column, a thermal halo and taking into account relativistic light deflection in the strong gravitational field of the neutron star. Based on the results of Caballero et al. (2011a), we infer the following geometrical model that can produce the observed pulse profiles: one magnetic pole passes through the observer's line of sight, whereas the second pole is never seen directly from the top but only through the gravitationally bent radiation from the lateral emission of the accretion column and its thermal scattering halo (see Fig. 5.11).

Since we observe similar pulse profiles as those used by Caballero et al. (2011a) for the decomposition method (e.g. Figs. 5.6, 5.8), we adopt the reconstructed geometry to explain our data. In Section 5.6.2, we reported the hardness of the continuum X-ray spectrum in the main and secondary peak (Fig. 5.20): the spectrum of the main peak is slightly harder compared to the secondary peak. Harder photons can escape more effectively in the direction parallel to the magnetic field lines because the magnetized plasma gets optically thin for photons with  $E < E_{\text{cyc}}$  propagating in this direction due to the angular dependence of the scattering cross section in the magnetic field (Harding & Lai 2006). According to the assumed geometry, during the main peak, we observe harder photons originating in the polar caps and escaping the accretion column from the top along the magnetic field lines (Caballero 2009). During the secondary peak, about half a phase later, we observe the lateral emission of the accretion column and their thermal halos. The variation of the centroid cyclotron line energy with pulse phase (Fig. 5.17) can be caused by the changing viewing angles on the scattering region and by the dependence of the magnetic scattering cross sections on the angle between the magnetic field and the line of sight (Harding & Daugherty 1991).

We also observe a variation of the  $\Gamma$  and  $E_{\text{cyc}}$  values as a function of flux in the individual phase bins (Figs. 5.17, 5.18, 5.20). The photon index  $\Gamma$

decreases significantly with increasing flux for most phase bins (left panel in Fig. 5.17 and upper panel in Fig. 5.18), while the cyclotron line energy  $E_{\text{cyc}}$  only shows a marginal indication for a positive correlation with flux during the secondary peak of the pulse profile (Fig. 5.18 and Fig. 5.20, phase bins 8–10). In the section above, we outlined a possible geometry of accretion at different pulse phases. In this model, the secondary peak is caused by the emission perpendicular to the accretion column(s) axis/magnetic field lines. At these inclinations, when the radiation is emitted nearly perpendicular to the local magnetic field, the CRSFs are expected to be deeper and narrower (e.g. Schönherr et al. 2007, Ferrigno et al. 2011, and references therein). Therefore, the viewing angle might support the detection of an  $E_{\text{cyc}}$ -flux correlation in this pulse phase. This property is smeared out in the pulse phase averaged analysis, hence we did not find any indication for a positive  $E_{\text{cyc}}$ -flux correlation.

### Pulse amplitude resolved spectral analysis

In Section 5.6.3, we describe the spectral variability of the  $\Gamma$  and  $E_{\text{cyc}}$  parameters with pulse amplitude. We find a hardening of the power law (decrease of  $\Gamma$ ) with increasing pulse amplitude in the *RXTE* and *INTEGRAL* data. An indication of a positive  $E_{\text{cyc}}$ -pulse amplitude correlation is only detected for *RXTE* (Fig. 5.24). The results of our analysis (i.e. a hardening of the continuum spectrum and a positive  $E_{\text{cyc}}$  correlation with pulse amplitude) are in agreement with earlier analyses by Klochov et al. (2011) on the basis of observations of an outburst in 2005 with better photon statistics.

Why do we not observe the positive correlation between  $E_{\text{cyc}}$  and flux in the pulse phase averaged spectra? In Müller et al. (2013a), we give the following qualitative explanation for this discrepancy: The source exhibits a relatively broad distribution of individual pulse amplitudes due to a strong pulse-to-pulse variability (Fig. 5.23). The pulse phase averaged spectra are accumulated over longer time scales, thus, containing the contributions by pulses with different amplitudes. This variability might lead to a considerable smearing effect, suppressing the effect of a possible  $E_{\text{cyc}}$ -flux variation in the pulse phase averaged analysis.



# Chapter 6

## Her X-1

### 6.1 System overview

The X-ray binary system Her X-1/HZ Her was discovered by *UHURU* in 1972 (Tananbaum et al. 1972). Since then, Her X-1 is one of the most studied X-ray binary systems. The system is formed by a magnetized neutron star and the A/F companion HZ Her with masses of respectively  $\sim 1.5$  and  $2.3 M_{\odot}$  (Bahcall & Bahcall 1972, Forman et al. 1972, Liller 1972, Crampton 1974, Reynolds et al. 1997). The mass of the donor star puts the system between high- and low-mass X-ray binary systems. The distance of the system is  $\sim 7$  kpc (Howarth & Wilson 1983, Reynolds et al. 1997). Her X-1 is seen nearly edge-on with an inclination of  $i \geq 85^{\circ}$  (Gerend & Boynton 1976, Dennerl 1991). In Table 6.1, the newest orbital ephemeris by Staubert et al. (2009) are listed.

Howarth & Wilson (1983) found an intrinsic X-ray luminosity of  $4 \times 10^{37}$  erg/s (assuming a distance of 6 kpc). The observed X-ray flux is strongly modulated by different phenomena: a 1.24 s spin period of the neutron star, a 1.7 d orbital period of the system, that causes the obscuration of the X-ray emitting region by the stellar companion every orbit for  $\sim 6$  h, and a  $\sim 35$  d super-orbital period attributed to the precessing warped accretion disk periodically blocking the observer's line of sight (see e.g. Tananbaum et al. 1972, Giacconi et al. 1973, Katz 1973, Deeter & Boynton 1976, Gerend & Boynton 1976).

Table 6.1: Ephemeris as reported by Staubert et al. (2009).

$T_{\pi/2}(0)$ [MJD]	46359.8719408(6)
$P_{\text{orb}}$ [d]	1.700167590(2)
$\dot{P}_{\text{orb}}$ [dd $^{-1}$ ]	$(-4.85 \pm 0.13) \times 10^{-11}$
$a \sin i$ [lt-s]	13.1831(4)
eccentricity $\epsilon$	$(4.2 \pm 0.8) \times 10^{-4}$
omega [deg]	$96.0 \pm 10.0$

The emitted X-rays illuminate the side of HZ Her facing the neutron star, leading to a modulation of the optical emission with the binary period. The optical and UV emission is mainly produced by the heated surface of the primary star (Howarth & Wilson 1983, Cheng et al. 1995, Reynolds et al. 1997). About half of the hard X-rays are reprocessed in the photosphere of the optical companion and converted to optical radiation (Howarth & Wilson 1983).

As HZ Her most probably fills its critical Roche lobe, the material leaves HZ Her through the inner Lagrangian point and thus has enough angular momentum to form an accretion disk around the compact object. The accretion disk is a strong source of optical radiation. It also casts shadows onto the irradiated (by the central X-ray source) surface of the optical component.

## 6.2 Timing properties

### 6.2.1 35 day periodicity

The X-ray lightcurve of Her X-1/HZ Her shows a 35 d periodicity. The 35 d cycle segments in 2 on-states (high X-ray flux) and 2 off-states (low X-ray flux): a main-on with a duration of  $\sim 11$  d and a short-on with a duration of  $\sim 8$  d, separated by two off-states ( $\sim 7$ – $8$  d). During main-ons the maximum X-ray flux reaches about 5 times of the maximum X-ray flux during short-ons. The main-on state covers 35 d phases  $\Psi_{35} \sim 0.0 - 0.31$  and the short-on state covers  $\Psi_{35} \sim 0.57 - 0.79$ , with phase  $\Psi_{35} = 0.0$  defined as the turn-on of the main-on state (Scott & Leahy 1999). In Figure 6.1, we show the modulation of the X-ray flux, attributed to

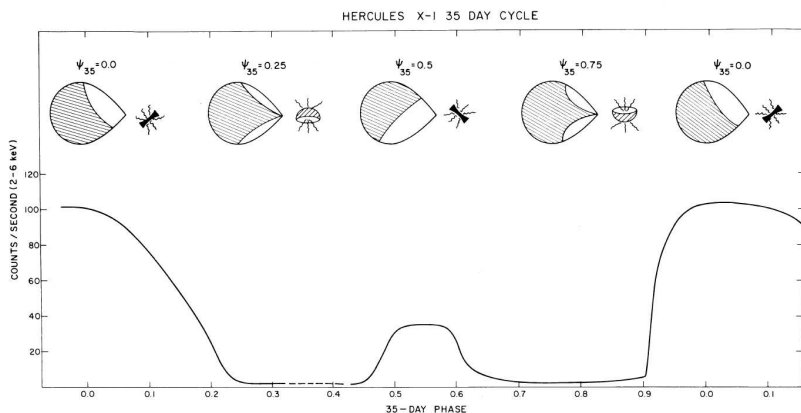


Figure 6.1: The modulation of the X-ray flux of one 35 d cycle measured by *Uhuru*. The patterns at the top show the possible configuration of a neutron star plus companion and the precessing accretion disk that opens the view onto the X-ray emitting region in on-states, while it shadows the region in off-states. In this interpretation, the 35 d period corresponds to the precession period of the disk. Figure is taken from Jones & Forman (1976).

a precessing accretion disk, of one 35 d cycle as suggested by Jones & Forman (1976).

The 35 d periodicity most probably results from the obscuration of the X-ray emitting region by a tilted and warped precessing accretion disk (e.g. Katz 1973, Gerend & Boynton 1976, Shakura et al. 1999). According to the model by Petterson (1975, 1977), the turn-ons occur when the outer rim of a tilted, twisted, counter-precessing accretion disk clears the view onto the neutron star Her X-1. The turn-ons end when the inner edge of the accretion disk passes the line of sight. In this model, the line of sight of the observer is close to the orbital plane of the system and the presence of main-on and short-on states can be attributed to a different angle of the observer with respect to the accretion disk. In Figure 6.2, a model of the accretion disk as proposed by Scott et al. (2000) is shown together with the observed X-ray flux.

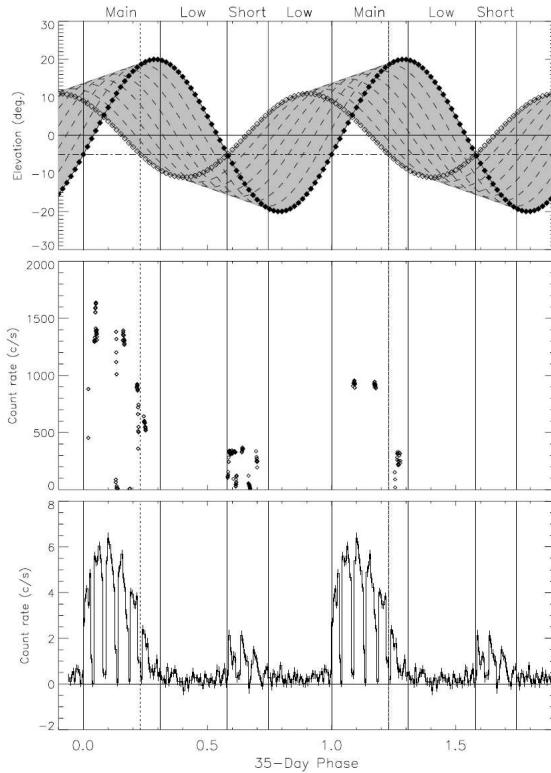


Figure 6.2: The proposed model for the 35d modulation of the X-ray flux is the occultation of the neutron star (X-ray source) by the tilted precessing accretion disk. In the *top panel*, the view of the disk as seen from the neutron star is shown. The outer rim of the disk is marked by filled diamonds, the inner edge - by open diamonds. The elevation of the observer is indicated by a horizontal dashed line. The turn-on times are marked by solid vertical lines. The dotted vertical lines indicate the time when the inner rim of the disk interrupts the direct view on the X-ray source. In the two panels *below*, the *Ginga* 1–37 keV flux and the *RXTE/ASM* 2–12 keV light curves are shown. The neutron star appears to the observer as a point source from the outer disk rim and as an extended source from the inner disk rim. Figure is taken from Scott et al. (2000).

The system also undergoes phases during which the X-ray flux is highly reduced, so called *anomalous low states* (ALs) (e.g. Parmar et al. 1985, 1999, Vrtilik et al. 1994). ALs were observed in 1983 (Parmar et al. 1985), 1993 (Mihara et al. 1994, Vrtilik et al. 1994), 1999 (Parmar et al. 1999) and 2003 (Boyd et al. 2004). The duration of ALs can be up to many 35 d cycles during which the X-ray flux is substantially decreased and the pulsed X-ray emission (and consequently the 35 d cycle) virtually disappears, while the optical and UV fluxes still show modulations (e.g. Parmar et al. 1985, 1999, Vrtilik et al. 1994). The decrease of the accretion rate is not big enough to explain the drop in the X-ray flux. Vrtilik et al. (1994) suggest, that during ALs, the disk lies down to the orbital plane and thus permanently blocks the line of sight to the neutron star. A change in torque on the neutron star, correlated with the observed strong spin-down, can shift the disk into the line of sight, thereby obscuring the X-ray emitting regions. The observed pulsations in the optical and UV light curves are attributed to X-ray heating of the companion HZ Her. The observed drop in UV flux can be attributed to the disk being in the line of sight and screening the UV emission originating from X-ray heating of the disk.

The X-ray light curve also exhibits dips. Some of them seem to be related to the orbital phase and formed by absorption in the gas stream from the companion to the accretion disk (Giacconi et al. 1973). The system presents different kinds of dips: Pre-eclipse dips are seen during the first orbits after turn-on. At the beginning, they occur during the eclipse and then move to earlier orbital phases. Post-eclipse recoveries are occasionally observed as an extension of the eclipse duration. Anomalous dips are observed at phase 0.45–0.65 and are related to an anisotropic X-ray heating of the optical star atmosphere due to the tilted and warped accretion disk. Thereby, gas streams are formed and can eventually cross the line of sight to the observer before merging with the accretion disk (Shakura et al. 1999).

### 6.2.2 Pulse period evolution

Basic accretion theory suggests a positive correlation between the spin-up rate of a pulsar and the observed flux (Pringle & Rees 1972, Davidson & Ostriker 1973, Lamb et al. 1973). If the accretion rate and hence the

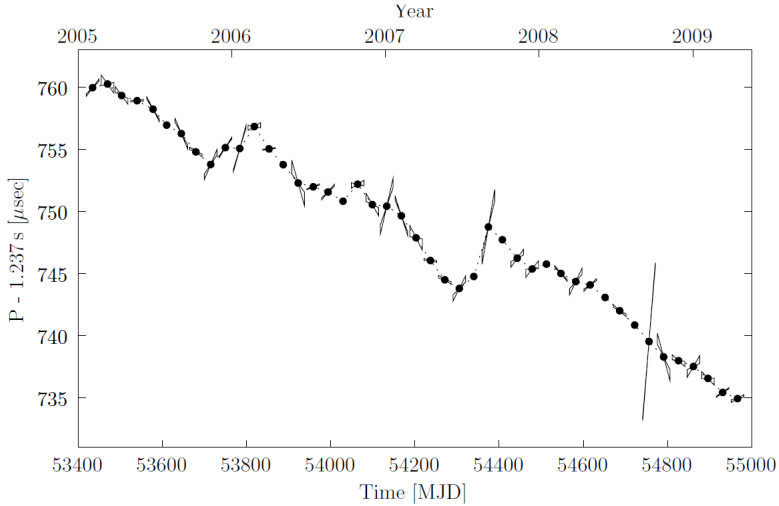


Figure 6.3: The pulse period measured with *Swift*/*BAT* is shown as a function of the time. The slopes ( $\dot{P}$ ) of the pulse period of each observation with the associated uncertainties are indicated by the cones. Figure is taken from Klochkov et al. (2009).

flux increases, a torque is exerted on the neutron star which experiences a change of the angular momentum and therefore shows a spin-up. This behavior is observed in many pulsars. In Her X-1, the pulse period changes within single main-on states, on time scales shorter than the 35 d super-orbital period (Klochkov et al. 2008, 2009). In Figure 6.3 (from Klochkov et al. 2009), we show the spin-up and spin-down episodes of Her X-1 as observed with *Swift*/*BAT*. The system experiences a long-term spin-up ( $\dot{P} = -1.8203(3) \times 10^{-13} \text{ ss}^{-1}$ ) that is interrupted by short spin-down episodes (Klochkov et al. 2009). As expected in basic accretion theory (e.g. Pringle & Rees 1972, Ghosh & Lamb 1979b), the spin-down rate is found to be anti-correlated with the maximum X-ray flux (Klochkov et al. 2009). Klochkov et al. (2009) observed Her X-1 with *Swift*/*BAT* over several years and found that during spin-down episodes, the torques are up to 5 times larger than during spin-up episodes. The

reason for this behavior is still unknown. A possible explanation is a change in the accretion regime. Strong mass ejection episodes (strong disk outflows) lead to an additional loss of angular momentum and therefore to strong spin-down episodes (Klochkov et al. 2009). Ejection of matter can explain various properties of the system Her X-1/HZ Her: Crosta & Boynton (1980) found a larger mass accretion rate onto the outer rim of the accretion disk around Her X-1 than required to maintain the observed luminosity; the decrease of the orbital period of the system can be caused by outflows from the disk (Deeter et al. 1991); Schandl & Meyer (1994) assigned the disk wind to the irradiation of disk matter by Her X-1; indications of gas outflows were found in the UV spectrum of the source (Boroson et al. 2001, Vrtilik et al. 2001); the presence of a coronal disk wind was suggested by Ji et al. (2009); Klochkov (2007), Staubert et al. (2009) showed that the observed decrease of the orbital period requires substantially non-conservative mass transfer. The idea of increased mass outflows is discussed in more detail in Section 7.5.

### 6.2.3 Pulse profiles

The 1.24 s pulse profiles of Her X-1 are highly energy-dependent and vary as a function of the 35 d phase and even throughout individual on-states (Doxsey et al. 1973, Deeter & Boynton 1976, Trümper et al. 1986, Deeter et al. 1998, Scott et al. 2000, Klochkov et al. 2008, Staubert et al. 2013). Typical pulse profiles of Her X-1 are shown in Figures 6.4 and 6.5.

The main-on pulse profile is asymmetric with a double-peaked main peak that gets single-peaked and narrower at higher energies. The intensity of the various components is found to vary during the time of a main-on ( $\Psi_{35} \sim 0.0 - 0.31$ , Deeter et al. 1998, Klochkov et al. 2008). At the start of the main-on, the pulse profile is more structured and comprises many components (Deeter et al. 1998). Towards the end of the main-on, the main peak gets stronger and narrower and the interpulse nearly disappears (Fig. 6.6) (Klochkov et al. 2008, Staubert et al. 2013). The pulsed fraction increases with energy, which is typical for accreting X-ray pulsars (Klochkov et al. 2008). A peculiarity of Her X-1 is the shape of the pulse profiles, regularly changing with 35 d phase, which allows to determine the turn-on time of the main-on through the observation of pulse profiles within this main-on (Staubert et al. 2013).

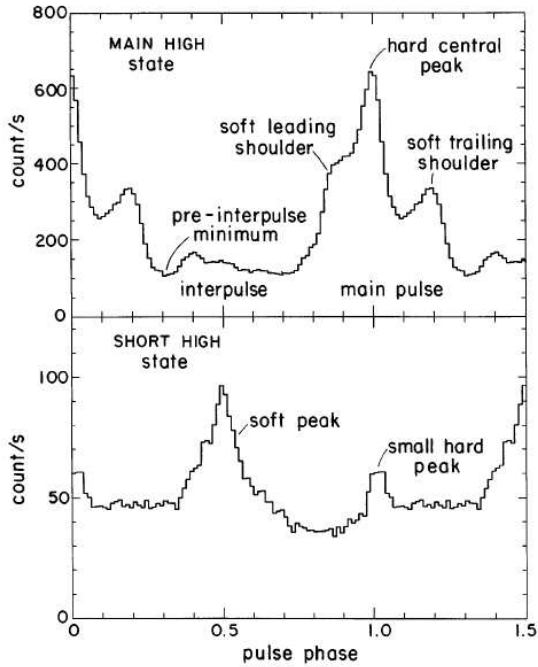


Figure 6.4: Typical pulse profiles of the main- and short-on states of Her X-1. The pulse profiles were obtained in the 9.4–14 keV energy band with *Ginga*. Figure is taken from Deeter et al. (1998).



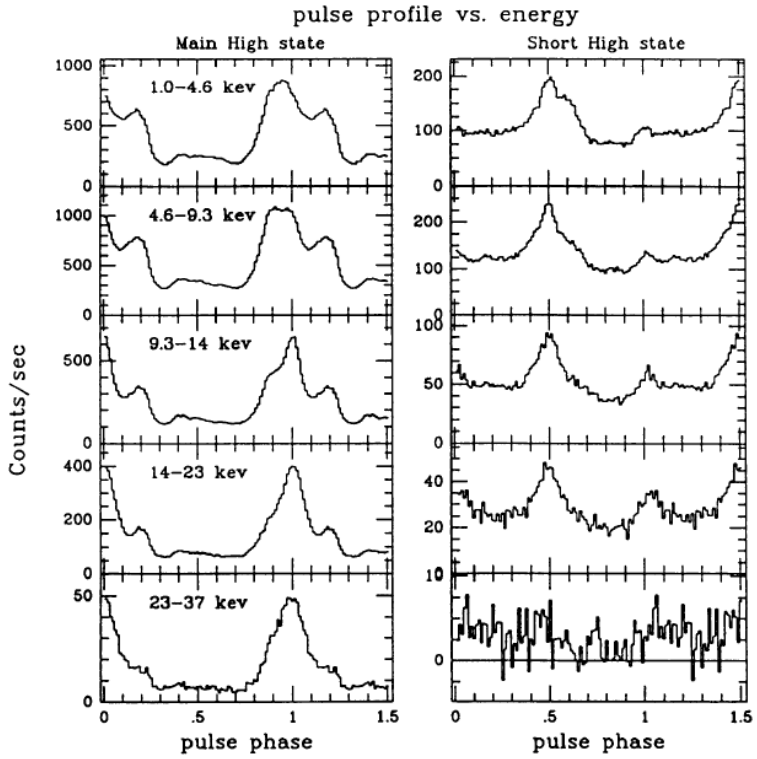


Figure 6.5: Pulse profiles of 5 different energy bands are shown for the main- and short-on states of Her X-1. Figure is taken from Deeter et al. (1998).

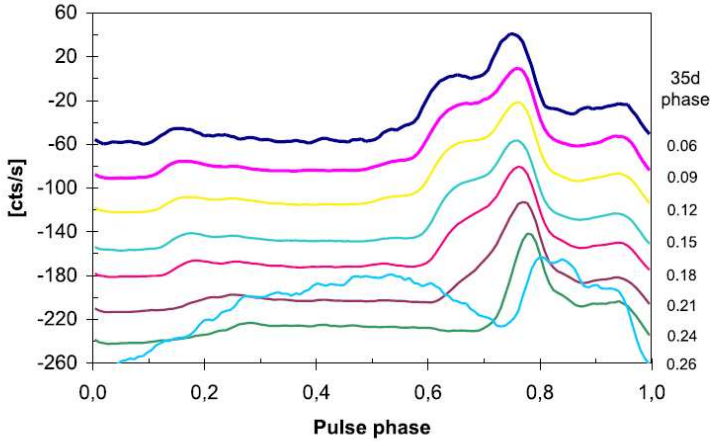


Figure 6.6: *RXTE/PCA* main-on pulse profiles of Her X-1 in the 9–13 keV energy range as a function of 35 day phase. Figure is taken from Staubert et al. (2013).

### 6.3 Spectral properties

The X-ray spectrum of Her X-1 can be described by following components: a thermal blackbody component ( $kT_{\text{BB}} \sim 0.1$  keV) at low energies ( $E < 1$  keV), a power law with photon index  $\Gamma \sim 0.9 - 1.0$  up to  $\sim 10$  keV with an exponential cutoff ( $E_{\text{cut}} \sim 20$  keV), an Fe  $K\alpha$  emission feature at  $\sim 6.5$  keV and an absorption feature at around 40 keV (see Fig. 6.7 and 6.8), interpreted as a cyclotron resonant scattering feature (CRSF) (see Sec. 2.3.1). The CRSF was detected in 1976 and yields the first direct measurement of the magnetic field strength of a neutron star (Trümper et al. 1978). The centroid energy of the CRSF is found to be positively correlated with the X-ray flux (Staubert et al. 2007, Vasco et al. 2011, also see Sec. 5.6.4).

It is generally assumed that the iron line originates from fluorescence of cold material that is illuminated by the X-ray beam (Ramsay et al. 2002). However, it is still not clarified where the fluorescence takes place.

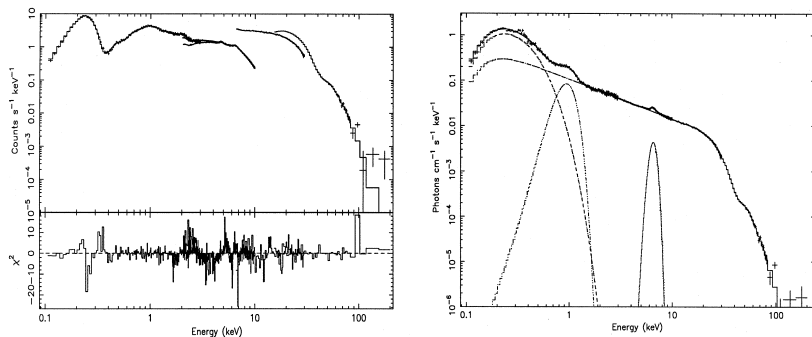


Figure 6.7: The broad band (0.1–200 keV) spectrum of Her X-1 from *BeppoSAX* is shown. The count rate spectrum is shown in the *left panel*. The *right panel* shows the deconvoluted photon spectrum with the indicated spectral components. The spectrum is fitted by a 0.1 keV blackbody, a power law with a high energy cutoff, Fe L and K features at 1 keV respectively 6.5 keV and a CRSF at  $\sim 40$  keV. Figure is taken from dal Fiume et al. (1998).

Ramsay et al. (2002) propose reprocessing of soft emission from cold material around the illuminated spot as a possible origin of the 6.4 keV line. Others (e.g. Choi et al. 1994) suggest the emission from an accretion disk corona, from the accretion column, the outer edge of the accretion disk or a region at the Alfvén radius (also see discussion in Vasco 2012).

Especially in the low- and short-on state, many narrow emission lines from a photoionized plasma are detected (Jimenez-Garate et al. 2002). It is difficult to observe these lines during the main-on state, since the continuum dominates the spectrum. The emission lines probably result from the recombination of electrons and ions and from subsequent radiative cascades (Jimenez-Garate et al. 2002). A potential line forming region is an accretion disk atmosphere or corona or the illuminated face of HZ Her (Jimenez-Garate et al. 2002).

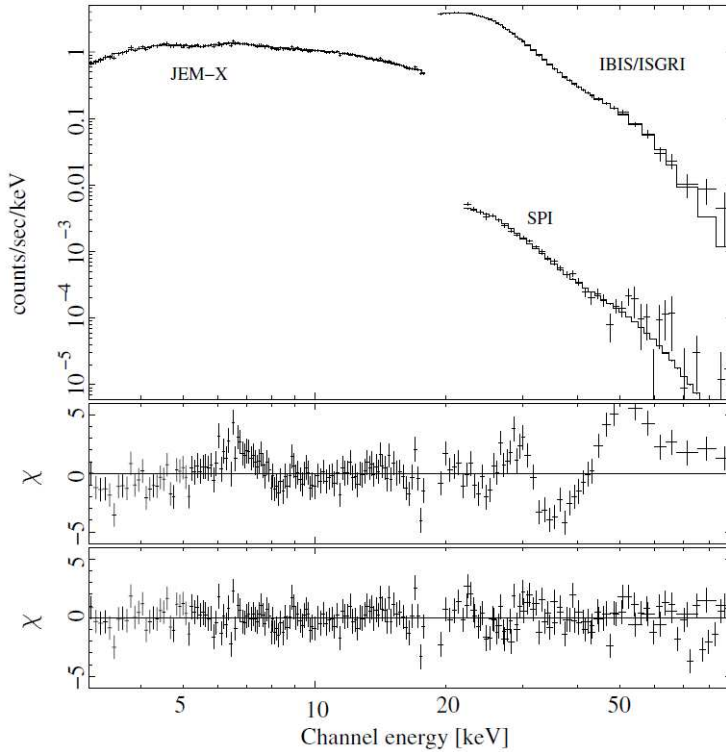


Figure 6.8: The *INTEGRAL* spectrum taken at the start of two main-ons is shown. The middle and lower panels display the residuals after fitting the spectrum with a power law with an exponential cutoff (*middle*) and after inclusion of an iron emission line at around 6.4 keV and an absorption line at  $\sim 40$  keV (*bottom*). Figure is taken from Klochkov et al. (2008).

**Pulse phase resolved analysis**

As many other pulsars, Her X-1 also exhibits spectral changes during a pulse phase (Pravdo et al. 1978, Pravdo et al. 1979, McCray et al. 1982, Voges et al. 1982, Soong et al. 1990, Kunz et al. 1996, Endo et al. 2000, Lutovinov et al. 2000, Zane & Ramsay 2001, Klochkov et al. 2008, Vasco et al. 2013). Vasco et al. (2013) confirmed a strong decrease of the photon index and a higher cyclotron line energy during the main peak. The photon index shows a narrow dip close to the left shoulder (referred to as leading shoulder in Deeter et al. 1998, Fig. 6.4) of the main peak (around phase 0.61). The iron line intensity also varies during one pulse phase. The intensity is slightly increasing until reaching the left shoulder ( $\sim$  phase 0.7), then nearly drops to zero during the main peak and reaches its start value again at around phase 0.9 (Choi et al. 1994, Zane et al. 2004, Vasco et al. 2013).



# Chapter 7

## *XMM-Newton* observations of Her X-1

### 7.1 Observations

We analyzed 4 *XMM-Newton* observations of Her X-1. A list of the observations is shown in Table 7.1. The individual observations have an exposure of about 13–30 ks and were taken during main-on states of the source from July 2011 to April 2012. In Figure 7.1, we plot the orbital *Swift/BAT* light curves of the respective main-ons with the marked time intervals of the 4 *XMM-Newton* observations. The observations are taken at 35 d precession phases  $\Psi_{35} \sim 0.03$  (obs 05),  $\Psi_{35} \sim 0.12$  (obs 06),  $\Psi_{35} \sim 0.10$  (obs 08) and  $\Psi_{35} \sim 0.09$  (obs 09). Figure 7.2 shows the pulse period and pulse period derivative of subsequent main-ons of Her X-1 as measured by *Swift/BAT*.

### 7.2 Data reduction

The data reduction was carried out with the *XMM-Newton* Scientific Analysis System (SAS). The data files consist of the observational data files (ODF) that include the raw science event files, the housekeeping data

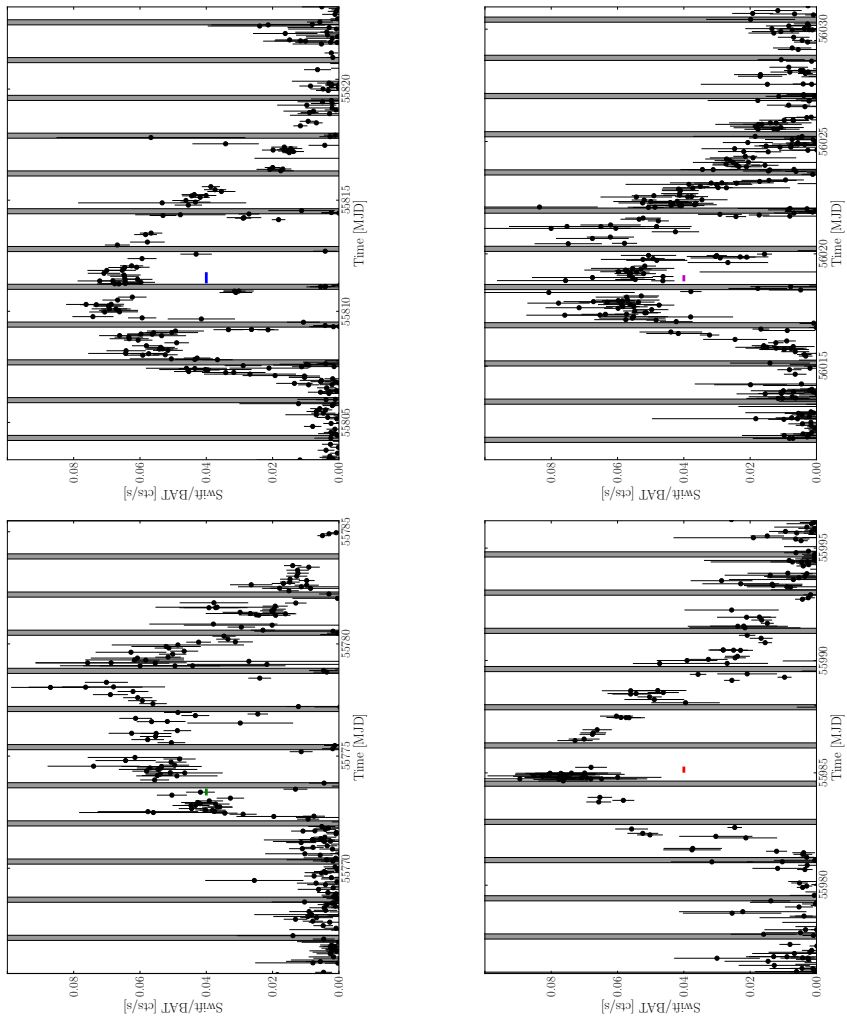


Figure 7.1: The orbital *Swift*/*BAT* light curves of the 4 main-ons listed in Table 7.1. The flux is plotted as a function of time and the duration of each *XMM* observation is marked with a horizontal bar (green - obs 05, blue - obs 06, red - obs 08, magenta - obs 09).



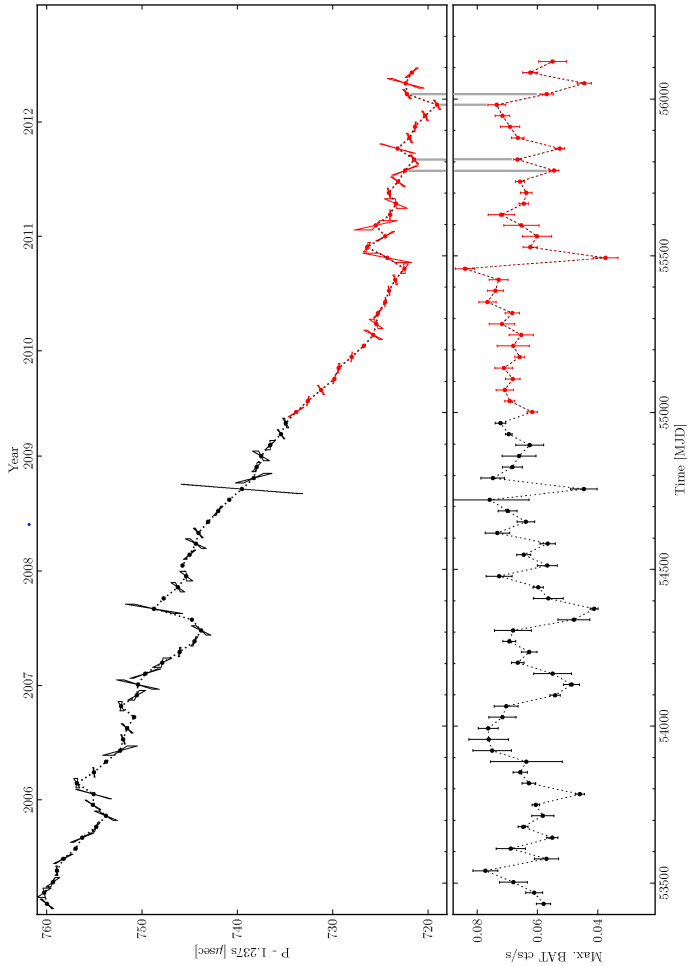


Figure 7.2: Figure is taken from Klochkov et al. (2009) with updated values from S. Gorol. Pulse period evolution of Her X-1 as measured by *Swift*/BAT. In the *upper panel*, the pulse period of each main-on state is shown. The cones illustrate the pulse period derivative and the corresponding error. In the *lower panel*, the maximum *Swift*/BAT cts/s in the respective main-on with error bars are shown. The 4 main-ons that we analyzed are marked with grey vertical lines.

Table 7.1: Four *XMM-Newton* observations during four different main-on states used in our analysis. In the following, the observations are referred to using the notation in the "reference" column.

observation	reference	revolution	MJD	exposure [ks]
0673510501	obs 05	2132	55773	15.9
0673510601	obs 06	2151	55811	32.5
0673510801	obs 08	2238	55985	12.9
0673510901	obs 09	2255	56018	13.2

and spacecraft files, and the data products from the Pipeline Processing System (PPS). For the data reduction, the Current Calibration Files (CCF) are required. Instructions are available in the *XMM-Newton* Users Handbook, the Users Guide to the *XMM-Newton* Science Analysis System or the SAS ABC-Guide that can be found on the *XMM-Newton* Science Operations Centre webpage<sup>1</sup>.

### 7.2.1 *RGS* data reduction

The *RGS* spectra were extracted using the SAS task `rgsproc`. We extracted spectra for the first and second order and used the same GTI as for the *MOS/pn* data reduction (Sec. 7.2.2) to exclude periods of high flaring particle background. The spectra were extracted in lambda space. We applied a heliocentric velocity correction that accounts for the shift of the observed wavelengths due to the motion of the satellite around the earth and of the earth around the sun. Due to electronic problems of the *RGS*, there are no data from CCD 7 (*RGS* 1) and CCD 4 (*RGS* 2).

In Figure 7.3, we show the spatial versus dispersion (displaying photon position in beta space) and energy versus dispersion (displaying photon energy versus beta angle in the dispersion direction) plots for one observation (obs 05) of *RGS* 1.

<sup>1</sup>[http://xmm.esac.esa.int/external/xmm\\_user\\_support/documentation](http://xmm.esac.esa.int/external/xmm_user_support/documentation)

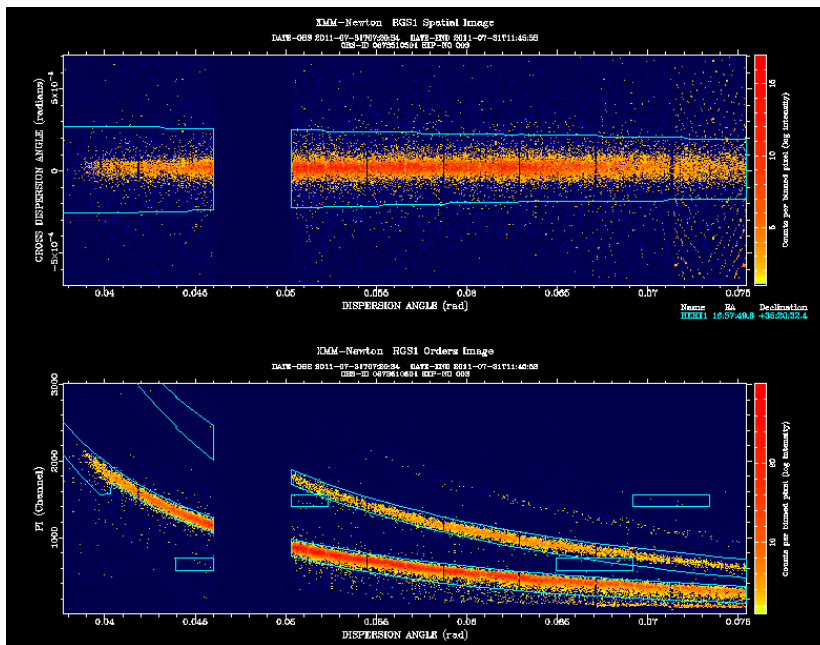


Figure 7.3: The *upper panel* shows the spatial (cross dispersion) versus dispersion (XDSP\_CORR - BETA\_CORR) image, displaying the spatial axis (y-axis) versus the dispersion in energy/wavelength (x-axis, corrected *RGS* angle, see Fig. 3.8). The *lower panel* shows the energy (pulse height) versus dispersion (PI - BETA\_CORR) image, displaying the spectral resolution of the CCD detector versus the dispersion of the spectrograph. Lower dispersion angles correspond to shorter wavelengths or higher energies. Both plots are from *RGS* 1 of obs 05. The images were produced using *rgsplot*. The plots show the spectral extraction regions (1<sup>st</sup> and 2<sup>nd</sup> order spectra) and also display the extraction regions for the calibration.

## 7.2.2 EPIC data reduction

The *MOS* detector plane is formed by an inner CCD chip that performs in timing mode and 6 outer CCDs that operate in imaging mode. Our data were taken in timing mode. That is, the central CCD which contains the source image, provides spatial information only along one dimension: the *RAWX* axis. Along the *RAWY* axis, data from a predefined area of one CCD chip is collapsed into a one dimensional row to be read out at high speed (with a maximal time resolution of  $30 \mu\text{s}$ ). According to the SAS ABC-Guide, we filtered the event files<sup>2</sup> and rejected data from intervals with high flaring particle background. For the spectral extraction, the event files were filtered<sup>3</sup> and the limits for *RAWX* were set so that the source is positioned in the middle of the selected extraction region (e.g. *left* plot of Fig. 7.4 for *MOS 2*). For the extraction of the background, we selected a source-free region from the outer CCDs (operating in imaging mode) because the timing strip is only 100 pixels wide and the inner CCD is dominated by radiation from the source. The background was then rescaled to the source region (SAS task *backscale*).

The *pn* timing mode event lists were filtered<sup>4</sup>. Data from periods of high flaring particle background were excluded. As recommended by the instrument team, we also used the task *epfast* to correct for rate-dependent effects on the energy scale. The spectra were extracted<sup>5</sup> and the *RAWX* limits were set (Fig. 7.4 *right*). The background was taken from the same CCD of a distant region from the source and scaled to the source region. We also checked for photon pile-up. For high count rates pile-up can become a problem because more than one X-ray photon can hit the detector in one camera pixel and is not read out as two (or more) events but as one event with a higher energy. Pile-up becomes important at count rates of  $\sim 800$  cts/s (for *pn*, see *XMM-Newton* user book). Our *pn* observations have mean count rates of: 455.8 cts/s (obs 05), 484.5 cts/s (obs 06), 513.6 cts/s (obs 08) and 459.6 cts/s (obs 09). We still checked for pile-up using the task *epatplot*. This task plots the relative ratios

---

<sup>2</sup>using SAS task *evselect* with following criteria of the pattern of an event characterizing e.g. if the event was distributed over more detector pixels (*PATTERN*) and pulse height/energy (*PI*):  $\text{PATTERN} \leq 12$ ,  $\text{PI} \geq 200$ ,  $\text{PI} \leq 12000$

<sup>3</sup>with *FLAG=0* to specify the event quality,  $\text{PATTERN} \leq 0$

<sup>4</sup>using *evselect* with following criteria:  $\text{PATTERN} \leq 4$ ,  $\text{PI} \geq 200$ ,  $\text{PI} \leq 15000$

<sup>5</sup>using *FLAG=0*,  $\text{PATTERN} \leq 4$

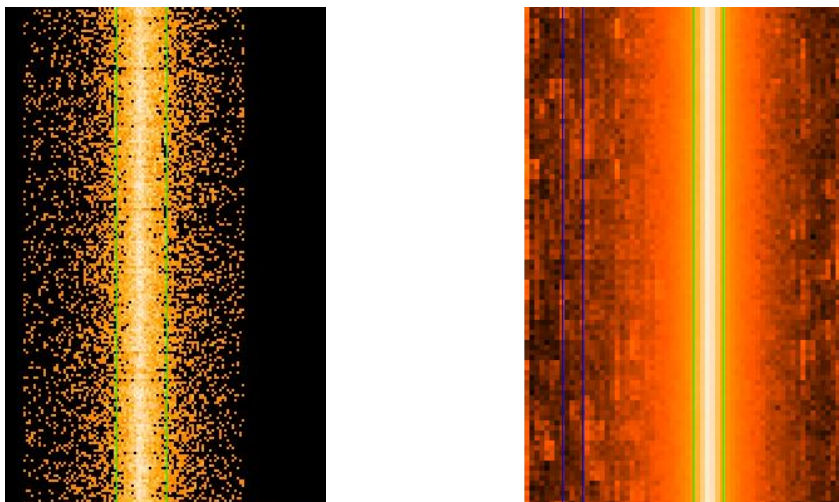


Figure 7.4: *MOS2* (left) and *pn* (right) source extraction region (green) and background extraction region (blue).

of single and double events, that one theoretically expects in the absence of pile-up and visualizes a deviation from standard values. In all four observations, we didn't find any evidence for pile-up. An example of a pattern distribution plot is shown in the appendix (Fig. A.2).

For the pulse phase resolved analysis of the *pn* spectra, we calculated pulse phases of each event in the barycentric and binary corrected event files applying the SAS task `phasecalc`. We then filtered the event lists for the selected phase intervals and performed a spectral extraction as described in the previous section.

## 7.3 Timing analysis

### 7.3.1 Light curve

We extracted *pn* light curves from the total count rates with a time resolution of 0.01 s. We then subtracted the background and corrected the photon arrival times for the motion of the satellite around the earth and

the sun (barycentric correction; SAS task `barycen`) and for the binary motion of the pulsar around his companion star (binary correction). For the binary correction we used the ephemeris from Staubert et al. (2009) (Table 6.1).

We calculated the pulse period as described in Klochkov et al. (2009), Staubert et al. (2009). First, we applied the epoch folding technique (see Sec. 5.5.1). Then, we checked the computed result of the pulse period using the pulse phase connection technique. In this technique, the light curve is split into segments that are large enough to obtain a pulse profile with good statistics. A pulse profile is produced for each of the intervals and fitted with a template profile. It is required that the pulse profiles do not change excessively within the time period of applying this method. One can then calculate the number of pulses passed in between the splitted observations. For a constant pulse period, the arrival time of the  $n$ -th pulse is

$$t_n = t_0 + nP. \quad (7.1)$$

If the pulse period changes (e.g.  $\dot{P}, \ddot{P} \neq 0$ ), this equation is modified to

$$t_n = t_0 + nP_0 + \frac{1}{2}n^2P_0\dot{P}_0 + \frac{1}{6}n^3P_0^2\ddot{P}_0 + \dots \quad (7.2)$$

with the pulse period  $P_0$  and pulse period derivatives  $\dot{P}_0, \ddot{P}_0$  at time  $t_0$  (Klochkov et al. 2009, Staubert et al. 2009). A change of the pulse period can be estimated from the (O-C) diagram. This diagram shows the *observed minus the calculated* pulse arrival times assuming a constant period. A straight line implies a constant period while a parabolic fit corresponds to a non-zero pulse period derivative.

The values of the pulse periods (Table 7.2) are in agreement with the values from *Swift/BAT* (Klochkov et al. 2009). In Figure 7.5, we show an (O-C) diagram of *XMM-pn* obs 08. For all 4 observations, we could not constrain a pulse period derivative for the time of the observations (which are quiet short). The values from *Swift/BAT* (see Figure 7.2) yield a spin-up ( $\dot{P} \sim -9.5 \times 10^{-13} \text{ ss}^{-1}$ ) during obs 05 and a spin-down ( $\dot{P} \sim 2 - 3 \times 10^{-13} \text{ ss}^{-1}$ ) during obs 06, 08, and 09.

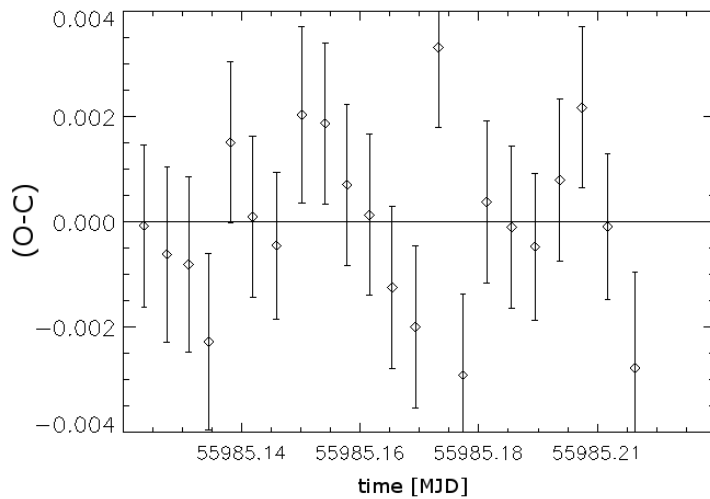


Figure 7.5: (O-C) diagram for pulse arrival times of Her X-1 measured with *XMM-pn* obs 08.

Table 7.2: Pulse period and time of phase zero ( $T_0$ ) of the *XMM-Newton* observations.

observation	period [s]	$T_0$ [MJD]
05	1.2377228	55773.0000057302
06	1.2377213	55811.0000008595
08	1.2377182	55985.0000093115
09	1.2377223	56018.0000114603

### 7.3.2 Pulse profiles

We extracted *XMM EPIC-pn* pulse profiles for following energy ranges: 0.3–0.8 keV, 0.8–1.2 keV, 1.2–2.0 keV, 2–4 keV, 4–6 keV, 6–7 keV and 7–12 keV. We extracted light curves with a time resolution of 0.01 s and applied a barycentric and binary correction to account for the motion of the satellite around the earth and the sun and for the binary motion of the system. Each light curve was folded with the pulse period from Table 7.2. The pulse profiles were produced with 64 phase bins. To select a reference phase (phase 0) for each observation, we fitted the sharp edge at the right shoulder of the main peak of the 4–6 keV pulse profile with a straight line and determined the phase value of the fitted line when crossing the level of the minimum thereafter (Staubert et al. 2009). The normalized and shifted pulse profiles are shown in Figure 7.6.

The 0.3–0.8 keV pulse profiles show a sinusoidal structure which gets more structured in the 0.8–1.2 keV band. In this energy band, we possibly observe an overlap of the soft and hard X-ray components. For energies above  $\sim 1.2$  keV, we notice a transition in the pulse profile shape. The main peak of the pulse profile shows an asymmetric double-peaked structure with a central peak (phase  $\sim 0.5$ –0.8) and a trailing shoulder (phase  $\sim 0.8$ –1.0). At phase  $\sim 0.2$  we detect an interpulse. The intensity of the trailing shoulder and the interpulse appears strongest in obs 05 (that was taken directly at the beginning of the main-on state at  $\Psi_{35} \sim 0.03$ ). This behavior is known for *Her X-1* since the intensity of the various components is found to vary during the time of a main-on (e.g. Klochko et al. 2008). This characteristic is seen also in Figure 7.7, where we show a combined image of the 4–6 keV pulse profiles of the 4 observations.

## 7.4 Spectral analysis

### 7.4.1 Phase averaged analysis

#### *RGS* spectra

*RGS* spectra of the 4 main-on observations were analyzed. We searched for changes of the intensity of the narrow X-ray emission lines that are



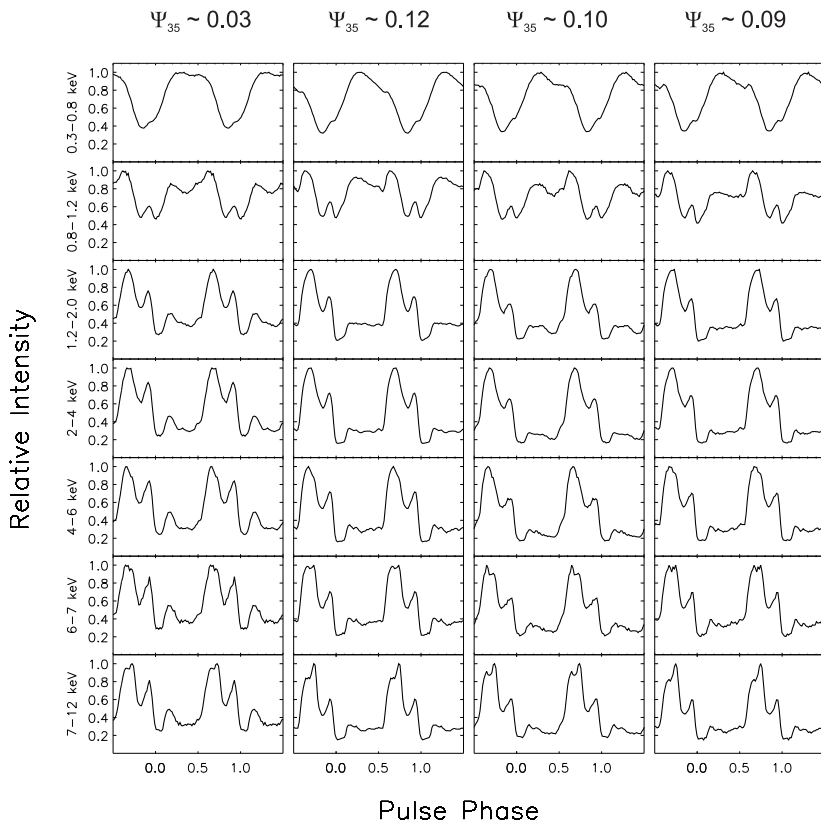


Figure 7.6: *XMM EPIC-pn* pulse profiles. The normalized flux is plotted as a function of the pulse phase. The pulse profiles are shown for different main-ons (from left to right: obs 05, 06, 08 and 09) and for different energy bands (energy is increasing from top to bottom). As a reference phase (phase 0) we selected the sharp edge at the right shoulder of the main peak of the 4–6 keV pulse profile.

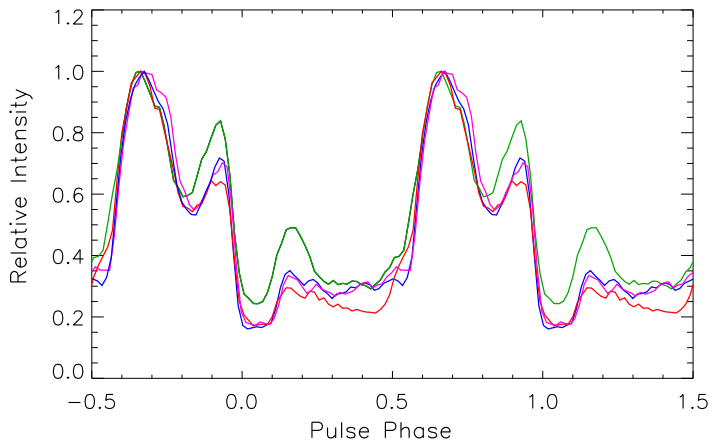


Figure 7.7: XMM EPIC-*pn* 4–6 keV pulse profiles. The normalized flux is plotted as a function of the pulse phase. The observations are labeled as following: obs 05 ( $\Psi_{35} \sim 0.03$ ) - green, obs 06 ( $\Psi_{35} \sim 0.12$ ) - blue, obs 08 ( $\Psi_{35} \sim 0.10$ ) - red, obs 09 ( $\Psi_{35} \sim 0.09$ ) - magenta.

Table 7.3: Nominal values of the observed X-ray emission lines from Jimenez-Garate et al. (2002): (i) intercombination lines; (r) resonance lines.

line	$\lambda_0$ [Å]	$E_0$ [keV]
OVIII Ly $\alpha$	18.97	0.6536
NVII Ly $\alpha$	24.78	0.5003
OVII He $\alpha$	21.80 (i)	0.5687
	21.60 (r)	0.5740
NVI He $\alpha$	29.08 (i)	0.4264

mainly present in the low and short-on state but also detected during main-ons (Jimenez-Garate et al. 2002). For the spectral analysis, we accumulated data from  $\lambda = 6 - 37 \text{ \AA}$  ( $\sim 0.35\text{--}2.05 \text{ keV}$ ) of *RGS* 1 and 2. The continuum spectra were best fitted with a power law model (`powerlaw` in *XSPEC*) and a blackbody component (`diskbb` in *XSPEC*). The continuum is modified by a broad bump at  $\sim 0.9 \text{ keV}$  that was modeled with a Gaussian emission line. The excess of emission at the OVIII Ly  $\alpha$ , NVII Ly  $\alpha$ , OVII He  $\alpha$  and NVI He  $\alpha$  energies was fitted with narrow Gaussian emission lines (see Table 7.3). In Figure 7.8, the residuals of the *RGS* spectra for obs 05 for the continuum (Fig. 7.8 a) and with the inclusion of the narrow X-ray emission lines (Fig. 7.8 b) are shown.

All line parameters were left free for fitting. In Figure 7.9, we show the fit parameters of the X-ray emission lines: line energy  $E$  (*top right*), line width  $\sigma$  (*bottom left*), relative intensity as calculated with the `cflux` command in *XSPEC* from line flux divided by total flux ( $0.5\text{--}2.0 \text{ keV}$ , *bottom right*) - and the continuum parameters (*top left*): photon index  $\Gamma$  and blackbody temperature  $T_{\text{BB}}$  as well as the pulse period derivative  $\dot{P}$  as derived from *Swift/BAT* observations (Fig. 7.2).

We analyzed one observation (obs 05) for which *Swift/BAT* yields a spin-up ( $\dot{P} \sim -9.5 \times 10^{-13} \text{ ss}^{-1}$ ) and three observations (obs 06, 08, 09) during spin-down ( $\dot{P} \sim 2 - 3 \times 10^{-13} \text{ ss}^{-1}$ ). The flux in the  $0.5\text{--}2.0 \text{ keV}$  energy band ranges between  $3.8 - 6.8 \times 10^{-10} \text{ erg s}^{-1} \text{ cm}^{-2}$  and reaches the highest value in obs 08. The photon index varies slightly between  $\sim 0.62$  and  $0.72$ . The blackbody temperature of obs 05, 06 and 09 is

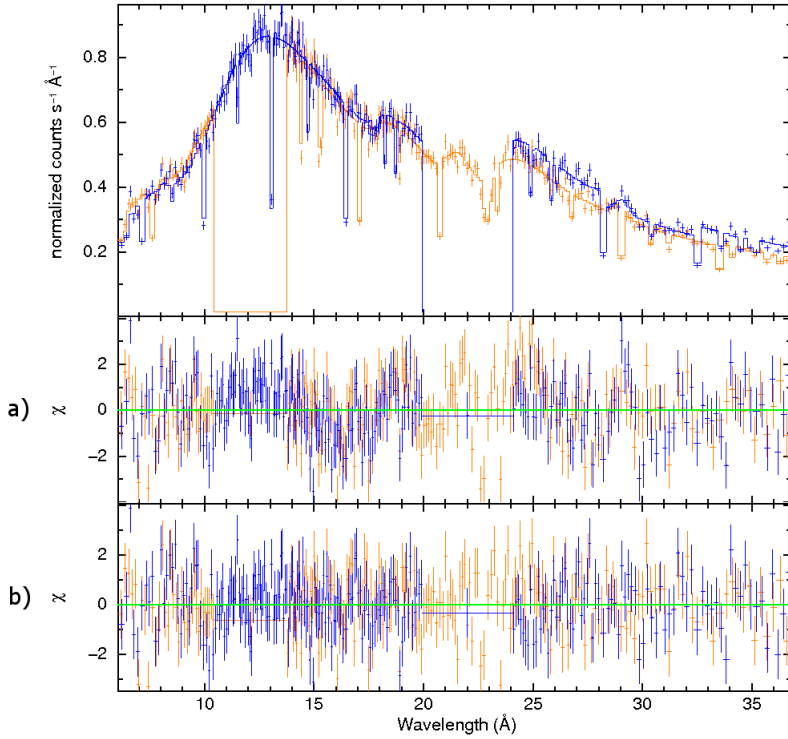


Figure 7.8: The spectra of *RGS* 1 (orange) and *RGS* 2 (blue) of obs 05 and the residuals a) without the inclusion of X-ray emission lines and b) with the inclusion of the lines.

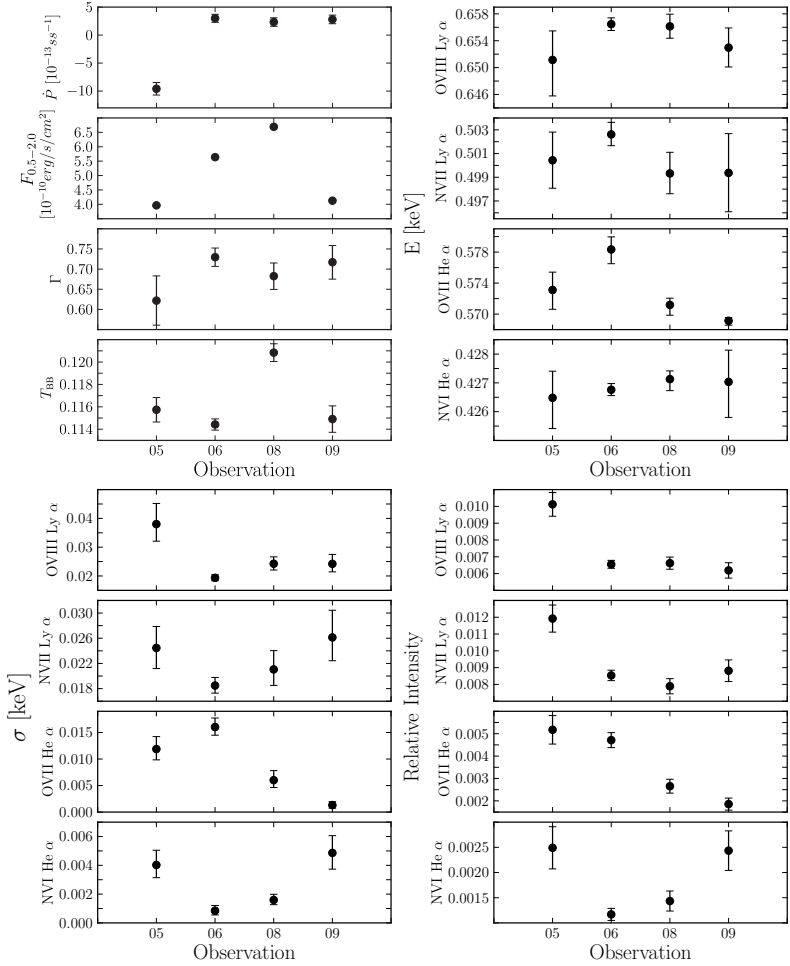


Figure 7.9: Fit parameters of the *RGS* spectra. In the panels on the *upper left* we show the pulse period derivative as derived from the *Swift*/*BAT* observations (see Fig. 7.2), the flux in the 0.5–2.0 keV energy range and the continuum parameters for the photon index  $\Gamma$  and the blackbody temperature  $T_{\text{BB}}$  of the four *XMM-Newton* observations. The other panels show the energy of the X-ray emission lines (*upper right*), the line width (*bottom left*) and the relative flux of the lines as derived with the *cflux* command in *XSPEC* (*bottom right*).

$kT_{\text{BB}} \sim 0.114\text{--}0.116\text{ keV}$ , while for obs 08 we obtained a slightly higher value ( $kT_{\text{BB}} \sim 0.122\text{ keV}$ ). The X-ray emission line parameters vary but do not show a dependence on  $\dot{P}$  or flux. The observed energies are spread around the nominal values according to Table 7.3. Except for the OVII He  $\alpha$  line of obs 06 for which we detected an offset compared to its nominal value. The line width is constrained best for obs 06 and 08. These two observations display the best statistics (again, except for OVII He  $\alpha$  line of obs 06). The relative intensity of the X-ray emission lines does not show a significant dependence on flux or  $\dot{P}$ .

### **EPIC spectra**

*EPIC-MOS* and *EPIC-pn* spectra of the 4 main-on state observations were analyzed. We studied the continuum and the iron line (see Sec. 6.3) parameters. The spectra were extracted in the energy ranges 0.3–10 keV (*EPIC-MOS*) and 0.5–10 keV (*EPIC-pn*) as recommended by the instrument team. In Figure 7.10, we show a combined spectrum of *EPIC-MOS* 1, *EPIC-MOS* 2 and *EPIC-pn* of obs 05. In the *EPIC-MOS* spectra there was no indication of an iron line component. Therefore, we limited our analysis to the *EPIC-pn* data. For the fit of the iron line, we restricted the energy range to 5–10 keV (similar to e.g. Zane et al. 2004). The very high statistics of the Her X-1 observations and the not very well calibration of the *EPIC-pn* timing mode yield high residuals in the low energy part of the spectrum (see e.g. Fig. 7.10, 7.11), thus not allowing us to fit the line in the 0.5–10 keV spectrum. The 5–10 keV spectrum still provides sufficient statistics to justify a fit of the iron line in this energy band.

The continuum spectra were best fitted with a power law, a blackbody component, a Gaussian emission line at  $\sim 0.9\text{ keV}$  and 2 (respectively 3) Gaussian emission lines at  $\sim 6.4\text{ keV}$  (i.e. the energy of the Fe K $\alpha$  emission line of a certain ionization stage). In *XSPEC*, these models are referred to as

`powerlaw:`

$$F(E) = K \times E^{-\Gamma} \quad (7.3)$$

with the photon index  $\Gamma$ , the normalization  $K$  (in

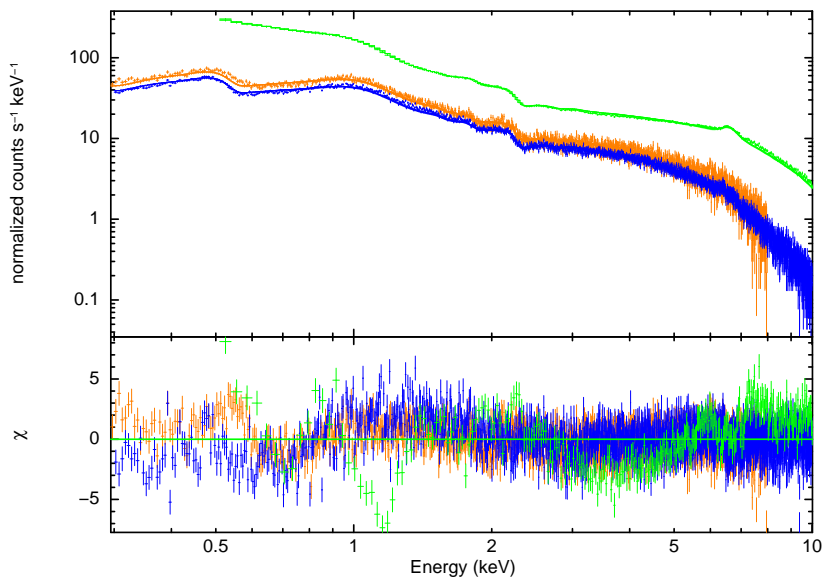


Figure 7.10: The combined *EPIC-MOS 1* (orange), *-MOS 2* (blue) and *EPIC-pn* (green) spectrum of obs 05.

photons  $\text{keV}^{-1} \text{cm}^{-2} \text{s}^{-1}$  at 1 keV),

**body:**

$$F(E) = K \times \frac{8.0525 E^2 dE}{(kT^4)(\exp(E/kT) - 1)} \quad (7.4)$$

with the temperature  $kT_{\text{BB}}$  in keV and the normalization  $K$ ,

**gauss:**

$$F(E) = K \frac{1}{\sigma\sqrt{2\pi}} \exp\left[-\frac{(E - E_0)^2}{2\sigma^2}\right] \quad (7.5)$$

with the line energy  $E_0$ , the line width  $\sigma$  and the normalization  $K$  (in photons  $\text{cm}^{-2} \text{s}^{-1}$  in the line).

The fit parameters are shown in Table 7.4. In Figure 7.11, the 0.5–10 keV EPIC-*pn* spectrum of obs 05 is shown. Figure 7.12 shows the iron line profile of all observations. To illustrate the line profiles in the residuals, we fitted the 5–10 keV spectrum and then put the iron line intensity to 0.

In Figure 7.13, the values for the flux of the different components as calculated with the `cflux` command in *XSPEC* are shown. We show the total flux ( $F_{0.5-10 \text{ keV}}$ ), the flux ( $F_{\text{BB}}$ ) and normalized flux ( $F_{\text{BB,rel}}$ ) in the blackbody component and the flux ( $F_{\text{Fe}}$ ) and normalized flux ( $F_{\text{Fe,rel}}$ ) in the iron line. The iron line flux was estimated by fitting one Gaussian line (see Table 7.5 for the fit parameters and upper two panels on the right of Fig. 7.13 for the fluxes) to allow a better comparison of the line flux, but also by fitting multiple Gaussians ( $F_{\text{Fe},1}$ ,  $F_{\text{Fe},2}$ ,  $F_{\text{Fe},3}$ , lower panels on the right of Fig. 7.13).

We analyzed 4 EPIC-*pn* main-on observations of Her X-1. For all observations we found a broad iron line ( $\sigma \sim 0.2-0.3 \text{ keV}$ ) that was best fitted with 2 (respectively 3) Gaussian lines at  $\sim 6.8$  and  $6.5 \text{ keV}$  (and  $\sim 7.2 \text{ keV}$ ). In Figure 7.14, we show the fit of the iron line with one Gaussian line, and compare it to a fit with two Gaussian lines. For the indicated observation, the  $\chi_{\text{red}}^2$  improves from 1.46 to 1.25 when fitting the line with two Gaussian components. To compare the iron line flux of the observations, we fitted the line with only one Gaussian and calculated the flux and relative flux (normalized to the total 0.5-10 keV flux) of the line. The relative flux in the iron line is higher in obs 06 and 08



Table 7.4: Fit parameters of the phase averaged spectra of the *EPIC-pn* observations obs 05, 06, 08 and 09. The errors are at  $1\sigma$  confidence level.

\*The parameters of the Gaussian lines to account for the iron emission line at around 6.4 keV were fitted for the 5–10 keV *EPIC-pn* spectra. For the evaluation of the errors, we fixed the respective other Gaussian line parameters. We then froze the values for the 0.5–10 keV fit.  $\chi^2_{\text{red},Fe}/\text{d.o.f.}$  gives the value of the 5–10 keV power law plus Gaussian line fit (with fixed Gaussian line energies and widths).

observation	$\Gamma$	$kT_{\text{BB}}$	$E_{\text{Fe},1}$ [keV]*	$\sigma_{\text{Fe},1}$ [keV]*	$\chi^2_{\text{red}}/\text{d.o.f.}$
			$E_{\text{Fe},2}$ [keV]*	$\sigma_{\text{Fe},2}$ [keV]*	$\chi^2_{\text{red},Fe}/\text{d.o.f.}$
			$E_{\text{Fe},3}$ [keV]*	$\sigma_{\text{Fe},3}$ [keV]*	
05	$0.830^{+0.002}_{-0.002}$	$0.093^{+0.002}_{-0.002}$	$6.843^{+0.018}_{-0.017}$	$0.104^{+0.030}_{-0.023}$	4.49/311
			$6.528^{+0.012}_{-0.010}$	$0.137^{+0.016}_{-0.014}$	1.32/163
06	$0.869^{+0.001}_{-0.001}$	$0.094^{+0.001}_{-0.001}$	$6.876^{+0.007}_{-0.007}$	$0.088^{+0.010}_{-0.010}$	23.45/308
			$6.553^{+0.005}_{-0.005}$	$0.137^{+0.007}_{-0.006}$	1.17/162
			$7.230^{+0.016}_{-0.018}$	$0.082^{+0.028}_{-0.027}$	
08	$0.884^{+0.002}_{-0.002}$	$0.102^{+0.002}_{-0.002}$	$6.872^{+0.019}_{-0.019}$	$0.189^{+0.028}_{-0.025}$	7.29/311
			$6.518^{+0.015}_{-0.014}$	$0.166^{+0.018}_{-0.017}$	1.30/163
09	$0.830^{+0.002}_{-0.002}$	$0.094^{+0.001}_{-0.001}$	$6.793^{+0.009}_{-0.009}$	$0.076^{+0.014}_{-0.013}$	7.87/311
			$6.511^{+0.006}_{-0.005}$	$0.071^{+0.011}_{-0.011}$	1.25/163

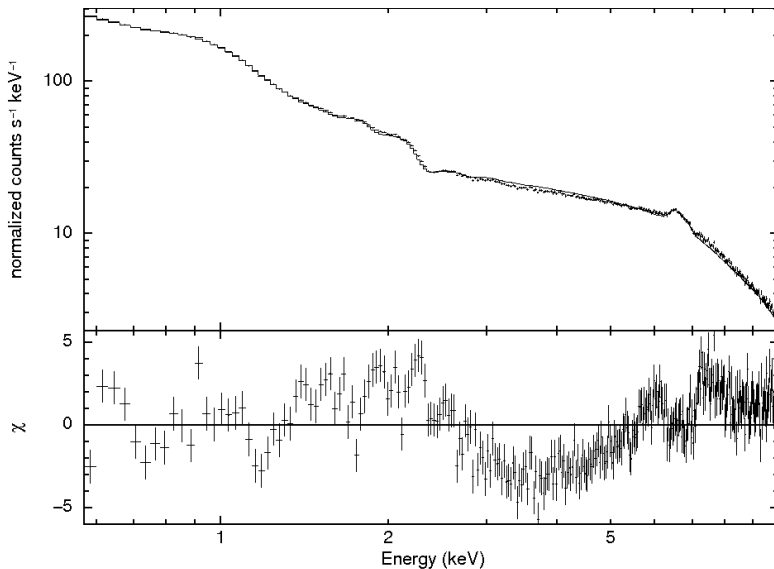


Figure 7.11: The 0.5–10 keV *EPIC-pn* spectrum of obs 05.

Table 7.5: Fit parameters of *EPIC-pn* observation obs 05, 06, 08 and 09. The spectra were fitted with a power law and one Gaussian line in the 5–10 keV energy range. The errors are at  $1\sigma$  confidence level.

obs	$E$ [keV]	$\sigma$ [keV]
05	$6.615^{+0.011}_{-0.011}$	$0.222^{+0.015}_{-0.013}$
06	$6.659^{+0.005}_{-0.006}$	$0.250^{+0.007}_{-0.007}$
08	$6.682^{+0.013}_{-0.011}$	$0.284^{+0.013}_{-0.013}$
09	$6.608^{+0.009}_{-0.010}$	$0.216^{+0.012}_{-0.012}$

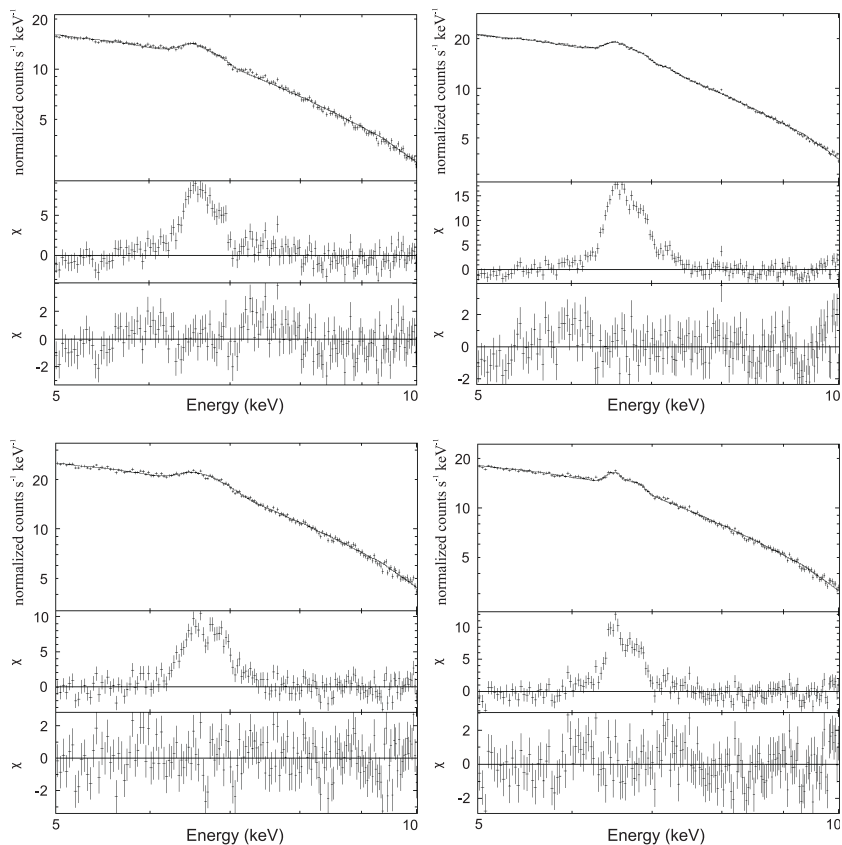


Figure 7.12: The 5–10 keV *EPIC-pn* spectra of obs 05 (*top left*), 06 (*top right*), 08 (*bottom left*) and 09 (*bottom right*). The *bottom* panels show the residuals of the fit of the iron line, the *middle* panels - the residuals from the fit with a later exclusion of the Gaussian iron line components to illustrate the shape of the line.

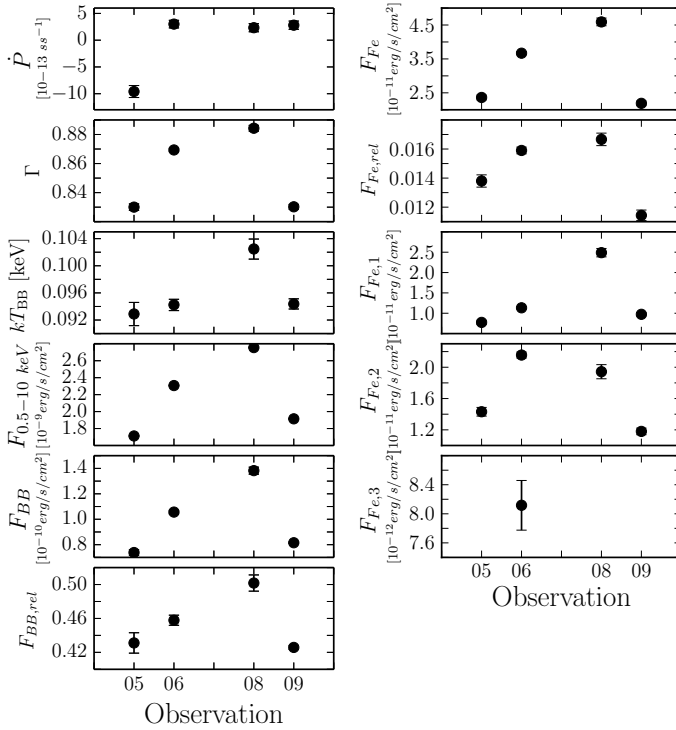


Figure 7.13: The fit parameters of the *EPIC-pn* spectra. *Left*:  $\dot{P}$  of the *Swift/BAT* observations, the photon index  $\Gamma$ , the blackbody temperature  $kT_{\text{BB}}$ , the total 0.5–10 keV flux as estimated with the `cflux` command in *XSPEC* and the flux and relative flux (normalized to the total flux) of the blackbody component. *Right*: The flux and relative flux (normalized to the total flux) in the iron line are shown. We fitted the line with only one Gaussian component for a better comparison of the line flux of the different observations. The iron line energy and width were fixed to the values reported in Table 7.5. The three panels below show the iron line flux as we fit the line with 2 (3) Gaussian components.

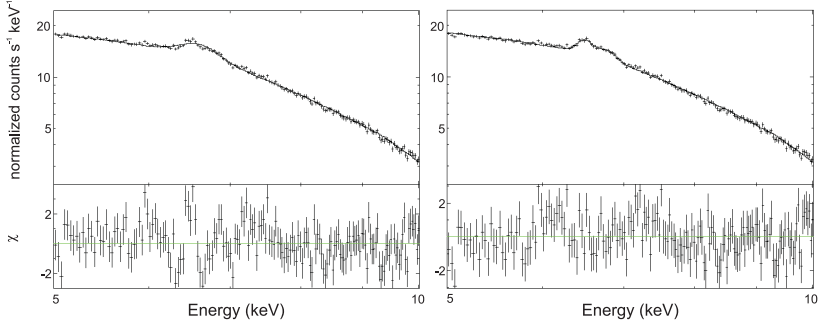


Figure 7.14: The 5–10 keV *EPIC-pn* spectra of obs 09 are shown to illustrate the shape of the iron line. In the *left* plot, the spectrum is fitted with a power law and a Gaussian line at  $\sim 6.61$  keV. The *right* plot shows the spectrum fitted with a power law and two Gaussian lines at  $\sim 6.51$  keV and  $\sim 6.79$  keV.

and considerably lower in obs 09. The photon index  $\Gamma$  ranges between  $\sim 0.83$ – $0.89$  and shows a similar variation as the total 0.5–10 keV flux. The blackbody temperature  $kT_{\text{BB}}$  and the relative flux in the blackbody component are significantly higher in obs 08. None of the parameters shows a correlation with  $\dot{P}$ .

## 7.4.2 Pulse phase resolved analysis

To analyze the spectral changes during one pulse period, we performed a pulse phase resolved analysis. We selected 60 phase bins: phase interval 0.0–0.5 is split into 20 phase bins of equal width, phase interval 0.5–1.0 - into 40 bins due to the higher flux in the second half of the pulse phase. We want to stress that this is the largest number of phase bins used for such an analysis. For the spectral analysis we extracted data from 0.5–10 keV. We fitted the spectra with the model given in Section 7.4.1 (*EPIC-pn* spectra). The iron line feature was fitted sufficiently well by the inclusion of only one Gaussian line. The blackbody temperature was fixed to the phase averaged value reported in Table 7.4. The energy and width of the Gaussian line were fixed to the values we obtained from the

pulse phase averaged analysis reported in Table 7.5.

In Figure 7.15, we show the photon index  $\Gamma$ , the flux in the blackbody component  $F_{\text{BB}}$  and the iron line flux  $F_{\text{Fe}}$ . All three parameters show a modulation with pulse phase. The photon index  $\Gamma$  shows bumps at phases  $\sim 0.05$  and  $0.3\text{--}0.35$ , a broad minimum at  $\sim 0.6$  and two deep minima at pulse phases  $\sim 0.75$  and  $\sim 0.95$ . The blackbody flux is sinusoidally modulated, reaching a minimum at pulse phase  $\sim 0.7\text{--}0.9$ , i.e. during the central peak and the trailing shoulder. The flux in the iron line component also shows a modulation with pulse phase, even though with less significance. For the two observations with the best statistics (obs 06 - blue and obs 08 - red) there appears a minimum at phase  $\sim 0.7$ . For all observations, the iron line flux is lower in phase bins  $0.8\text{--}1.0$ , i.e. during the trailing shoulder.

## 7.5 Discussion

We determined the pulse periods and energy dependent pulse profiles of 4 *EPIC-pn* observations of Her X-1. We found a pulse period (Table 7.2) in agreement with the values from *Swift/BAT* (Klochkov et al. 2009). A pulse period derivative could not be determined since the exposure time of the *XMM-Newton* observations was not sufficient (e.g. Fig. 7.5). We observe pulse profiles as a function of energy and 35 d phase that are similar to the ones reported in literature (e.g. Deeter et al. 1998, Endo et al. 2000, Ramsay et al. 2002, Staubert et al. 2013). The intensity of the interpulse appears strongest in obs 05, which was taken at the beginning of the main-on state ( $\Psi_{35} \sim 0.03$ ). This behavior is known for Her X-1 since the intensity of the various components is found to vary with 35 d phase (e.g. Klochkov et al. 2008, , Fig. 6.6). The  $0.8\text{--}1.2$  keV pulse profiles show a superposition of the soft and hard X-ray components, since both, the broad peak observed at lower energies and the double-peaked structure observed at higher energies are seen (also see Ramsay et al. 2002).

Her X-1 shows an overall spin-up trend that is interrupted by very short spin-down episodes (see Fig. 7.2). Klochkov et al. (2009) interpret this behavior with a model that expects mass ejection close to the inner parts of the accretion disk during the intense short spin-down episodes. They

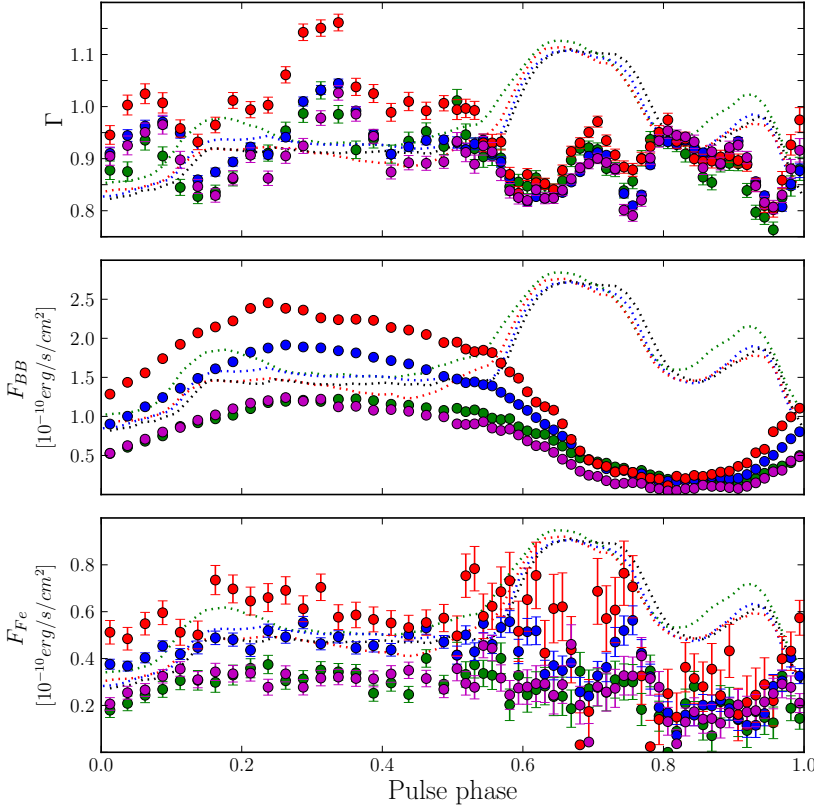


Figure 7.15: Spectral parameters as a function of pulse phase from *EPIC-pn* observations obs 05 - green, obs 06 - blue, obs 08 - red and obs 09 - magenta. The fit parameters of the photon index  $\Gamma$ , the flux in the blackbody component  $F_{BB}$  and the iron line flux  $F_{Fe}$  for 60 phase bins are shown. For each observation, the dotted lines show an averaged and normalized pulse profile ( $\sim 0.3\text{--}12$  keV) that was shifted and scaled in height for a better illustration.

assume an accretion disk that carries a magnetic field that can interact with the magnetosphere of the neutron star beyond the corotation radius. In this region, the magnetic field lines can become open (Lovelace et al. 1995) and matter escapes from the inner parts of the accretion disk along the open magnetic field lines. During these coronal wind ejections, angular momentum can be carried away from the system and a strong spin-down of the pulsar is observed.

To search for evidence of increased disk outflows during spin-down episodes, we analyzed the spectral changes in the *RGS* and *EPIC* data and compared the amount of hot, photo-ionized material in the line of sight derived from the *RGS* data in different observations. In the model of Klochkov et al. (2009), the spin-down episodes are connected to strong outflows and should therefore show a larger density of the outflowing material. In our analyses, this should be noticeable as a dependence of the intensities of the emission lines in the *RGS* spectra on the locally measured  $\dot{P}$ . We do not see a correlation between the measured  $\dot{P}$  by *Swift/BAT* and the intensity of the OVIII Ly  $\alpha$ , NVII Ly  $\alpha$ , OVII He  $\alpha$  and NVI He  $\alpha$  lines. We were actually not able to catch a good spin-down episode with our *XMM* observations (in three of them  $\dot{P}$  is around zero and in one there is a spin-up). We also could not measure a local  $\dot{P}$  from the *XMM-Newton* observations but only refer to the measured values of *Swift/BAT*. Another reason why we actually do not see a correlation can be, that we observed Her X-1 during main-on states, when the spectrum is dominated by the continuum and the significance of the lines is not very high. From our analyses, we cannot exclude the possibility of outflows during spin-down episodes or give another explanation for the strong spin-down episodes, e.g. a decrease of the mass transfer rate from the donor star. One of the main problems of this analysis was the timing of the observations. These were taken during the main-on state of the source, thus not allowing us to get good constraints on the detection of the narrow emission lines with *RGS*. To improve our results, we need to take data at different spin-down/-up episodes while the source is in a low state and the *RGS* spectra are not dominated by the continuum emission.

A change in the amount of matter around the neutron star is assumed to be connected to the width and intensity of the Fe K $\alpha$  line (see Sec. 6.3).



It is generally assumed that the iron line originates from fluorescence of cold material that is illuminated by the X-ray beam (see e.g. Ramsay et al. 2002, Vasco et al. 2013, and references therein). However, it is still not clarified where the fluorescence takes place. Proposed emission scenarios/regions are e.g. reprocessing of soft emission from cold material around the illuminated spot (Ramsay et al. 2002) or emission from an accretion disk corona, from the accretion column, the outer edge of the accretion disk or a region at the Alfvén radius (e.g. Choi et al. 1994, and references therein). It is also possible that several emission regions contribute to the total emission (e.g. Leahy 2001). The observed line broadening can originate from the emission of a complex of Fe K fluorescence lines from a variety of ionization states of Fe (from Fe I-Fe XIII to Fe XXIII), emission from the Comptonization of a range of ionized Fe states (centered around Fe XX) in a hot corona (Ramsay et al. 2002) or emission from cold material in an accretion disk wind that contributes to the Fe K $\alpha$  emission (Choi et al. 1994, Zane et al. 2004).

In our analysis of the *EPIC-pn* spectra of 4 different main-on states of Her X-1, we get results in agreement with Zane et al. (2004). We measured a broad iron line with a width of  $\sim 0.2\text{--}0.3$  keV. Fitting the Fe line with 1 Gaussian at  $\sim 6.6$  keV, the line energy and width are correlated with the total flux of the observations. The same holds for the flux in the blackbody and Fe line components, that are both correlated with the total flux (see Fig. A.3). We did not find a correlation between the fluorescent line width/intensity and the locally measured  $\dot{P}$  by *Swift/BAT*.

The pulse phase resolved analysis was done with an unprecedented resolution of 60 phase bins, i.e. corresponds to a bin size of  $\sim 1.24\text{s}/40$ , respectively  $\sim 1.24\text{s}/80$ . We found a variation of the photon index  $\Gamma$ , the Fe line intensity and the blackbody flux with pulse phase.

The flux in the blackbody component is almost sinusoidal, reaching a minimum during the main peak (phase  $\sim 0.6\text{--}1.0$ ). The flux in the iron line component is lowest during the trailing shoulder (phase  $\sim 0.8\text{--}1.0$ ) with another minimum at phase  $\sim 0.7$  in obs 06 and 08. A correlation between the intensity of the 6.4 keV iron line and the soft thermal (blackbody) flux was reported by various authors and suggests a common origin of the two components (Ramsay et al. 2002, Zane et al. 2004).

Moon & Eikenberry (2001) calculate an inner accretion disk radius of  $\sim 1 \times 10^8$  cm, proposing reprocessing of X-ray radiation from the neutron star at the inner accretion disk as a possible origin of the blackbody emission.

To estimate the region of blackbody emission, we fitted the phase averaged spectra with the `bbbodyrad` model in *XSPEC*. In this model, the normalization from the fit directly transforms to the radius of a sphere filled with blackbody emission. We calculated a radius of  $0.54 \times 10^8$  cm (e.g. obs 06) assuming a distance of 7 kpc.

Our analyses of the phase averaged and pulse phase resolved spectra suggest, that the blackbody emission (and the emission of the iron line, assuming a common origin of the two components) originates from closer to the magnetosphere ( $r_A \sim 10^8$  cm, depending on the assumed model; Boroson et al. 2000, Moon & Eikenberry 2001) than to the neutron star surface itself. The measured width of the iron line is consistent with what we expect from Keplerian motion: If we assume that the line is formed close to the inner region of the accretion disk ( $R_{\text{in}} \sim 1 \times 10^8$  cm, Moon & Eikenberry 2001), we can calculate the Doppler shift of the line energy as  $E = E_0 \left(1 + \frac{v}{c}\right)$  with  $v = \frac{2\pi R_{\text{in}}}{P}$ . For a pulse period of  $P \sim 1.2377$  s, the expected line width by Doppler broadening is  $\Delta E = 2 \times (E - E_0) \approx 2 \times 0.1 \text{ keV} = 0.2 \text{ keV}$ .

The photon index shows a strong modulation that was not detected with so many details and with such a high accuracy before. A minimum of the photon index (harder spectrum) around the main peak was reported before, as well as a smaller minimum around the left shoulder (phase  $\sim 0.6$ ) (Vasco et al. 2013). Actually, we find a much more complicated variation of  $\Gamma$  (see Fig. 7.15 in Sec. 7.4.2). The minimum of  $\Gamma$  around the main peak is split into a broader minimum at pulse phase  $\sim 0.6$  and a narrow minimum at phase  $\sim 0.75$ . Beside these two distinct minima, we find a clear minimum at phase  $\sim 0.95$  and an excess of emission at pulse phases  $\sim 0.05$  and  $0.3\text{--}0.35$ . Vasco et al. (2013) argue that the minimum of  $\Gamma$  around the main peak results from the emission of a narrow pencil beam that is emitted perpendicular to the surface of the neutron star (see also e.g. Pravdo et al. 1978, Klochkov et al. 2008). In this pulse phase, the observer looks down the accretion column closer to the neutron star

surface where the magnetic field and the temperatures are higher. This model explains the observed maximum of  $E_{\text{cyc}}$  and the minimum of  $\Gamma$  (harder spectrum) around the main peak (phase  $\sim 0.75$ ). Vasco et al. (2013) attribute the second sharp minimum at phase  $\sim 0.6$  to the emission from the second pole. We find another sharp distinct minimum at phase  $\sim 0.95$ .

Blum & Kraus (2000) provide a model that can describe the energy-dependent pulse profiles of Her X-1. Blum & Kraus (2000) applied the pulse profile decomposition method (see Sec. 5.6.4, Kraus et al. 1995) to reconstruct the geometry of the rotating neutron star and its emitting regions. As a result, the asymmetry in the pulse profiles of the source can be explained by a slightly distorted magnetic dipole field. The structure of the beam patterns is interpreted as a pencil- plus fan-beam configuration for which the relative contribution of the two components changes with energy (Blum & Kraus 1999, 2000). They find that the emission pattern can be described by a soft fan-beam component at phases  $\sim 0.15$  and  $0.45$  (at phases  $\sim 0.55$  and  $0.95$  of our pulse profiles due to another choice of phase 0) and a harder pencil-beam component at the peak of the pulse profile (phase  $\sim 0.75$  of our pulse profiles). At these pulse phases, we find minima of the photon index in our analysis. If we compare our results to the model of Blum & Kraus (2000), we can attribute the emission (and the minimum of  $\Gamma$ ) at the main peak (phase  $\sim 0.75$ ) to the emission of a hard pencil beam component of one pole, while the hardening of the spectrum (minimum of  $\Gamma$ ) at pulse phases  $\sim 0.6$  and  $\sim 0.95$  can be caused by the emission of a softer fan beam component from the second pole.

The dependence of the photon index on pulse phase can also be interpreted in the context of the work of Postnov et al. (2013). Postnov et al. (2013) computed a geometrical model of a freely precessing neutron star with a complex magnetic field configuration. This model can explain the variation of the pulse profiles with 35 d phase in Her X-1, which is related to the phase of neutron star free precession. The complex shape of the pulse profiles of Her X-1 is attributed to the emission from several emission components, i.e. several emission regions. In addition to the canonical magnetic dipole field of the neutron star (emission from the accretion onto the two magnetic poles), there form ring-like structures around the magnetic poles and transient emission regions

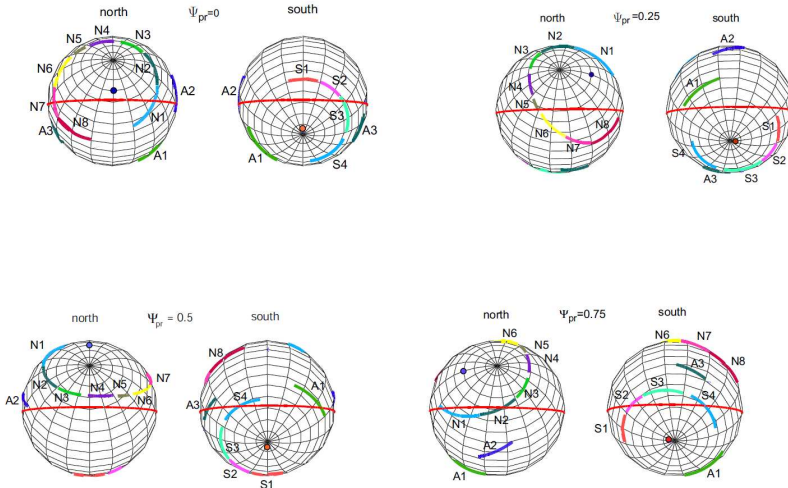


Figure 7.16: The emission regions on the surface of the neutron star Her X-1 are shown for different precession phases  $\Psi_{35}$ . The two magnetic poles are marked with red/blue circles, the ring-like emission regions around the poles in different colors. The red line indicates the projected line of sight of the observer on the neutron star surface over one spin period. The pole of the grid corresponds to the axis of inertia. The north and south hemispheres are shown. Figure is taken from Postnov et al. (2013).

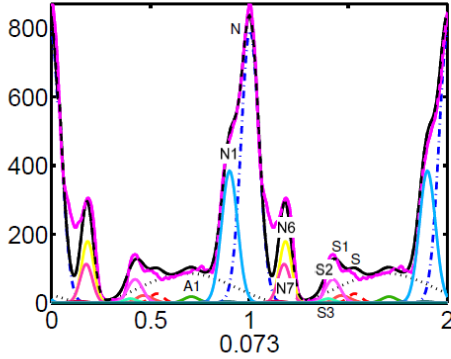


Figure 7.17: The contribution from several emission regions to the observed pulse profile (magenta) of Her X-1 is shown for precession phase  $\Psi_{35} = 0.073$ . The corresponding emission regions are indicated in Fig. 7.16. Figure is taken from Postnov et al. (2013).

(Fig. 7.16). A complex non-dipole magnetic field was already suggested before (Shakura et al. 1991, Panchenko & Postnov 1994) and confirmed by MHD simulations (Long et al. 2008, 2012). Ring-like emission structures can be formed e.g. if there exists an additional quadrupole field, aligned with the dipole field, and can become more complicated, e.g. if one magnetic pole is shifted with respect to the other from the symmetry axis. In this model, it is assumed that the emission originates from narrow X-ray beams emitted normally to the neutron star surface. In Figure 7.16, the emission regions on the surface of the neutron star Her X-1 are shown. Figure 7.17 illustrates the contribution from the emission regions to the observed pulse profile.

Our observations are taken during main-on states of the source, at precession phases  $\Psi_{35} \sim 0.03 - 0.12$ . According to the model by Postnov et al. (2013), in this precession phase, the main peak is composed of emission from the north pole ("N") and from a section of the ring around the north pole, "N1" (Fig. 7.17). The trailing shoulder is composed of the emission from regions "N6" and "N7" from the ring-like structure around "N". The interpulse is formed by emission from the south pole ("S") and

from sections of the ring-like emission structure around the south pole ("S1" and "S2"). Additionally, emission from a transient region ("A1") is observed. At the center of the emission peaks (shown in Fig. 7.17), we find (sharp) minima of the photon index, i.e. a hardening of the spectrum (see Fig. 7.15). This suggests a narrow X-ray emission beam at exactly these pulse phases, when the mentioned emission regions cross the line of sight. We encourage the idea mentioned in Vasco et al. (2013, and references therein) that the peaks in the pulse profile can be associated with narrow X-ray beams emitted from the accretion regions. The geometrical model of Postnov et al. (2013) is strongly supported by our results. We can consider the magnetic field configuration outlined above (see Fig. 7.16) as a possible scenario to explain the observed behavior of Her X-1.

# Chapter 8

## Summary and conclusions

In this work, we study the spectral and timing properties of the two accreting pulsars A 0535+26 and Her X-1. We analyzed observations from the X-ray observatories *RXTE*, *INTEGRAL* and *XMM-Newton*. The main results are summarized in the following:

### **A 0535+26**

- The dependence of the pulse profile shape on energy and luminosity is interpreted with a geometrical model of one magnetic pole passing through the observer's line of sight, whereas the second pole is never seen directly from the top but only through the gravitationally bent radiation from the lateral emission of the accretion column and its thermal scattering halo. The emission from this column forms the secondary peak. Hence, only the emission of softer photons is detected from this pole. The emission of harder photons that are produced closer to the neutron star surface can be screened by the neutron star. Thus, the intensity of the secondary peak decreases with increasing energy. The same applies for lower accretion rates: the column height decreases and the secondary peak of the pulse profile gets smaller.

- The dependence of pulsed fraction on energy and luminosity (i.e. the pulsed fraction increases with energy and decreases with luminosity) is attributed to the emission diagram changing from a more "pencil" to a more "fan" beam configuration with increasing flux.
- A hardening of the continuum with increasing flux is observed in the phase averaged, pulse phase resolved and pulse amplitude resolved analyses. An indication of a positive  $E_{\text{cyc}}$ -flux correlation is seen in some phase bins, even though with a small significance. In the phase averaged analyses, the cyclotron line centroid energy indicates some variation but does not show a correlation with the luminosity of the source.
- The maximum flux of the analyzed outburst ( $\sim 1$ Crab) suggests that A 0535+26 accretes in a sub-critical accretion regime during that outburst. If we assume that A 0535+26 operates in a similar accretion regime as the other sub-critical sources, Her X-1 and GX 304-1, the positive  $E_{\text{cyc}}$ -flux correlation might be smeared due to a special orientation of the system with respect to the observer's line of sight and/or a special geometry of the emitting structure. Otherwise, A 0535+26 could represent another accretion regime, in which the height of the emitting region does not change significantly in the observed range of luminosities. Compared to the other sub-critical sources, the luminosity of A 0535+26 is far below the respective  $L_{\text{crit}}$ , hence, the accretion geometry of A 0535+26 might indeed be different.
- The pulse phase resolved analysis yields a variation of the photon index  $\Gamma$  and the cyclotron line energy  $E_{\text{cyc}}$  with pulse phase and with luminosity at individual pulse phases. The main peak has a slightly harder spectrum, compared to the secondary peak. This is attributed to harder photons originating in the polar caps and escaping the accretion column from the top along the magnetic field lines. The variation of  $E_{\text{cyc}}$  with pulse phase can be caused by the changing viewing angles on the scattering region and by the dependence of the magnetic scattering cross sections on the angle between the magnetic field and the line of sight.  $E_{\text{cyc}}$



shows a marginal indication for a positive correlation with flux during the secondary peak of the pulse profile. The secondary peak is caused by the emission perpendicular to the accretion column(s) axis/magnetic field lines. At these inclinations, when the radiation is emitted nearly perpendicular to the local magnetic field, the CRSFs are expected to be deeper and narrower. Therefore, the viewing angle might support the detection of an  $E_{\text{cyc}}$ -flux correlation in this pulse phase.

- Contrary to the pulse phase averaged studies, the pulse amplitude resolved analysis reveals a hardening of the power law (decrease of  $\Gamma$ ) and a positive  $E_{\text{cyc}}$ -pulse amplitude correlation. The (non-)detection of an  $E_{\text{cyc}}$ -flux correlation in the pulse phase averaged analysis is attributed to a relatively broad distribution of individual pulse amplitudes due to a strong pulse-to-pulse variability of A 0535+26. The pulse phase averaged spectra are accumulated over longer time scales, thus, containing the contributions by pulses with different amplitudes. This variability might lead to a considerable smearing effect, suppressing the effect of a possible  $E_{\text{cyc}}$ -flux variation in the pulse phase averaged analysis.

## Her X-1

- The pulse period behavior of Her X-1 can be interpreted with a model that expects mass ejection close to the inner parts of the accretion disk during the intense short spin-down episodes. We analyzed the spectral changes in the *RGS* and *EPIC* data. We compared the amount of hot, photo-ionized material in the line of sight derived from the *RGS* data in different observations but did not find a correlation between the measured  $\dot{P}$  by *Swift/BAT* and the intensity of the OVIII Ly  $\alpha$ , NVII Ly  $\alpha$ , OVII He  $\alpha$  and NVI He  $\alpha$  lines. We also did not find a correlation between the iron fluorescence line width/intensity and the local measured  $\dot{P}$  by *Swift/BAT*, which could indicate a change in the amount of matter around the neutron star. We were actually not able to catch a good

spin-down episode with our *XMM* observations. We also could not measure a local  $\dot{P}$  from the *XMM-Newton* observations but only refer to the measured values of *Swift/BAT*. From our analyses, we cannot exclude the possibility of outflows during spin-down episodes or give another explanation for the strong spin-down episodes, e.g. a decrease of the mass transfer rate from the donor star. The main problem of this analysis lies in the timing of the observations. These were taken during the main-on state of the source, thus when the *RGS* spectrum is dominated by the continuum emission and the significance of the narrow emission lines is not very high. To improve our results, we need data taken at different spin-down/-up episodes while the source is in a low state.

- It is generally assumed that the iron line originates from fluorescence of cold material that is illuminated by the X-ray beam but still not clarified where the fluorescence takes place. We measured a broad iron line with a width of  $\sim 0.2\text{--}0.3$  keV. This width is consistent with what we expect from Keplerian motion, assuming an inner disk radius of  $\sim 1 \times 10^8$  cm. We estimated the region of blackbody emission (and the emission of the iron line, assuming a common origin of the two components). We find that the blackbody and iron line emission originates from a region closer to the magnetosphere than to the neutron star surface itself.
- The pulse phase resolved analysis was done with an unprecedented resolution of 60 phase bins. All spectral parameters show a strong variation with pulse phase, particularly at the peaks of the pulse profile.
- The modulation of the photon index was not detected with so many details and with such a high accuracy before. We encourage the idea that the peaks in the pulse profile can be associated with narrow X-ray beams emitted from the accretion regions. The dependence of the photon index on pulse phase can be attributed to the emission from multiple emission regions.





# Bibliography

- Acciari, V. A., Aliu, E., Araya, M., et al. 2011, *ApJ*, 733, 96
- Arnaud, K. A. 1996, *Astronomical Society of the Pacific Conference Series*, 101, 17
- Baade, W., & Zwicky, F. 1934a, *Phys. Rev.*, 45, 138
- Baade, W., & Zwicky, F. 1934b, *Proceedings of the National Academy of Science*, 20, 254
- Bahcall, J. N., & Bahcall, N. A. 1972, *Astronomy Letters*, 178, L1
- Barnstedt, J., Staubert, R., Santangelo, A., et al. 2008, *A&A*, 486, 293
- Basko, M. M., & Sunyaev, R. A. 1976a, *Soviet Astronomy Letters*, 20, 537
- Basko, M. M., & Sunyaev, R. A. 1976b, *MNRAS*, 175, 395
- Becker, P. A., & Wolff, M. T. 2005, *Astronomy Letters*, 621, L45
- Becker, P. A., & Wolff, M. T. 2007, *ApJ*, 654, 435
- Becker, P. A., Klochikov, D., Schönherr, G., et al. 2012, *A&A*, 544, A123
- Blondin, J. M., Kallman, T. R., Fryxell, B. A., et al. 1990, *ApJ*, 356, 591
- Blum, S., & Kraus, U. 1999, in *Highlights in X-ray Astronomy*, ed. B. Aschenbach & M. J. Freyberg, 29
- Blum, S., & Kraus, U. 2000, *ApJ*, 529, 968

- Boella, G., Butler, R. C., Perola, G. C., et al. 1997, *A&AS*, 122, 299
- Bondi, H. 1952, *MNRAS*, 112, 195
- Bondi, H., & Hoyle, F. 1944, *MNRAS*, 104, 273
- Borkus, V. V., Kaniovsky, A. S., Sunyaev, R. A., et al. 1998, *Astronomy Letters*, 24, 350
- Boroson, B., Kallman, T., & Vrtillek, S. D. 2001, *ApJ*, 562, 925
- Boroson, B., O'Brien, K., Horne, K., et al. 2000, *ApJ*, 545, 399
- Boyd, P., Still, M., & Corbet, R. 2004, *The Astronomer's Telegram*, 307, 1
- Boynton, P. E., Deeter, J. E., Lamb, F. K., et al. 1986, *ApJ*, 307, 545
- Boynton, P. E., Deeter, J. E., Lamb, F. K., et al. 1984, *Astronomy Letters*, 283, L53
- Bradt, H., Mayer, W., Buff, J., et al. 1976, *Astronomy Letters*, 204, L67
- Bradt, H. V., Rothschild, R. E., & Swank, J. H. 1993, *A&AS*, 97, 355
- Caballero, I. 2009, PhD thesis, IAAT University of Tuebingen
- Caballero, I., Kraus, U., Santangelo, A., et al. 2011a, *A&A*, 526, A131
- Caballero, I., & Wilms, J. 2012, *MmSAI*, 83, 230
- Caballero, I., Kretschmar, P., Santangelo, A., et al. 2007, *A&A*, 465, L21
- Caballero, I., Santangelo, A., Kretschmar, P., et al. 2008, *A&A*, 480, L17
- Caballero, I., Kretschmar, P., Pottschmidt, K., et al. 2009, *The Astronomer's Telegram*, 2337, 1
- Caballero, I., Santangelo, A., Pottschmidt, K., et al. 2010a, *The Astronomer's Telegram*, 2541, 1
- Caballero, I., Pottschmidt, K., Barragan, L., et al. 2010b, *ArXiv e-prints*

- Caballero, I., Pottschmidt, K., Santangelo, A., et al. 2010c, in Eighth Integral Workshop
- Caballero, I., Ferrigno, C., Klochkov, D., et al. 2011b, *The Astronomer's Telegram*, 3204, 1
- Caballero, I., Pottschmidt, K., Santangelo, A., et al. 2011c, ArXiv e-prints
- Caballero, I., Müller, S., Bordas, P., et al. 2012, *American Institute of Physics Conference Series*, 1427, 300
- Caballero, I., Pottschmidt, K., Marcu, D. M., et al. 2013, *Astronomy Letters*, 764, L23
- Camero-Arranz, A., Finger, M. H., Wilson-Hodge, C., et al. 2011, *The Astronomer's Telegram*, 3166, 1
- Camero-Arranz, A., Finger, M. H., Wilson-Hodge, C. A., et al. 2012, *ApJ*, 754, 20
- Carrier, F., Barblan, F., Burki, G., et al. 2003, *A&A*, 398, 1073
- Chandrasekhar, S. 1931, *ApJ*, 74, 81
- Chandrasekhar, S. 1935, *MNRAS*, 95, 207
- Chartres, M., & Li, F. 1977, *IAU Circ.*, 3154, 2
- Cheng, F. H., Vrtilik, S. D., & Raymond, J. C. 1995, *ApJ*, 452, 825
- Choi, C. S., Nagase, F., Makino, F., et al. 1994, *ApJ*, 437, 449
- Crampton, D. 1974, *ApJ*, 187, 345
- Crosa, L., & Boynton, P. E. 1980, *ApJ*, 235, 999
- dal Fiume, D., Orlandini, M., Cusumano, G., et al. 1998, , 329, L41
- Daugherty, J. K., & Harding, A. K. 1986, *ApJ*, 309, 362
- Davidson, K., & Ostriker, J. P. 1973, *ApJ*, 179, 585
- Deeter, J. E., & Boynton, P. E. 1976, *Astronomy Letters*, 210, L133

- Deeter, J. E., Boynton, P. E., Lamb, F. K., et al. 1989, *ApJ*, 336, 376
- Deeter, J. E., Boynton, P. E., Miyamoto, S., et al. 1991, *ApJ*, 383, 324
- Deeter, J. E., Scott, D. M., Boynton, P. E., et al. 1998, *ApJ*, 502, 802
- Demmel, V., Morfill, G., & Atmanspacher, H. 1990, *ApJ*, 354, 616
- den Herder, J. W., Brinkman, A. C., Kahn, S. M., et al. 2001, *A&A*, 365, L7
- Dennerl, K. 1991, NASA STI/Recon Technical Report N, 93, 28202
- Doroshenko, V., Santangelo, A., Doroshenko, R., et al. 2014, *A&A*, 561, A96
- Doxsey, R., Bradt, H. V., Levine, A., et al. 1973, *Astronomy Letters*, 182, L25
- Elsner, R. F., & Lamb, F. K. 1977, *ApJ*, 215, 897
- Endo, T., Nagase, F., & Mihara, T. 2000, *PASJ*, 52, 223
- Ferrigno, C., Falanga, M., Bozzo, E., et al. 2011, *A&A*, 532, A76
- Ferrigno, C., Segreto, A., Santangelo, A., et al. 2007, *A&A*, 462, 995
- Finger, M. H., Camero-Arranz, A., Kretschmar, P., et al. 2006, *Bulletin of the American Astronomical Society*, 38, 359
- Finger, M. H., Wilson, R. B., & Hagedon, K. S. 1994a, *IAU Circ.*, 5931, 1
- Finger, M. H., Wilson, R. B., & Harmon, B. A. 1994b, *IAU Circ.*, 5934, 1
- Finger, M. H., Wilson, R. B., & Harmon, B. A. 1996, *ApJ*, 459, 288
- Forman, W., Jones, C., Cominsky, L., et al. 1978, *ApJs*, 38, 357
- Forman, W., Jones, C. A., & Liller, W. 1972, *Astronomy Letters*, 177, L103
- Frank, J., King, A. R., & Raine, D. J. 1985, *Science*, 230, 1269



- Frontera, F., dal Fiume, D., Morelli, E., et al. 1985, *ApJ*, 298, 585
- Fürst, F., Pottschmidt, K., Wilms, J., et al. 2014, *ApJ*, 780, 133
- Gehrels, N., Chincarini, G., Giommi, P., et al. 2005, *ApJ*, 621, 558
- Gerend, D., & Boynton, P. E. 1976, *ApJ*, 209, 562
- Ghosh, P., & Lamb, F. K. 1978, *Astronomy Letters*, 223, L83
- Ghosh, P., & Lamb, F. K. 1979a, *ApJ*, 232, 259
- Ghosh, P., & Lamb, F. K. 1979b, *ApJ*, 234, 296
- Giacconi, R., Gursky, H., Kellogg, E., et al. 1973, *ApJ*, 184, 227
- Giacconi, R., Gursky, H., Kellogg, E., et al. 1971a, *Astronomy Letters*, 167, L67
- Giacconi, R., Gursky, H., Paolini, F. R., et al. 1962, *Physical Review Letters*, 9, 439
- Giacconi, R., Gursky, H., & Waters, J. R. 1964, *Nature*, 204, 981
- Giacconi, R., Kellogg, E., Gorenstein, P., et al. 1971b, *Astronomy Letters*, 165, L27
- Giacconi, R., Murray, S., Gursky, H., et al. 1972, *ApJ*, 178, 281
- Giacconi, R., Branduardi, G., Briel, U., et al. 1979, *ApJ*, 230, 540
- Giangrande, A., Giovannelli, F., Bartolini, C., et al. 1980, *A&AS*, 40, 289
- Giovannelli, F., & Graziati, L. S. 1992, *Space Science Reviews*, 59, 1
- Grimm, H.-J., Gilfanov, M., & Sunyaev, R. 2002, *A&A*, 391, 923
- Gruber, D. E., Blanco, P. R., Heindl, W. A., et al. 1996, *A&AS*, 120, C641+
- Hanuschik, R. W. 1996, *A&A*, 308, 170
- Harding, A. K., & Daugherty, J. K. 1991, *ApJ*, 374, 687

- Harding, A. K., & Lai, D. 2006, *Reports on Progress in Physics*, 69, 2631
- Henrichs, H. F. 1983, in *Accretion-Driven Stellar X-ray Sources*, ed. W. H. G. Lewin & E. P. J. van den Heuvel, 393–429
- Hewish, A., Bell, S. J., Pilkington, J. D. H., et al. 1968, *Nature*, 217, 709
- Howarth, I. D., & Wilson, B. 1983, *MNRAS*, 202, 347
- Hoyle, F., & Lyttleton, R. A. 1941, *MNRAS*, 101, 227
- Hutchings, J. B., Bernard, J. E., Crampton, D., et al. 1978, *ApJ*, 223, 530
- Ikhsanov, N. R. 2001, *A&A*, 367, 549
- Illarionov, A. F., & Sunyaev, R. A. 1975, *A&A*, 39, 185
- Jahoda, K., Swank, J. H., Giles, A. B., et al. 1996, *SPIE Conference Series*, 2808, 59
- Jansen, F., Lumb, D., Altieri, B., et al. 2001, *A&A*, 365, L1
- Ji, L., Schulz, N., Nowak, M., et al. 2009, *ApJ*, 700, 977
- Jimenez-Garate, M. A., Hailey, C. J., den Herder, J. W., et al. 2002, *ApJ*, 578, 391
- Jones, C., & Forman, W. 1976, *Astronomy Letters*, 209, L131
- Joss, P. C., & Rappaport, S. A. 1984, *Ann. Rev. A&A*, 22, 537
- Kasagi, J., Yoshida, K., Murakami, T., et al. 1986, *Phys. Rev. A*, 34, 2480
- Katz, J. I. 1973, *Nature Physical Science*, 246, 87
- Kellogg, E. M. 1975, *ApJ*, 197, 689
- Kendziorra, E., Kretschmar, P., Pan, H. C., et al. 1994, *A&A*, 291, L31
- Kiraly, P., & Meszaros, P. 1988, *ApJ*, 333, 719
- Klochkov, D. 2007, PhD thesis, IAAT University of Tuebingen
- Klochkov, D., Staubert, R., Postnov, K., et al. 2009, *A&A*, 506, 1261

- Klochkov, D., Staubert, R., Santangelo, A., et al. 2011, *A&A*, 532, A126
- Klochkov, D., Staubert, R., Postnov, K., et al. 2008, *A&A*, 482, 907
- Klochkov, D., Doroshenko, V., Santangelo, A., et al. 2012, *A&A*, 542, L28
- Kraus, U., Nollert, H.-P., Ruder, H., et al. 1995, *ApJ*, 450, 763
- Kretschmar, P. 2006, PhD thesis, IAAT University of Tuebingen
- Krimm, H. A., Barthelmy, S. D., Baumgartner, W., et al. 2009, *The Astronomer's Telegram*, 2336, 1
- Kunz, M., Kendziorra, E., Kretschmar, P., et al. 1996, *A&AS*, 120, C233
- Labanti, C., Di Cocco, G., Ferro, G., et al. 2003, *A&A*, 411, L149
- Lamb, F. K. 1988, *Timing Neutron Stars*, 649
- Lamb, F. K., & Pethick, C. J. 1974, in *Astrophysics and Gravitation*, 135–141
- Lamb, F. K., Pethick, C. J., & Pines, D. 1973, *ApJ*, 184, 271
- Lamb, R. C., Cawley, M. F., Fegan, D. J., et al. 1988, *Astronomy Letters*, 328, L13
- Lamers, H. J. G. L. M., van den Heuvel, E. P. J., & Petterson, J. A. 1976, *A&A*, 49, 327
- Landau, L. D. 1932, *Phys. Abh. Sov. Union*, 1, 285
- Leahy, D. A. 2001, in *International Cosmic Ray Conference*, Vol. 6, *International Cosmic Ray Conference*, 2536
- Lebrun, F., Leray, J. P., Lavocat, P., et al. 2003, *A&A*, 411, L141
- Levine, A. M., Bradt, H., Cui, W., et al. 1996, *Astronomy Letters*, 469, L33
- Lewin, W. H. G., van Paradijs, J., & Taam, R. E. 1993, *Space Science Reviews*, 62, 223

- Lewin, W. H. G., van Paradijs, J., & van den Heuvel, E. P. J. 1995, Cambridge Astrophysics Series, 26
- Li, F., Clark, G. W., Jernigan, J. G., et al. 1979, *ApJ*, 228, 893
- Liller, W. 1972, *IAU Circ.*, 2415, 1
- Long, M., Romanova, M. M., & Lamb, F. K. 2012, *New Astronomy*, 17, 232
- Long, M., Romanova, M. M., & Lovelace, R. V. E. 2008, *MNRAS*, 386, 1274
- Lovelace, R. V. E., Romanova, M. M., & Bisnovatyi-Kogan, G. S. 1995, *MNRAS*, 275, 244
- Lund, N., Budtz-Jørgensen, C., Westergaard, N. J., et al. 2003, *A&A*, 411, L231
- Lutovinov, A., & Tsygankov, S. 2008, American Institute of Physics Conference Series, 1054, 191
- Lutovinov, A. A., Grebenev, S. A., Pavlinsky, M. N., et al. 2000, *Astronomy Letters*, 26, 691
- Maisack, M., Grove, J. E., Kendziorra, E., et al. 1997, *A&A*, 325, 212
- Maisack, M., Grove, J. E., Johnson, W. N., et al. 1996, *A&AS*, 120, C179
- Makino, F., Cook, W., Grunsfeld, J., et al. 1989, *IAU Circ.*, 4769, 1
- Mas-Hesse, J. M., Giménez, A., Culhane, J. L., et al. 2003, *A&A*, 411, L261
- Mason, K. O., Breeveld, A., Much, R., et al. 2001, *A&A*, 365, L36
- Matsuoka, M., Kawasaki, K., Ueno, S., et al. 2009, *PASJ*, 61, 999
- McCray, R. A., Shull, J. M., Boynton, P. E., et al. 1982, *ApJ*, 262, 301
- Meszáros, P. 1984, *Space Science Reviews*, 38, 325
- Mészáros, P. 1992, High-energy radiation from magnetized neutron stars.

- Mihara, T., Soong, Y., & ASCA Team. 1994, in *New Horizon of X-Ray Astronomy. First Results from ASCA*, ed. F. Makino & T. Ohashi, 419
- Mitsuda, K.,Kunieda, H.,Inoue, H., et al. 2004, *SPIE Conference Series*, 5488, 177
- Moon, D.-S., & Eikenberry, S. S. 2001, *Astronomy Letters*, 552, L135
- Morfill, G. E.,Trümper, J.,Tenorio-Tagle, G., et al. 1984, *A&A*, 139, 7
- Motch, C.,Stella, L.,Janot-Pacheco, E., et al. 1991, *ApJ*, 369, 490
- Mowlavi, N.,Kreykenbohm, I.,Shaw, S. E., et al. 2006, *A&A*, 451, 187
- Müller, D.,Klochkov, D.,Caballero, I., et al. 2013a, *A&A*, 552, A81
- Müller, S.,Ferrigno, C.,Kühnel, M., et al. 2013b, *A&A*, 551, A6
- Mushtukov, A. A.,Suleimanov, V. F.,Tsygankov, S. S., et al. 2014, *ArXiv e-prints*
- Nagase, F. 1989, *PASJ*, 41, 1
- Nagase, F.,Corbet, R. H. D.,Day, C. S. R., et al. 1992, *ApJ*, 396, 147
- Nagase, F.,Hayakawa, S.,Kunieda, H., et al. 1982, *ApJ*, 263, 814
- Nagel, W. 1981, *ApJ*, 251, 288
- Naik, S.,Dotani, T.,Terada, Y., et al. 2008, *ApJ*, 672, 516
- Negueruela, I. 2004, *ArXiv Astrophysics e-prints*
- Oppenheimer, J. R., & Volkoff, G. M. 1939, *Physical Review*, 55, 374
- Ostriker, J. P., & Davidson, K. 1973, *IAU Symposium*, 55, 143
- Panchenko, I. E., & Postnov, K. A. 1994, *A&A*, 286, 497
- Parmar, A. N.,Oosterbroek, T.,dal Fiume, D., et al. 1999, *A&A*, 350, L5
- Parmar, A. N.,Pietsch, W.,McKechnie, S., et al. 1985, *Nature*, 313, 119
- Petterson, J. A. 1975, *Astronomy Letters*, 201, L61

- Petterson, J. A. 1977, *ApJ*, 218, 783
- Porter, J. M., & Rivinius, T. 2003, *PASP*, 115, 1153
- Postnov, K., Shakura, N., Staubert, R., et al. 2013, *MNRAS*, 435, 1147
- Pottschmidt, K., Rothschild, R. E., Gasaway, T., et al. 2006, *Bulletin of the American Astronomical Society*, 38, 384
- Pottschmidt, K., Suchy, S., Rivers, E., et al. 2012, *American Institute of Physics Conference Series*, 1427, 60
- Poutanen, J., Mushtukov, A. A., Suleimanov, V. F., et al. 2013, *ApJ*, 777, 115
- Pravdo, S. H., Bussard, R. W., Becker, R. H., et al. 1978, *ApJ*, 225, 988
- Pravdo, S. H., Bussard, R. W., & White, N. E. 1979, *MNRAS*, 188, 5P
- Priedhorsky, W. C., & Terrell, J. 1983, *Nature*, 303, 681
- Pringle, J. E. 1981, *Ann. Rev. A&A*, 19, 137
- Pringle, J. E., & Rees, M. J. 1972, *A&A*, 21, 1
- Ramsay, G., Zane, S., Jimenez-Garate, M. A., et al. 2002, *MNRAS*, 337, 1185
- Reig, P. 2011, *Ap&SS*, 332, 1
- Revnivtsev, M., Churazov, E., Postnov, K., et al. 2009, *A&A*, 507, 1211
- Reynolds, A. P., Quaintrell, H., Still, M. D., et al. 1997, *MNRAS*, 288, 43
- Ricker, G. R., Scheepmaker, A., Ballintine, J. E., et al. 1976, *Astronomy Letters*, 204, L73
- Ricketts, M. J., Turner, M. J. L., Page, C. G., et al. 1975, *Nature*, 256, 631
- Ritz, S. M., Michelson, P. F., Meegan, C., et al. 2006, *Bulletin of the American Astronomical Society*, 38, 153.01
- Roche, E. A. 1873, *constitution et lorigine du systme solaire*

- Rosenberg, F. D., Eyles, C. J., Skinner, G. K., et al. 1975, *Nature*, 256, 628
- Rothschild, R., Markowitz, A., Hemphill, P., et al. 2013, ArXiv e-prints
- Rothschild, R. E., Markowitz, A., Rivers, E., et al. 2011, *ApJ*, 733, 23
- Rothschild, R. E., Blanco, P. R., Gruber, D. E., et al. 1998, *ApJ*, 496, 538
- Rothschild, R. E., Wilms, J., Tomsick, J., et al. 2006, *ApJ*, 641, 801
- Schandl, S., & Meyer, F. 1994, *A&A*, 289, 149
- Schönherr, G., Wilms, J., Kretschmar, P., et al. 2007, *A&A*, 472, 353
- Schreier, E., Levinson, R., Gursky, H., et al. 1972, *Astronomy Letters*, 172, L79
- Scott, D. M., & Leahy, D. A. 1999, , 510, 974
- Scott, D. M., Leahy, D. A., & Wilson, R. B. 2000, *ApJ*, 539, 392
- Sembay, S., Schwartz, R. A., Orwig, L. E., et al. 1990, *ApJ*, 351, 675
- Shakura, N. I., Postnov, K. A., & Prokhorov, M. E. 1991, *Soviet Astronomy Letters*, 17, 339
- Shakura, N. I., Prokhorov, M. E., Postnov, K. A., et al. 1999, *A&A*, 348, 917
- Shakura, N. I., & Sunyaev, R. A. 1973, *A&A*, 24, 337
- Slettebak, A. 1988, *PASP*, 100, 770
- Soong, Y., Gruber, D. E., Peterson, L. E., et al. 1990, *ApJ*, 348, 641
- Staubert, R., Kendziorra, E., Pietsch, W., et al. 1980, *ApJ*, 239, 1010
- Staubert, R., Klochkov, D., Vasco, D., et al. 2013, *A&A*, 550, A110
- Staubert, R., Klochkov, D., & Wilms, J. 2009, *A&A*, 500, 883
- Staubert, R., Shakura, N. I., Postnov, K., et al. 2007, *A&A*, 465, L25

- Steele, I. A., Negueruela, I., Coe, M. J., et al. 1998, *MNRAS*, 297, L5+
- Stella, L., White, N. E., & Rosner, R. 1986, *ApJ*, 308, 669
- Strüder, L., Briel, U., Dennerl, K., et al. 2001, *A&A*, 365, L18
- Syunyaev, R. A. 1976, *Soviet Astronomy Letters*, 2, 111
- Tananbaum, H., Gursky, H., Kellogg, E. M., et al. 1972, *Astronomy Letters*, 174, L143
- Tanvir, N. R., Fox, D. B., Levan, A. J., et al. 2009, *Nature*, 461, 1254
- Tauris, T. M., & van den Heuvel, E. P. J. 2006, Formation and evolution of compact stellar X-ray sources, ed. W. H. G. Lewin & M. van der Klis, 623–665
- Tavani, M., Barbiellini, G., Argan, A., et al. 2008, *Nuclear Instruments and Methods in Physics Research A*, 588, 52
- Tchernin, C., Ferrigno, C., & Bozzo, E. 2011, *The Astronomer's Telegram*, 3173, 1
- Terada, Y., Mihara, T., Nakajima, M., et al. 2006, *Astronomy Letters*, 648, L139
- Trümper, J. 1984, *Advances in Space Research*, 3, 483
- Trümper, J., Kahabka, P., Oegelman, H., et al. 1986, *Astronomy Letters*, 300, L63
- Trümper, J., Pietsch, W., Reppin, C., et al. 1978, *Astronomy Letters*, 219, L105
- Tsygankov, S. S., Lutovinov, A. A., Churazov, E. M., et al. 2006, *MNRAS*, 371, 19
- Tsygankov, S. S., Lutovinov, A. A., Churazov, E. M., et al. 2007, *Astronomy Letters*, 33, 368
- Tsygankov, S. S., Lutovinov, A. A., & Serber, A. V. 2010, *MNRAS*, 401, 1628



- Tueller, J., Ajello, M., Barthelmy, S., et al. 2005, *The Astronomer's Telegram*, 504, 1
- Turner, M. J. L., Abbey, A., Arnaud, M., et al. 2001, *A&A*, 365, L27
- Ubertini, P., Lebrun, F., Di Cocco, G., et al. 2003, *A&A*, 411, L131
- van Paradijs, J. 1988, *Timing Neutron Stars*, 191
- Vasco, D. 2012, PhD thesis, IAAT University of Tuebingen
- Vasco, D., Klochkov, D., & Staubert, R. 2011, *A&A*, 532, A99
- Vasco, D., Staubert, R., Klochkov, D., et al. 2013, *A&A*, 550, A111
- Vedrenne, G., Roques, J.-P., Schönfelder, V., et al. 2003, *A&A*, 411, L63
- Verbunt, F., Pooley, D., & Bassa, C. 2008, *IAU Symposium*, 246, 301
- Violes, F., Niel, M., Bui-van, A., et al. 1982, *ApJ*, 263, 320
- Voges, W., Pietsch, W., Reppin, C., et al. 1982, *ApJ*, 263, 803
- Vrtilek, S. D., Quaintrell, H., Boroson, B., et al. 2001, *ApJ*, 549, 522
- Vrtilek, S. D., Mihara, T., Primini, F. A., et al. 1994, *Astronomy Letters*, 436, L9
- Weisskopf, M. C., Brinkman, B., Canizares, C., et al. 2002, *PASP*, 114, 1
- White, N. E., & Peacock, A. 1988, *MmSAI*, 59, 7
- White, N. E., Swank, J. H., & Holt, S. S. 1983, *ApJ*, 270, 711
- Wilson-Hodge, C. A., Finger, M. H., Camero-Arranz, A., et al. 2009, *The Astronomer's Telegram*, 2324, 1
- Winkler, C., Courvoisier, T. J.-L., Di Cocco, G., et al. 2003, *A&A*, 411, L1
- Woosley, S. E., & Weaver, T. A. 1986, *Ann. Rev. A&A*, 24, 205
- Zane, S., & Ramsay, G. 2001, in *Two Years of Science with Chandra*
- Zane, S., Ramsay, G., Jimenez-Garate, M. A., et al. 2004, *MNRAS*, 350, 506



# Appendix A

## Appendix

### A.1 *RXTE* and *INTEGRAL* observations of A 0535+26

*Figure A.1:*

In the *top panel*, we show a normalized and averaged *RXTE* (magenta) and *INTEGRAL* (blue) pulse profile. The panels below show the parameters of the photon index  $\Gamma$ , the rolloff energy  $E_{\text{rolloff}}$ , the cyclotron line energy  $E_{\text{cyc}}$ , width  $\sigma_{\text{cyc}}$  and depth  $\tau_{\text{cyc}}$  and the iron line intensity  $\text{INT}_{\text{Fe}}$ . For each phase bin (numbered from "1" to "10"), we analyzed the three *RXTE* observations (marked by magenta triangles) and the *INTEGRAL* observations of rev. 0912, 0914, 0915 and 0916/0917. We accumulated spectra for the two *INTEGRAL* observations with the lowest luminosity, 0916 and 0917. In each phase bin the observations are ordered from left to right - from low to high luminosity. The errors are at  $1\sigma$  confidence level. For the fit all parameters were left free. For the fit of  $\sigma_{\text{cyc}}$  of *INTEGRAL* observations 0912, phase bin 0.2–0.3 and observation 0914, phase bin 0.5–0.6, we could only determine the lower limit of the  $1\sigma$  error and extrapolated this value to an upper limit.

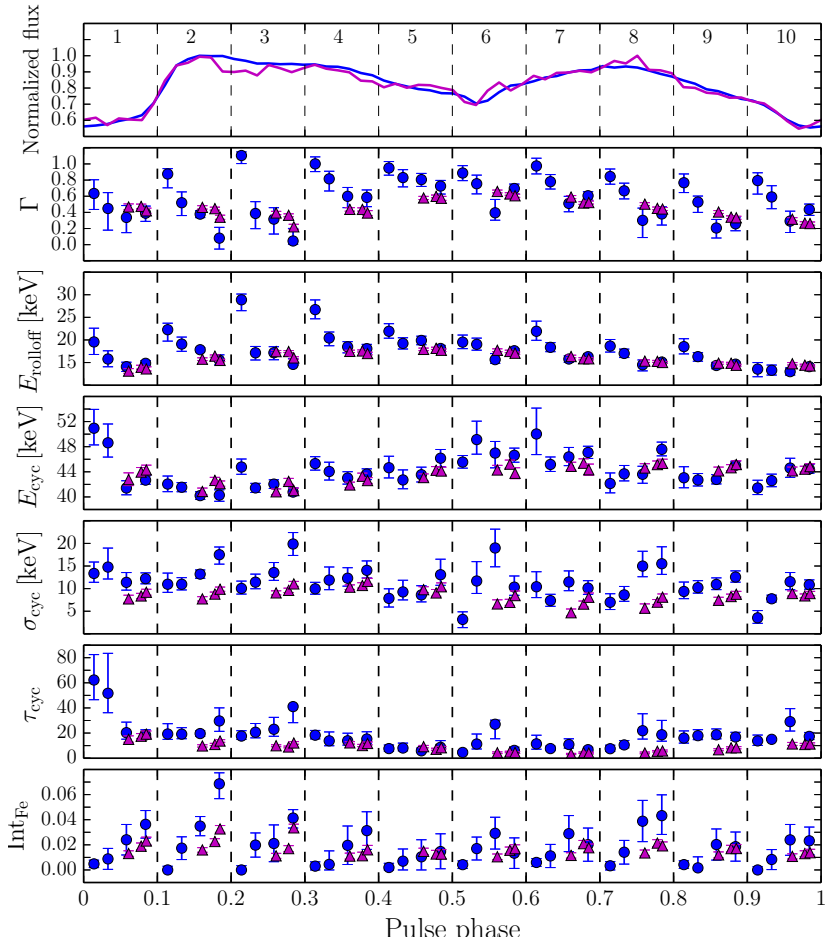


Figure A.1: Fit parameters of the pulse phase resolved analysis. More details, see A.1.

Table A.1: Probability values of the F-test for the *INTEGRAL* observations. With the F-test, we evaluated whether a linear fit with a non-zero slope is statistically preferred over a fit with a constant. A low value indicates that a fit with a non-zero slope is preferred to a fit with a constant line.

Phase bin		P-value $\Gamma$	P-value $E_{\text{cyc}}$
1	0.0–0.1	0.211	0.365
2	0.1–0.2	0.020	0.115
3	0.2–0.3	0.038	0.278
4	0.3–0.4	0.046	0.253
5	0.4–0.5	0.033	0.420
6	0.5–0.6	0.484	0.538
7	0.6–0.7	0.166	0.479
8	0.7–0.8	0.062	0.081
9	0.8–0.9	0.099	0.169
10	0.9–1.0	0.231	0.047

## A.2 *XMM-Newton* observations of Her X-1

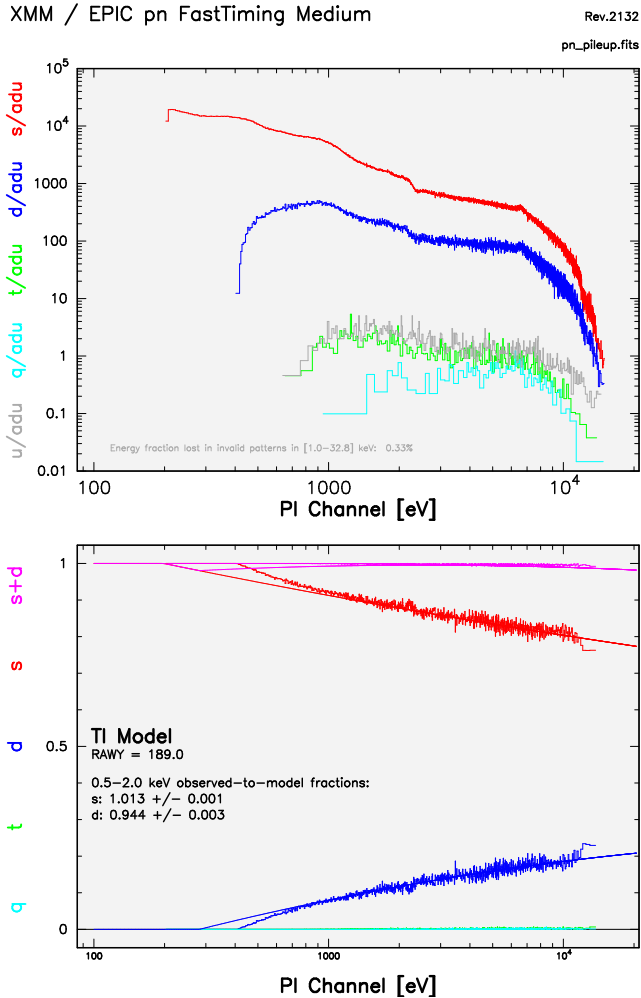


Figure A.2: *EPIC-pn* pattern distribution plot of observation 05. The relative ratios of single and double events and the deviation from the standard values are shown.

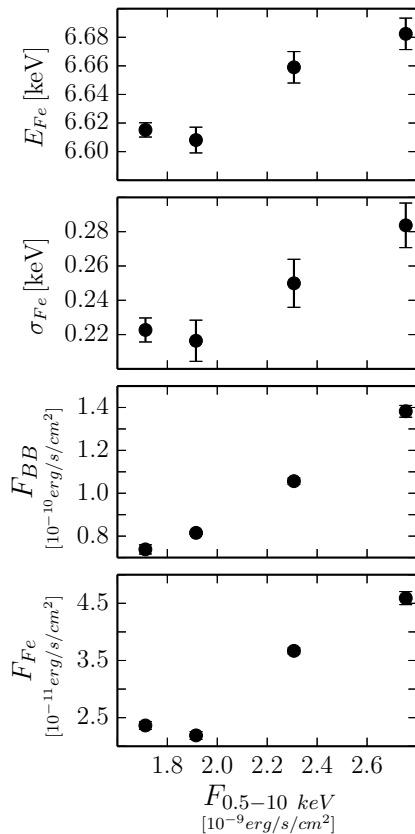


Figure A.3: The fit parameters of the *EPIC-pn* spectra as the Fe line is fitted with 1 Gaussian. We show the Fe line energy and width,  $E_{\text{Fe}}$  and  $\sigma_{\text{Fe}}$ , and the flux in the blackbody and iron line component as estimated with the `cflux` command in *XSPEC*,  $F_{\text{BB}}$  and  $F_{\text{Fe}}$ , as a function of the total 0.5–10 keV flux. The errors are  $1 \sigma$ .





# Publications

**A&A 535, A102, 2011:**

**No apparent accretion mode changes detected in Centaurus X-3 (Research Note)**

D. Müller<sup>1</sup>, D. Klochkov<sup>1</sup>, A. Santangelo<sup>1</sup>, T. Mihara<sup>2</sup>, and M. Sugizaki<sup>2</sup>

<sup>1</sup> Institut für Astronomie und Astrophysik, Universität Tübingen,  
Germany

<sup>2</sup> MAXI team, RIKEN, 2-1 Hirosawa, Wako, Saitama 351-0198, Japan

*Abstract: Aims.* Two distinct spectral states have previously been reported for Cen X-3 on the basis of RXTE/ASM observations. Intrigued by this result, we investigated the spectral properties of the source using the enhanced possibilities of the X-ray data now available with the aim to clarify and interpret the reported behavior. *Methods.* To check the reported results, we used the same data set and followed the same analysis procedures as in the work that reported the two spectral states. Additionally, we repeated the analysis using the enlarged data sample including the newest RXTE/ASM observations as well as the data from the MAXI monitor and from the INTEGRAL/JEM-X and ISGRI instruments. *Results.* We were unable to confirm the reported presence of the two spectral states in Cen X-3 either in the RXTE/ASM data or in the MAXI or INTEGRAL data. Our analysis shows that the flux variations in different energy bands are consistent with a spectral hardness that is constant over the entire time covered by observations.

**A&A 540, A35, 2012:**

**Analysing X-ray pulsar profiles - Geometry and beam pattern of 4U 0115+63 and V 0332+53**

M. Sasaki<sup>1</sup>, D. Müller<sup>1</sup>, U. Kraus<sup>2</sup>, C. Ferrigno<sup>3</sup>, and A. Santangelo<sup>1</sup>

<sup>1</sup> Institut für Astronomie und Astrophysik, Universität Tübingen, Germany

<sup>2</sup> Institut für Physik, Universität Hildesheim, Germany

<sup>3</sup> ISDC Data Centre for Astrophysics, Univeristy of Geneva, Switzerland

*Abstract: Aims.* By analysing the asymmetric pulse profiles of the transient Be/X-ray binaries 4U0115+63 and V 0332+53 we aim to identify the origin of the pulsed emission to understand the geometry of the accretion onto the neutron star. *Methods.* We have applied the pulse-profile decomposition method, which enabled us to find two symmetric pulse profiles for the two magnetic poles of the neutron star. We derived beam patterns for different energy bands and luminosity states. This allowed us to identify the components that are responsible for the emission. The analysis and the models used for the interpretation of the results take relativistic light deflection into account. *Results.* We find that the magnetic field of the neutron star is distorted in both 4U0115+63 and V0332+53. The beam patterns are interpreted in terms of a model for an accretion column that includes the formation of a halo at the bottom of the accretion column and scattering in the upper accretion stream. *Conclusions.* In both systems, an accretion column forms while the accretion rate is high. If the accretion decreases and the sources become fainter, the emission from the halo and the accretion column disappears. In 4U0115+63 there seems to be significant scattering of photons in the still existing accretion stream even at the end of the outburst. In V 0332+53, the scattering in the upper stream also disappears at the end and we apparently observe the emission from the hot spots on the neutron star.

**A&A, 552, A81, 2013:**

**A 0535+26 in the April 2010 outburst: probing the accretion regime at work**

D. Müller<sup>1</sup>, D. Klochkov<sup>1</sup>, I. Caballero<sup>2</sup>, and A. Santangelo<sup>1</sup>

<sup>1</sup> Institut für Astronomie und Astrophysik, Universität Tübingen, Germany

<sup>2</sup> Laboratoire AIM, CEA/IRFU, CNRS/INSU, Université Paris Diderot, CEA DSM/IRFU/SAP, 91191 Gif-sur-Yvette, France

*Abstract: Context.* A number of accreting X-ray pulsars experience spectral changes, both on the long time scales and on the time scales of the neutron star spin period. The sources seem to form two distinct groups that differ by the type of the spectral variations with flux. Such a bimodality probably reflects two different regimes of accretion that may result in a particular pulsar depending on its luminosity so-called sub- and super-critical regimes. *Aims.* We investigated the behavior of the spectral parameters of the Be/X-ray binary system A 0535+26, as a function of flux and pulse phase. *Methods.* We used the data collected with INTEGRAL and RXTE during the April 2010 outburst of the source. We analyzed the phase-averaged and phase-resolved spectra and performed pulse-to-pulse spectral analysis of the pulsar. *Results.* Our analysis reveals variability in the continuum parameters of the sources pulse-averaged spectrum with flux. The pulse-averaged cyclotron line energy does not change with the source luminosity during the outburst, which is consistent with previous studies. Our pulse-phase resolved and pulse-to-pulse analyses reveal, however, indications for a positive correlation of the cyclotron line energy with flux, as well as a flux-dependence of the continuum parameters. Based on the observed behavior, we argue that A 0535+26 operates at the sub-critical accretion regime.



# Acknowledgment

I want to thank all people who contributed to this work. Without your help, this would not have been possible!

Thanks to my supervisors, Andrea Santangelo and Dmitry Klochkov, for giving me the opportunity to work on this highly interesting and puzzling field of X-ray astrophysics. I had a great time and I really liked to work in your group, Andrea. Thank you for your advice and discussions during all these years. Dima, thank you for everything, for your help with data processing, analysis, discussions, for always being ready to help and discuss any problems! Especially during the last couple of months of finishing this thesis!

I also want to thank Manami Sasaki, who introduced me to the X-ray data analysis during the time of my Diploma thesis at the institute. Prof. Staubert, thank you for your suggestions and ideas for the analysis and discussion of Her X-1.

I would like to thank Isabel Caballero for her help with the analysis and discussion of A 0535+26.

I had a great time at the institute, thanks to my colleagues who made my time at the institute so entertaining and nice, thanks to the coffee round, and especially to Benni, Davide and Marc.

A big thank goes to my family and friends who supported me over all the years. Thank you mum and dad and to my brother for always being there. Tina and Anne, it was a lot of fun to study together with you! A big hug and kiss to my husband Raimund and my son Jonas. Thank you Raimund for your help with the thesis, especially for providing me the

time to finally submit the thesis during the last couple of weeks. Jonas, you make life so colorful and happy!

# Curriculum vitae

- 24.08.1985 Born in Nürtingen, Germany
- 1992 - 1996 Elementary school (Grundschule), Mörikeschule  
Köngen, Germany
- 1996 - 2005 High School (Gymnasium),  
Robert-Bosch-Gymnasium Wendlingen
- 10.2005 - 09.2010 Study of Physics at the Eberhard Karls  
Universität Tübingen, Germany, specialized on  
astrophysics and medical physics
- 01.2010 - 09.2010 Preparation of Diploma Thesis entitled: "Pulse  
Profile Decomposition of the Accreting X-ray  
Pulsar V 0332+53" under the supervision of Dr.  
M. Sasaki, Prof. A. Santangelo at the Eberhard  
Karls Universität Tübingen, Germany; Institute  
of Astronomy and Astrophysics (IAAT)
- 09.2010 Diploma in physics
- 10.2010 - 12.2013 Scientific employee at the IAAT
- since 10.2010 Preparation of this thesis entitled: "Accretion  
regimes in the X-ray binary systems A 0535+26  
and Her X-1/HZ Her" under the supervision of  
Dr. D. Klochkov, Prof. Dr. A. Santangelo at  
the IAAT
- since 07.2013 Parental leave (Elternzeit)